DOI: 10.1070/RCR4879

Dispersion forces in nanoscience

Anatoly I. Rusanov, Elena N. Brodskaya

Institute of Chemistry, Saint Petersburg State University,
Universitetskaya nab. 7 – 9, 199034 Saint Petersburg, Russian Federation

The 21st century was marked by a new outbreak of interest in dispersion forces in nanoscale systems. However, now the consideration is conducted at a different level. Whereas earlier the main object of study was infinite plane-parallel films, now it is a question of calculations for systems of a more complex configuration with non-parallel and finite surfaces of various shapes. On the other hand, it is not the average interaction force that is estimated, but the detailed mechanical state of the interacting bodies, for which statistical mechanics and the Irving – Kirkwood stress tensor are involved. This review summarizes the theoretical studies of plane-parallel, but finite-area films, wedge-shaped films, systems with spherical, cylindrical, and conical surfaces. Particular consideration is given to interactions involving nanoparticles. Spheroidal particles, rod-like and disc-shaped particles are analyzed. The shape factor of the interaction of particles with a flat surface is estimated. The calculation of the contribution of dispersion forces to surface, line and point tension is explained. Among the latest news is the calculation (brought to numbers) of the contribution of dispersion forces to the graphene point energy. The bibliography includes 109 references.

Contents

1. Introduction: dispersion forces in surface and colloid science 838
2. Interaction of nonparallel flat surfaces. A wedge-shaped slit 841
3. Conical surface 845
4. Parallel semi-infinite flat surfaces 848
5. Interactions with participation of nanoparticles 850
6. Contribution of dispersion forces to surface, line, and point tension 866
7. Concluding remarks 872

The following abbreviations are used in the review:

A_{st} is the constant of potential,
a_s is the radius of nanosphere,
a_d is the radius of nanocylinder,
a_c is the radius of nanorod,
c is the number density of body,
d is the thickness of nanocylinder,
$\hat{E}$ is the stress tensor,
$\mathbf{e}_r$ and $\mathbf{e}_\varphi$ are the orts of cylindrical coordinates,
$\mathbf{F}$ is the force of interaction of two solid bodies,
$g(R)$ is the radial distribution function,
$G(R)$ is the total correlation function,
H is the distance between surfaces,
k is the Boltzmann constant,
L is the length of nanorod,
$\hat{p}$, p_N, p_T are the pressure tensor and its normal and tangential components,
p_{rr}, p_{zz}, $p_{\varphi\varphi}$, $p_{rz}, p_{r\varphi}, p_{z\varphi}$ are the pressure tensor components in cylindrical coordinates,
p^α is the pressure in bulk phase α,
R_{ij} is the distance between i and j molecules,
S is the structure factor,
T is the absolute temperature,
U is the energy of interaction of two solid bodies,
V is the volume of body,
$X(R)$ is the direct correlation function,
W_{12} is the potential of mean force,
Γ_s is the adsorption of component s,
ε is the line energy,
η is the point tension,
θ is the dihedral angle of the slit or the cone,
Θ is the shape factor,
κ is the line tension,
μ_s is the chemical potential of component s,
Π is the disjoining pressure,
$\rho^{(1)}$ is the one-particle distribution function,
$\rho^{(2)}(\mathbf{r}_1, \mathbf{r}_2)$ is the two-particle distribution function,
$\rho\{n\}$ is the distribution function of the set of n molecules,
σ is the surface tension,
Φ_{st} is the intermolecular potential,
χ is the isothermal compressibility.

A.I.Rusanov. Doctor of Science, Professor, Academician of RAS, Head of the Department of Colloid Chemistry at the Institute of Chemistry, St. Petersburg State University.
Telephone: +7(812)554 – 2877, e-mail: airusanov@mail.ru
E.N.Brodskaya. Doctor of Science, Professor of the same Department.
E-mail: e.brodskaya@spbu.ru
Current research interests of authors: surface and colloid science.

Received 25 February 2019

© 2019 Uspekhi Khimii, Russian Academy of Sciences and Turpion Ltd.

1. Introduction: dispersion forces in surface and colloid science

The history of dispersion forces started with publishing London's theory [1,2] that resulted in the pair potential of molecular attraction in a vacuum. We write it here in the form

$$\Phi_{st}(R_{ij}) = -A_{st}R_{ij}^{-6} \tag{1}$$

where R_{ij} is the distance between molecules i and j, and s and t are the sorts of molecules i and j, respectively. Equation (1) is a strict asymptotic relationship, and distance R is implied to be large as compared with molecular dimensions. However, on passing to especially large distances, the effect of electromagnetic retardation yields another asymptotics (with the exponent decreased by one):

$$\Phi_{st}(R) = -A'_{st}R^{-7} \tag{2}$$

as it was stated by Casimir and Polder.[3] The contribution of this form of dispersion interaction in practical calculations is typically small and seldom taken into account. It is of note that the pair potential form presented by Eqn (1) is also inherent in the interaction of rotating and induced dipoles. For this reason, Eqn (1) is often more generally qualified as relating to the London–van der Waals forces.

Possessing a pair potential provokes calculating the interaction between bodies by means of the pairwise summation. Dealing with Eqn (1), Hamaker [4] considered the interaction between two spheres, between a sphere and a semi-infinite solid with a flat surface, and between two flat-parallel surfaces. The computational scheme was the following. The first step was the summation of the pair potential for interacting bodies 1 and 2 as the integration over their volumes V_1 and V_2. This yielded the interaction energy

$$U = c_1c_2\int_{V_1}\mathrm{d}V_1\int_{V_2}\mathrm{d}V_2\Phi_{12} \tag{3}$$

where c_i is the molecular number density for body i ($i = 1, 2$). The second step was the differentiation of Eqn (3) with respect to the body separation H to yield the interaction force F. The most famous Hamaker's result is the interaction force (per unit surface area S) for two flat-parallel surfaces (with a correction in sign because Hamaker wrote plus instead of minus)

$$\Pi = \frac{F}{S} = -\frac{\pi c_1c_2A_{12}}{6H^3} \equiv -\frac{C}{H^3} \tag{4}$$

and the constant $C \equiv \pi c_1c_2A_{12}/6$ is now called Hamaker's constant. Hamaker's results were repeatedly replicated later in the literature, but we do not include such works in our review.

Derjaguin [5] named the quantity Π 'disjoining pressure' and defined it generally as

$$\Pi = p - p^{\alpha} \tag{5}$$

where p is the pressure at the surface of an interacting body and p^{α} is the pressure in the bulk of phase α, which is a fluid surrounding medium where the body interaction occurs ($p^{\alpha} = 0$ and $p < 0$ in the case of vacuum). The concept of disjoining pressure (5) played an important role in the theory of thin films [6–8] and, especially, in the theory of stability of lyophobic colloid systems first formulated by Derjaguin and Landau [9] on the basis of the joint action of dispersion and electrostatic forces.

Returning to the procedure of pairwise summation, it was questioned as not sufficiently strict [7] and not accounting for multi-body interactions, which is especially important when interaction occurs through a condensed medium.[10] As a consequence, a novel non-microscopic approach was elaborated by Lifshitz.[11] His main idea was considering the interaction between condensed bodies as tensions associated with the quantum and thermal fluctuations of the electromagnetic field in the medium. Lifshitz' theory expresses interaction forces *via* the electrodynamic characteristic of matter, its complex dielectric permittivity. Such a macroscopic approach was a comprehensive alternative to the microscopic theory dealing with a pair potential. In course of its further development,[12] the macroscopic theory soon became dominant in the literature on dispersion forces.[7,10,13]

On the other hand, the failure of the microscopic theory of dispersion forces turned to be only temporary. Its further existence and improvement was due to the following factors. First, it was shown that accounting for multi-body forces is asymptotically reduced to the renormalization of the pair potential constant A_{st} in Eqn (1).[14,15] As a result, an effective pair potential was constructed whose dependence on R at large R is the same as in Eqn (1) with the only difference that the interaction constant value should be changed. Similarly to the ordinary pair potential, the effective pair potential can be used for calculating statistically average quantities.[16] The second factor was the development of statistical mechanics (the apparatus of distribution functions, functional expansions, diagram technique, *etc.*),[17–26] especially in connection with the pair potential expressed in Eqn (1). In fact, the famous Bogoliubov–Born–Green–Kirkwood–Yvon hierarchy of statistical mechanics already relates distribution functions to pair potentials. In addition, the condition of weakening correlations was formulated in connection with Eqn (1).
For example, the two-particle distribution function $\rho^{(2)}(\mathbf{r}_1, \mathbf{r}_2)$ asymptotically behaves as [23]

$$\rho^{(2)}(\mathbf{r}_1, \mathbf{r}_2) = \rho^{(1)}(\mathbf{r}_1)\rho^{(1)}(\mathbf{r}_2) + \frac{kTA_{12}}{R^6}\frac{\partial\rho^{(1)}(\mathbf{r}_1)}{\partial\mu}\frac{\partial\rho^{(1)}(\mathbf{r}_2)}{\partial\mu} \tag{6}$$

where $\rho^{(1)}$ is the one-particle distribution function and μ is chemical potential. Eqn (6) is written in the most general form when the presence of external fields is not excluded. In the absence of external fields, $\rho^{(1)}$ can be replaced by the molecular number density c. Then, using the thermodynamic relationship $\partial c/\partial\mu = c^2\chi$ (χ is the isothermal compressibility), Eqn (6) (with $A_{st} = A$ for a one-component system) becomes

$$\rho^{(2)}(\mathbf{r}_1, \mathbf{r}_2) = c^2 + \frac{kTAc^4\chi^2}{R^6} \tag{7}$$

It is seen from Eqn (7) that replacing the two-particle distribution function by the density square becomes possible at a large distance R and at a small compressibility χ for condensed matter and especially for solids. This result was also obtained as [21]

$$g(R) \sim 1 + \frac{AS^2}{kTR^6} \tag{8}$$

$$G(R) \sim \frac{AS^2}{kTR^6} \tag{8a}$$

$$X(R) \sim \frac{A}{kTR^6} \tag{8b}$$

where $g(R)$ is the radial distribution function, $G(R)$ is the total correlation function, $X(R)$ is the direct correlation function, and S is the structure factor with a thermodynamic relationship $S = kTc\chi$. The total and direct correlation functions are related to each other as (the Ornstein–Zernike equation for a homogeneous phase).

$$G(R) = X(R) + c\int \mathrm{d}\mathbf{r}_3 X(|\mathbf{r}_1 - \mathbf{r}_3|)G(|\mathbf{r}_2 - \mathbf{r}_3|) \tag{9}$$

If one- and two-particle distribution functions and the molecular pair potential are known, statistical mechanics makes it possible to calculate the stress tensor as an indicator of the interaction force. The computational scheme was elaborated by Irving and Kirkwood [27] and yields the following expression for the stress tensor $\hat{E}$ at a point $\mathbf{r}$:

$$\hat{E}(\mathbf{r}) = -kT\sum_s \rho_s^{(1)}(\mathbf{r})\ \hat{1} + \frac{1}{2}\sum_{s,t}\int \frac{\mathbf{R}\times\mathbf{R}}{R}\ \Phi'_{st}(R)\mathrm{d}\mathbf{R}\int_0^1 \rho_{st}^{(2)}(\mathbf{r}-\eta\mathbf{R}, \mathbf{r}-\eta\mathbf{R}+\mathbf{R})\mathrm{d}\eta \tag{10}$$

Equation (10) includes two terms. The first term is a kinetic part of the tensor where the probability of finding any molecule of sort s at the point $\mathbf{r}$ is given by the one-particle distribution function $\rho_s^{(1)}$ as the local density of molecules of sort s, and $\hat{1}$ is the unit tensor. The second term is a force part where $\mathbf{R}$ is the vector connecting two interacting particles with separation R between them and passing through point $\mathbf{r}$; $\Phi'_{st}(R)$ is the derivative of potential $\Phi_{st}(R)$ (*i.e.* the force of interaction between particles of sorts s and t); $\rho_{st}^{(2)}(\mathbf{r}-\eta\mathbf{R}, \mathbf{r}-\eta\mathbf{R}+\mathbf{R})$ is the two-particle distribution function corresponding to the simultaneous location of any molecule of sort s at point $\mathbf{r}-\eta\mathbf{R}$ and any molecule of sort t at point $\mathbf{r}-\eta\mathbf{R}+\mathbf{R}$ on the opposite sides from a unit surface with coordinate $\mathbf{r}$ (that is controlled by an additional variable η). The integration with respect to $\mathbf{R}$ is performed over the whole space. The Irving–Kirkwood tensor accounts only for those molecular pairs whose connecting lines intersect the elementary unit area with coordinate $\mathbf{r}$ (which splits R into fractions η and $1-\eta$). It is of note that, in principle, the definition of a local stress tensor is not unique, and there can be alternative definitions with respect to Eqn (8). As a good example, it is appropriate to recall the stress tensor with which Buff operated [28, 29] (also called Harasima's tensor in the literature [30, 31]). However, in contrast with the Harasima–Buff tensor, the Irving–Kirkwood stress tensor satisfies the mechanical equilibrium condition (written here in the absence of an external field).

$$\nabla\cdot\hat{E}(\mathbf{r}) = 0 \tag{11}$$

In this way, the Irving–Kirkwood stress tensor confirms its physical significance. On going to fluid structures, the stress tensor is usually replaced by the pressure tensor, $\hat{p}(\mathbf{r})$,which differs from the stress tensor only in sign.

Comparing now the macroscopic and microscopic variants of the theory of dispersion forces, we can say that the latter is more suitable for more detailed description of physicochemical systems with dispersion forces. Microscopic theory makes possible calculating not only the total force of interaction between two bodies, but also the strength distribution over the body surface. This is especially important for nanoscience. Numerous results of macroscopic theory concerning dispersion forces in surface and colloid science were exhaustively reviewed in a number of monographs.[7, 10, 13] However, these monographs only a little concerned contemporary results of the microscopic theory, not to speak about results of subsequent time. The purpose of this survey is to fill this gap.

The problem of interaction of bodies in a fluid medium requires the knowledge of properties of the fluid as a conductor of interaction. This is why the statistical mechanics of fluids plays a significant role in the microscopic theory of interaction of bodies. What immediately happens at, say, the solid/fluid contact is the formation of a fluid surface layer at a nanoscale thickness (a certain reconstruction of a solid also occurs near the surface). So it was not surprising that an expansive series of papers was devoted to the statistical-mechanical studying of surface layers (we only refer to those related to dispersion forces [32–40]). The main analysis tool was the functional expansions for distribution functions in combination with the condition of weakening correlations of type of Eqn (8) and a pair potential of type of Eqn (1). Explicit relationships were derived to describe the asymptotic behaviour of the one-particle distribution function (the local particle concentration), the two-particle distribution function, the local composition of a mixture, and the local pressure tensor (on the basis of the Irving–Kirkwood stress tensor) in a surface layer. In addition, the case of a thin fluid film between two interacting bodies (where two surface layers act simultaneously) was analyzed with calculating the disjoining pressure.[36, 41–43]

This large series of works was covered in the international review of that time.[44] But soon a new universal and powerful interaction research method was developed, especially applicable to dispersion forces. It entered the literature under the title 'The asymptotic principle of the interaction of bodies in a liquid medium'.[45–47] Since in essence we mean a fluid (liquid or gaseous) medium, this principle can be formulated in the words as follows: *Two bodies in a fluid medium interact at a large distance so as the bodies (including adjacent fluid surface layers) interact in a vacuum provided their local densities are measured from the density of the fluid medium*. The corresponding mathematical notation of the principle is [45]

$$W_{12} = -\sum_s \int_{V'_1} \mathrm{d}\mathbf{r}_1 \Delta\rho_s(\mathbf{r}_1|\{n_1\})\sum_t \int_{V'_2} \mathrm{d}\mathbf{r}_2 \Delta\rho_t(\mathbf{r}_2|\{n_2\})A_{st}r_{12}^{-\lambda} \tag{12}$$

where W_{12} is the potential of mean force of interaction of bodies 1 (consisting of the set of molecules $\{n_1\}$) and 2 (the set of molecules $\{n_2\}$), $\Delta\rho_s(\mathbf{r}_1|\{n_1\}$ or $\Delta\rho_s(\mathbf{r}_2|\{n_2\})$ is the local excess of the number density of molecules of sort s in the presence of body 1 or body 2, respectively, V'_1 and V'_2 are the volumes of bodies 1 and including their surface layers. Eqn (12) contains a generalized form of potentials (1) and (2) as

$$\Phi(i,j) = -A_{st} r_{ij}^{-\lambda} \tag{13}$$

In Eqn (13), A_{st} and λ form a pair of constants for both cases ($\lambda = 6$ without retardation and $\lambda = 7$ with retardation). The arguments i and j include molecular sorts, s and t, and also the 1 coordinates **i** and **j** (in particular, the radius-vectors $\mathbf{r}_i$ and $\mathbf{r}_j$ of molecular centres of mass) of molecules i and j, $r_{ij} \equiv |\mathbf{r}_i - \mathbf{r}_j|$ being the distance between the molecules. Finally, it should be noted that the sizes of molecular complexes can be anything from one molecule to macroscopic bodies. This creates a huge range of application of the asymptotic principle. Already in the original works, such problems were analyzed as the interaction of any two molecular complexes, small compared with the distance between them; the molecular structure of the surface layer far from the boundary surface; interaction of two semi-infinite bodies with plane-parallel surfaces; interaction of two spherical bodies; interaction of a spherical body with a flat surface.[46,47] Some of these problems have already been considered by Hamaker,[4] but the asymptotic principle gives much more general results.

It should be noted that the asymptotic principle is not an approximation, but the exact result of statistical mechanics. Its rigorous proof was given on the basis of the diagram technique.[45] If we talk about its limitations, then, since the principle is asymptotic, it refers to a large distance. The second limitation relates to the type of force. A strict conclusion was given only for dispersion and dipole–dipole forces.

With all its consequences, the asymptotic principle overlaps the results of individual functional expansions when finding distribution functions. On the other hand, the principle describes the interaction of bodies as a whole and can be supplemented by other methods if more detailed information is required. Most often, the role of such an additional method belongs to the Irving–Kirkwood stress tensor, which describes the local mechanical state of a system. The usefulness of such a combination was demonstrated when considering the local properties of curved surfaces. Since these results were not included in broad reviews[48,49] and were published only in the proceedings of a conference,[50] we reproduce here the most interesting of them relating to slightly curved surfaces of an arbitrary curvature

$$\frac{2}{a^*} = \frac{1}{a_x} + \frac{1}{a_y} \tag{14}$$

where a^* is the mean curvature radius, a_x and a_y are the principal curvature radii along directions x and y on the surface. It is implied that $|a^*| \gg h$, where h is the distance from the boundary surface between phases α (a fluid medium) and β (say, a solid adsorbent). In its turn, h is assumed to be much larger than molecular dimensions. With the aid of the asymptotic principle, the dependence of the local distribution functions $\rho\{n\}$ on h in a multicomponent surface layer with dispersion forces is found in the form

$$\rho\{n\} = \rho^{\alpha}\{n\} + \frac{2\pi}{(\lambda-2)(\lambda-3)} h^{-\lambda+3} \times \left[1 + \frac{(\lambda-3)h}{(\lambda-4)a^*}\right] \sum_{s,t} A_{st} \frac{\partial \rho^{\alpha}\{n\}}{\partial \mu_s} (\rho_t^{\beta} - \rho_t^{\alpha}) + \frac{2\pi}{\lambda-2} h^{-\lambda+2} \sum_{s,t} A_{st} \frac{\partial \rho^{\alpha}\{n\}}{\partial \mu_s} \Gamma_t \tag{15}$$

where μ is chemical potential and Γ is adsorption. Next, using (13), the local Irving–Kirkwood pressure tensor is calculated. Obviously, the tensor has a diagonal form in the set of curvilinear coordinates with the origin at the observation point, with the z axis perpendicular to the boundary surface of the adsorbent and the x and y axes along the principal directions on the surface. The resulting expressions for the components of the pressure tensor are[50]

$$p_{\mathrm{N}} \equiv p_{zz} = p^{\alpha} + \frac{2\pi}{(\lambda-2)^2(\lambda-4)} h^{-\lambda+3} \times \left(\frac{h}{a_x} + \frac{h}{a_y} + \frac{3h^2}{2a_x^2} + \frac{3h^2}{2a_y^2} + \frac{h^2}{a_x a_y}\right) \sum_{s,t} A_{st} \rho_s^{\alpha} (\rho_t^{\beta} - \rho_t^{\alpha}) + \frac{2\pi}{(\lambda-2)^2} h^{-\lambda+2} \left(\frac{h}{a_x} + \frac{h}{a_y}\right) \sum_{s,t} A_{st} \rho_s^{\alpha} \Gamma_t \tag{16}$$

$$p_{\mathrm{T1}} \equiv p_{xx} = p^{\alpha} + \frac{2\pi}{(\lambda-2)^2} h^{-\lambda+3} \times \left[1 + \frac{(\lambda-5)h}{2(\lambda-4)a_x} + \frac{(\lambda-3)h}{2(\lambda-4)a_y}\right] \sum_{s,t} A_{st} \rho_s^{\alpha} (\rho_t^{\beta} - \rho_t^{\alpha}) + \frac{2\pi(\lambda-3)}{(\lambda-2)^2} h^{-\lambda+2} \sum_{s,t} A_{st} \rho_s^{\alpha} \Gamma_t \tag{17}$$

$$p_{\mathrm{T2}} \equiv p_{yy} = p^{\alpha} + \frac{2\pi}{(\lambda-2)^2} h^{-\lambda+3} \times \left[1 + \frac{(\lambda-3)h}{2(\lambda-4)a_x} + \frac{(\lambda-5)h}{2(\lambda-4)a_y}\right] \sum_{s,t} A_{st} \rho_s^{\alpha} (\rho_t^{\beta} - \rho_t^{\alpha}) + \frac{2\pi(\lambda-3)}{(\lambda-2)^2} h^{-\lambda+2} \sum_{s,t} A_{st} \rho_s^{\alpha} \Gamma_t \tag{18}$$

where $p_{\mathrm{N}} \equiv p_{zz}$, $p_{T1} \equiv p_{xx}$ and $p_{\mathrm{T2}} \equiv p_{yy}$ are the normal pressure and two tangential pressures. The correctness of Eqns (16)–(18) is confirmed by the fact that they satisfy the mechanical equilibrium condition, Eqn (11), which, in this case, takes the form

$$-\frac{1}{(a_x - h)(a_y - h)} \frac{\mathrm{d}}{\mathrm{d}h} \left[(a_x - h)(a_y - h) p_{\mathrm{N}}\right] = \frac{p_{xx}}{a_x - h} + \frac{p_{yy}}{a_y - h} \tag{19}$$

It is of note that Eqn (19) itself facilitated finding true correcting terms in Eqn (16).[50] Considering strongly curved surfaces, the interest shifts to the central part of the cavity in a body (say, in a pore inside an adsorbent). The cases of the spherically[47,50] and cylindrically[50–52] symmetrical systems were analyzed comprehensively.

The combination of the asymptotic principle with the Irving–Kirkwood pressure tensor is often found in modern works, which are reviewed below. The material was distributed as follows. In Section II, we proceed to consider the interaction of bodies whose configuration differs from the classical version of bodies with infinite parallel surfaces. Both empty wedge-shaped slits and those filled with fluid are considered. For small wedge angles, the effect of deviations from a parallel film on the components of the pressure tensor is estimated. Section III is devoted to the analysis of a conical cavity inside a solid filled with a fluid. The

contributions of the angular dependence for the normal and tangential components of the pressure tensor near the axis of the cone are estimated. Since the surfaces of a wedge-shaped slit become infinite when passing to the zero wedge angle, the case of a bounded plane-parallel slit is considered separately in Section IV. The dependence of the components of the pressure tensor on the distance to the end of the slit is found. Section V deals with nanoparticle interactions. This is the case when interacting bodies are separated by a slit with limited dimensions in all directions. The interactions of nanoparticles of various shapes (globular, rod-shaped and lamellar), but of the same volume and nature, with a macroscopic solid are compared. Section VI deals with issues related to the calculation of the contribution of dispersion forces to surface, line, and point energy. The calculation of the line tension at the curved edge of a molecular solid is given. Turning to two-dimensional structures, the calculation of line and point tensions and energies is discussed. For graphene, estimates are given to numeric values. Finally, Section VII contains concluding remarks. Two problems are discussed here: the possibility of replacing the summation by integration in calculations for crystalline solids and the need for a series of quantum chemical calculations to determine the local properties of solid particles in modern nanoscience.

2. Interaction of nonparallel flat surfaces. A wedge-shaped slit

Most of the calculations using the Irving–Kirkwood stress tensor refer to infinite flat-parallel surfaces. Gradually proceeding to nanoparticles, we must reduce the dimensions in all directions. The first step is the transition from infinite to semi-infinite surfaces. Nonparallel surfaces are evident to form the widest class of such surfaces because they always intersect and thus become semi-infinite. So we begin with considering the interaction between non-parallel surfaces of various shapes and then return to flat-parallel surfaces.

The most popular example of a wedge-shaped slit is a solid crack whose thermodynamics was reviewed in detail.[53] Because of this connection, the question of forces acting in a wedge-shaped slit was of particular practical importance and multiply discussed in the literature, for example, for solvation forces.[54–57] In addition, the effect of surface roughness of the slit walls was simulated [58] to estimate the average pressure tensor in a film inside the slit. However, the investigation considered only parallel (on the average) slit walls and did not touch upon the case of a wedge-shaped film. The latter case was analyzed soon [8, 59–62] with formulating the mechanical equilibrium conditions for a non-uniform film. For a long time, only integral effects were concerned in the literature, until a detailed analysis of local properties of a wedge-shaped film was performed.[63–68] Of this series of papers, only the first one [63] managed to be mentioned in the review on cracks.[53] Now we present the problem in full.

2.1. Interaction through an empty wedge-shaped slit

We depict a wedge-shaped slit as a dihedral angle θ with the z-axis at the apex of the angle and flat endless faces. The cylindrical coordinates z, r, and φ with orts $\mathbf{e}_r$ and $\mathbf{e}_\varphi$ (Fig. 1, the z-axis is perpendicular to the figure plane) seem to be most convenient for describing local characteristics in such a system. Here we consider a simple symmetrical case when both slit walls are identical as it happens, for example, in a solid crack.[63, 64]

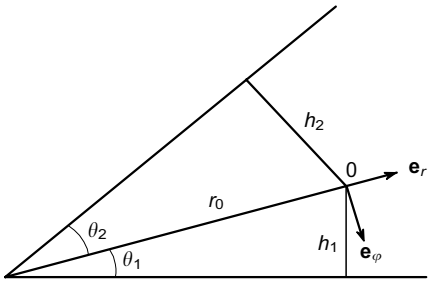


Figure 1. The profile of a wedge-shaped slit with the calculation point at the origin 0 of the cylindrical coordinates, $\theta_1 + \theta_2 = \theta$ is the dihedral angle of the slit.[63]

Accounting for the symmetry condition in the cylindrical coordinates, the structure of the pressure tensor in a wedge-shaped slit is of the form

$$\hat{p} = \begin{pmatrix} p_{rr} & p_{r\varphi} & 0 \\ p_{\varphi r} & p_{\varphi\varphi} & 0 \\ 0 & 0 & p_{zz} \end{pmatrix} \tag{20}$$

and the mechanical equilibrium condition following from Eqn (11) becomes

$$\frac{\partial p_{rr}}{\partial r} + \frac{p_{rr} + p_{\varphi\varphi}}{r} + \frac{1}{r}\frac{\partial p_{r\varphi}}{\partial \varphi} = 0 \tag{21}$$

$$\frac{1}{r}\frac{\partial p_{\varphi\varphi}}{\partial \varphi} + \frac{2p_{r\varphi}}{r} + \frac{\partial p_{r\varphi}}{\partial r} = 0 \tag{22}$$

$$\frac{\partial p_{zz}}{\partial z} = 0 \tag{23}$$

To give a complete description of the mechanical state of the slit, the problem consists of calculating all pressure tensor components as functions of the spatial coordinates and of the value of angle θ.

Since the slit is assumed to be empty, the first term on the right-hand side of Eqn (10) disappears. We also include two following simplifications: (i) the consideration is restricted to the case with non-retarded dispersion forces Eqn (1); (ii) the interacting bodies are assumed to be solids with constant molecular number densities c_s, which makes it possible to set $\rho_{st}^{(2)} = \rho_s^{(1)}\rho_t^{(1)} = c_s c_t$. Then, passing to the pressure tensor and using cylindrical coordinates, Eqn (10) takes the form

$$\hat{p}(\mathbf{r}) = -\frac{15\pi A}{8}\int_{\varphi_1}^{\varphi_2} \mathrm{d}\varphi \hat{\kappa}(\varphi) \int_{\tilde{h}_1}^{\infty} \mathrm{d}r_1 \int_{\tilde{h}_2}^{\infty} \mathrm{d}r_2 \frac{1}{(r_1 + r_2)^5} \tag{24}$$

where

$$A \equiv \sum_{s,t} A_{st} c_s c_t \tag{24a}$$

$$\tilde{h}_1 \equiv \frac{h_1}{\sin(\varphi - \theta_1)} \tag{24b}$$

$$\tilde{h}_2 \equiv \frac{h_2}{\sin(\varphi + \theta_2)} \tag{24c}$$

and tensor $\hat{\kappa}(\varphi)$ has components

$$\kappa_{rr}(\varphi) = \cos^2\varphi \tag{25}$$

$$\kappa_{\varphi\varphi}(\phi) = \sin^2\varphi \tag{25a}$$

$$\kappa_{r\varphi}(\varphi) = \sin\varphi\cos\varphi \tag{25b}$$

$$\kappa_{zz}(\varphi) = \frac{1}{5} \tag{25c}$$

After integration by r_1 and r_2, the pressure tensor in Eqn (24) can be represented as

$$\hat{p}(r_0, \theta_1, \theta_2) = -\frac{5\pi A}{32 r_0^3 \sin^3\theta}\,\hat{I}(\theta_1, \theta_2) \tag{26}$$

where

$$\hat{I}(\theta_1, \theta_2) = \int_{\theta_1}^{\pi-\theta_2} \hat{\kappa}(\varphi)\frac{\sin^3(\varphi-\theta_1)\sin^3(\varphi+\theta_2)}{\sin^3\varphi}\,d\varphi \tag{27}$$

The integrals in Eqn (27) are easy to take. However, the resultant expressions are too bulky to be given here. In accordance with Eqn (25)–(25c), the diagonal components of the pressure tensor satisfy the condition

$$p_{\varphi\varphi} + p_{rr} = 5p_{zz} \tag{28}$$

In addition, Eqns (26) and (27) satisfy the conditions of mechanical equilibrium, Eqns (21)–(23). Taking into account the explicit dependence on r_0 for our case of a wedge-shaped slit, Eqns (21) and (22) can be written as

$$\frac{\partial p_{r\varphi}}{\partial\varphi} = 2p_{rr} + p_{\varphi\varphi} \tag{29}$$

$$\frac{\partial p_{\varphi\varphi}}{\partial\varphi} = p_{r\varphi} \tag{30}$$

When applying these formulas to the pressure tensor, the equalities should be used $\partial/\partial\varphi = \partial/\partial\theta_2 = -\partial/\partial\theta_1$.

At given angles, distance r_0 in Eqn (26) is proportional to the transverse slit size. This allows us to reformulate the results in the usual terms of the theory of films. We introduce the notion of the local width H of a wedge-shaped slit (analogous of the film thickness) as the length of the segment (between the slit walls) of a straight line perpendicular to the bisector of the dihedral angle and passing through the calculation point $\mathbf{r}(r_0, \theta_1)$ (Fig. 2).

Geometry sets the relationship

$$r_0\sin\theta = H\frac{\cos^2(\theta/2)}{\cos(\theta/2-\theta_1)} \tag{31}$$

Putting Eqn (31) transforms Eqn (27) as

$$\hat{p}(H, \theta_1, \theta_2) = -\frac{5\,A\pi\cos^3(\theta/2-\theta_1)}{32\,H^3\cos^6(\theta/2)}\,\hat{I}(\theta_1, \theta_2) \tag{32}$$

Now it can be seen from Eqn (32) that the inverse cubic dependence on the transverse size, which is typical of thin films, is also valid for a wedge-shaped slit.

We now consider in more detail the dependence of the pressure tensor on the slit angle θ. Herewith, one can either fix the distance to the edge of the slit or the local width H (see Fig. 2). Of these two ways of varying the angle θ, the first method is inconvenient in the region of small angles due to the apparent divergence of the factor $\sin^{-3}\theta$. The second method allows us to eliminate the divergence at $\theta = 0$. It is of note that distance changes with θ at a fixed local width. Throughout the rest of the range of change of θ, the first method with a constant r_0 is most suitable for analyzing the angular dependence of the pressure tensor because of the correct asymptotic behaviour of the pressure tensor at $\theta \to \pi$. Using Eqn (31), the pressure tensor can be written as

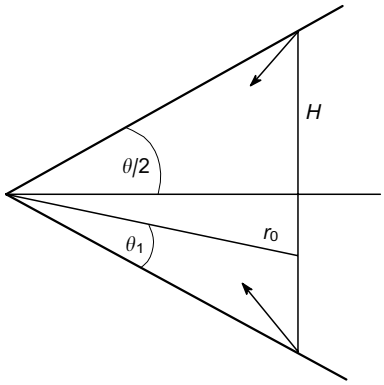


Figure 2. To the definition of the local width H of a wedge-shaped slit: the horizontal line is the bisector of the dihedral slit angle.[63]

$$\hat{p}(H, \theta, \theta_1) = -\frac{5\pi A}{32H^3}\,\hat{F}(\theta, \theta_1) \tag{33}$$

where

$$\hat{F}(\theta, \theta_1) \equiv \frac{\cos^3(\theta/2-\theta_1)}{\cos^6(\theta/2)}\,\hat{I}(\theta, \theta_1) \tag{34}$$

On the other side, we rewrite Eqn (32) in the form

$$\hat{p}(r_0, \theta_1, \theta_2) = -\frac{5\pi A}{32 r_0^3}\,\hat{J}(\theta, \theta_1) \tag{35}$$

where

$$\hat{J} \equiv \frac{\hat{I}}{\sin^3\theta} \tag{36}$$

So, with accuracy up to a constant factor, the dependence of the pressure tensor on the angle will be described by functions $\hat{F}$ at constant H or functions $\hat{J}$ at constant r_0. The equations obtained have a number of consequences. The expressions for the diagonal components are symmetric with respect to the dependence on angles θ_1 and θ_2. Since they are functions of two arguments, we will consider their dependence on θ at fixed values of θ_1 for the sake of simplicity. Then the expressions for the integrals become functions of a single variable θ and are greatly simplified. The diagonal components attain an extreme value at the plane passing through the bisector of angle θ where $\theta_1 = \theta/2$. All components of tensors $\hat{F}$ and $\hat{J}$ decrease with a growth in θ. This means a decrease of the absolute values of the pressure tensor components. Thus, the pressure tensor components, remaining negative, take minimum absolute values in the middle of the wedge-shaped slit.

The foregoing refers to the position of the calculation point on the bisector. Another interesting and practically important case is the position of the calculation point on the slit wall. For the sake of definiteness, we set $\theta_1 = 0$. The components of tensor $\hat{I}(\theta)$ become

$$I_{\varphi\varphi}(\theta) = \frac{16}{15}\cos^6\frac{\theta}{2} \tag{37}$$

$$I_{zz}(\theta) = \frac{4}{5}\cos^4\frac{\theta}{2}\left(1 - \frac{2}{3}\cos^2\frac{\theta}{2}\right) \tag{38}$$

$$I_{r\varphi}(\theta) = \frac{1}{5}\sin\theta(1+\cos\theta)^2 \tag{39}$$

The components of tensors $\hat{F}(\theta)$, Eqn (34), and $\hat{J}(\theta)$, Eqn (36), are shown in Fig. 3. In this case, the off-diagonal component of the pressure tensor appears too. To obtain the values of the components of the pressure tensor itself, the functions $F_{kl}(\theta)$ must be multiplied by $-(5\pi A/32)H^{-3}$, and the functions $J_{kl}(\theta)$ by $-(5\pi A/32)r_0^{-3}$. From Fig. 3, it can be seen that the absolute value of only the normal component of the pressure tensor on the wall decreases with increasing the slit angle over the entire range of its change (see Fig. 3). The absolute values of the tangential components, on the contrary, first increase with increasing angle and reach a maximum in the region of $\theta \cong \pi/2$, although the change in the normal (zz) component is rather small. The off-diagonal component also tends to a maximum at $\theta \cong 70^\circ$. In the region of large values of the angle (see Fig. 3 *b*), the diagonal components tend to zero, and the normal pressure decreases most rapidly to zero (see Fig. 3 *b*, curve *1*).

Generally, at a fixed local width, the normal pressure $p_N \equiv p_{zz}$ slightly changes within the angle range from 0 to 20° and then decreases almost linearly. Both tangential components are several times smaller than the normal one, almost coinciding with each other at $\theta < 20^\circ$. Then component p_{rr} decreases faster than $p_{\varphi\varphi}$. At a given distance to the z-axis, the components of the pressure tensor change more dramatically and already approach zero at 90°.

In the limit $\theta \to 0$, a wedge-shaped slit turns into a plane-parallel one, in which only the normal and tangential components of the pressure tensor become nonzero. Herewith, $r_0 \sin\theta$ tends to $h_1 + h_2$ where h_i is the distance between the calculation point and the ith slit wall (see Fig. 1). Considering the deviation from parallelism as a small value ($h_i/r_0 \ll 1$), we write down the expressions for the pressure tensor components with retaining only the first terms of the expansion in this ratio:

$$p_{\varphi\varphi} = -\frac{\pi A}{6H^3}\left(1 - \frac{3}{4}\frac{h_1^2 + h_2^2 + 3h_1h_2}{r_0^2}\right) \tag{40}$$

$$p_{rr} = -\frac{\pi A}{24H^3}\left(1 + 3\frac{h_1^2 + h_2^2 - 9h_1h_2/2}{r_0^2}\right) \tag{41}$$

$$p_{zz} = -\frac{\pi A}{24H^3}\left(1 - \frac{9h_1h_2}{2r_0^2}\right) \tag{42}$$

$$p_{r\varphi} = \frac{\pi A}{8H^3}\frac{h_1 - h_2}{r_0}\left(1 - \frac{3h_1^2 + 3h_2^2 - h_1h_2}{r_0^2}\right) \tag{43}$$

Checking Eqns (40)–(43) for compatibility with the mechanical equilibrium conditions shows the above limiting values of the components of the pressure tensor to satisfy Eqns (29) and (30).

It can be seen that the deviation from the parallelism of the slit walls, first, weakens their mutual dispersive attraction, since the multiplier in the parentheses in Eqn (40) is less than one. Second, the wedge-shaped slit leads to asymmetry in the tangential components. In the cross section of the wedge-shaped slit, the absolute values of the tangential components p_{rr} and p_{zz} can be both larger and smaller as compared with the values in a flat-parallel slit of the same width, depending on the position in the slit. So, on a bisector, these quantities decrease with an increase in the angle, and on the wall they exhibit a non-monotonic angular dependence, which is especially evident for p_{rr}. And, finally, a bright consequence of the non-parallelism of the walls is the occurrence of a radially directed force applied to the surface of the slit ($p_{\varphi r}$). By virtue of the condition of mechanical equilibrium, this leads to shear stresses in a solid with a nonzero value of the pressure tensor component $p_{r\varphi} \equiv p_{\varphi r}$ in a vacuum. In contrast to the other components, the shear component of the pressure tensor is more sensitive to the violation of parallelism of the slit walls, since it depends linearly on the smallness parameter h_i/r_0. In the opposite limiting case of the unfolded dihedral angle ($\theta = \pi$), one should expect the pressure tensor to vanish.

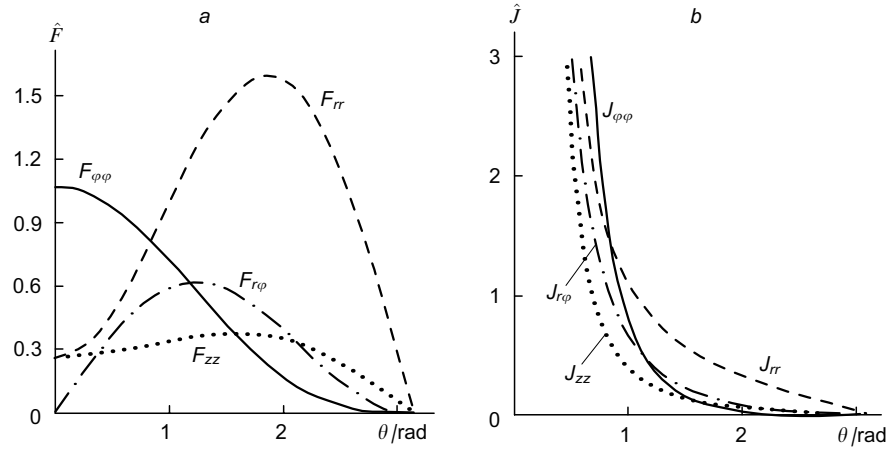


Figure 3. The dependence of the components of tensors $\hat{F}$ and $\hat{J}$ at the slit wall ($\theta_1 = 0$) on the slit angle θ for a fixed local width H (*a*) and for a fixed distance r_0 from the slit edge (*b*).[67]

2.2. Disjoining pressure

Historically, the concept of disjoining pressure was introduced for unrestricted plane-parallel films with a constant normal pressure inside.[7] The above example with a variable normal pressure suggests the need for generalizing the definition of disjoining pressure, especially as a local quantity. The idea is not new and was multiply discussed and reviewed in the literature.[7,8] The most universal and physically reasonable definition relates disjoining pressure to a difference between the local normal pressure on the solid surface itself p_{N}^{s} and the pressure p^{α} in the bulk mother phase α of a fluid inside the slit:[59–63]

$$\Pi \equiv p_{\mathrm{N}}^{s} - p^{\alpha} \tag{44}$$

If phase α is a vacuum, the disjoining pressure simply coincides with p_{N}^{s}.

In our case $p_{\mathrm{N}} \equiv p_{\varphi\varphi}(\theta_1)$ and $p_{\mathrm{N}}^{s} = p_{\varphi\varphi}(\theta_1 = 0)$. Therefore, we have

$$\Pi(\theta) \equiv p_{\varphi\varphi}(\theta_1 = 0) = -\frac{5\pi A F_{\varphi\varphi}}{32H^3} = \tag{45}$$

$$= -\frac{5\pi A I_{\varphi\varphi}}{32H^3\cos^3(\theta/2)} = -\frac{\pi A}{6H^3}\cos^3\frac{\theta}{2}$$

where Eqns (32) and (37) have been taken into account. This equation is valid for any $\theta < \pi$. On going to a plane-parallel slit ($\theta \to 0$), Eqn (45) takes the form

$$\Pi \equiv \Pi(\theta = 0) = -\frac{\pi A}{6H^3} \tag{46}$$

which corresponds to the ordinary disjoining pressure and for the one-component case coincides with Hamaker's Eqn (4). From Eqns (45) and (46), we obtain

$$\frac{\Pi(\theta)}{\Pi} = \cos^3\frac{\theta}{2} \tag{47}$$

Eqn (47) shows what error arises when the disjoining pressure of a flat film is used in the case of a wedge-shaped film of the same local thickness. The function (47) is monotonically decreasing, and, therefore, the disjoining pressure in the wedge-shaped slit is always less in absolute value than in a plane-parallel slit.The fact that function (46) as $\theta \to 0$ asymptotically approaches unity gives grounds for replacing $\Pi(\theta)$ by Π as an approximation for small θ. In this case, the admissible range of such an approximation is rather large: for $\theta < 20^{\circ}$, the deviation does not exceed 5%. A more general case of a slit between dissimilar solids was also considered.[65] The essential difference in the pressure tensor in such a system is the different values of the normal pressure on the two walls of the slit, which makes it difficult to determine the wedging pressure in it.

2.3. Interaction through a wedge-shaped fluid film

In contrast with the case of a pure solid system, a statistical theory of wedge-shaped slit in the presence of a fluid film inside the slit requires finding distribution functions. A corresponding consideration is presented below.

2.3.1. Distribution functions in a wedge-shaped fluid film

Let a fluid with bulk phase α enter a wedge-shaped slit in a solid with bulk phase β. To characterize the fluid in the slit, we have to calculate the distribution functions. According to the asymptotic principle[45–47] a rigorous analytical solution for distribution functions can be obtained only for sufficiently large distances (in comparison with the molecular dimensions) from the solid surface. On the basis of the asymptotic principle (Section 1), we obtain the following expression for the one-particle distribution function:[66]

$$\rho_p(\mathbf{r}_1) = \rho_p^{\alpha} + \frac{\pi}{12}\sum_{s,t} A_{st}\frac{\partial\rho_p^{\alpha}}{\partial\mu_s}\left(\rho_t^{\beta} - \rho_t^{\alpha}\right)\left[\frac{v(\theta_1)}{h_1^3} + \frac{v(\theta_2)}{h_2^3}\right] + \tag{48}$$

$$+\frac{\pi}{4}\sum_{s,t} A_{st}\frac{\partial\rho_p^{\alpha}}{\partial\mu_s}\left(\Gamma_t^{\alpha\beta} + \Gamma_t^{\beta\alpha}\right)\left[\frac{v(\theta_1)}{h_1^4} + \frac{v(\theta_2)}{h_2^4}\right]$$

or, using the relationship $h_k = r_0\sin\theta_k$,

$$\rho_p(\mathbf{r}_1) = \rho_p^{\alpha} + \frac{\pi}{12}\sum_{s,t} A_{st}\frac{\partial\rho_p^{\alpha}}{\partial\mu_s}\left(\rho_t^{\beta} - \rho_t^{\alpha}\right)\left[\frac{v(\theta_1)}{\sin^3\theta_1} + \frac{v(\theta_2)}{\sin^3\theta_2}\right]r_0^{-3} + \tag{49}$$

$$+\frac{\pi}{4}\sum_{s,t} A_{st}\frac{\partial\rho_p^{\alpha}}{\partial\mu_s}\left(\Gamma_t^{\alpha\beta} + \Gamma_t^{\beta\alpha}\right)\left[\frac{v(\theta_1)}{\sin^4\theta_1} + \frac{v(\theta_2)}{\sin^4\theta_2}\right]r_0^{-4}$$

where the single superscripts refer to bulk phases and double superscripts to their interface, p_t^r is the molecular number density of component t in phase r, $\Gamma_t^{\alpha\beta} + \Gamma_t^{\beta\alpha}$ is the total adsorption of component t on both sides of the interface, μ_s is the chemical potential of component s, and

$$v(\theta_k) \equiv 1 + \frac{3}{2}\cos\theta_k - \frac{1}{2}\cos^3\theta_k \quad (k = 1, 2) \tag{50}$$

A similar expression was also obtained for the dependence of the two-particle distribution function $\rho_{pq}(\mathbf{r}_1, \mathbf{r}_2)$ on $\mathbf{r}_0 = (\mathbf{r}_1 + \mathbf{r}_2)/2$ provided that $r_{12} = |\mathbf{r}_1 - \mathbf{r}_2|$ and $r_{12} \ll h_i$ ($i = 1, 2$). In our further calculations, because of the condition of weakening correlations, the product of the corresponding single-particle distribution functions $\rho_p(\mathbf{r}_1)\rho_q(\mathbf{r}_2)$ will be used instead of $\rho_{pq}(\mathbf{r}_1, \mathbf{r}_2)$.

When $\theta \to 0$, both angles θ_1 and θ_2 tend to zero. Then, by the definition expressed in Eqn (50), $v(\theta_k) \to 2$ ($k = 1, 2$), and Eqn (48) changes to an asymptotic formula for distribution functions in a plane-parallel liquid film. In a wedge-shaped film, the absolute values of the asymptotic contributions to the distribution functions, Eqn (49), at given distances from solid walls, will be less than in a plane-parallel film in the same solid body. At $\theta_k \ll 1$, when $\sin\theta_k \cong \theta_k$, it can be argued that the corrections for deviation of the walls from parallelism will be proportional to θ_k^4 or $(h_k/r_0)^4$ for both the principal and the asymptotic correction terms. According to the form of the function $v(\theta_k)$ in the region $\theta_k \leqslant \pi/6$, the effect of non-parallelism of the walls on the distribution functions is insignificant.

It was already noted above that the asymptotic formulas obtained are valid only at sufficiently large distances from the solid walls. Obviously, this condition will be observed at the middle section of the dihedral angle and far from its axis. Then $h_1 = h_2 = r_0\sin(\theta/2)$, and the angular dependences of the distribution functions for a given r_0 are determined by the following factors in brackets of Eqn (49):

$$f_1 \equiv 2\frac{v(\theta/2)}{\sin^3(\theta/2)} \quad (51)$$

$$f_2 \equiv 2\frac{v(\theta/2)}{\sin^4(\theta/2)} \quad (52)$$

As angle θ approaches zero, functions f_1 and f_2 diverge, and then it is more expedient to consider distribution functions depending on the distance to the slit walls according to Eqn (48).

In the case of a fixed distance r_0 to the axis, Eqn (49) for the distribution functions is a generalization of the results for a flat surface layer, which are obtained from the formulas for the bisector plane in the limit of the unfolded angle $\theta \to \pi$, when $v(\theta/2) \to 1$ and $\sin(\theta/2) \to 1$. The smaller the wedge angle of the slit, the greater in absolute value the asymptotic contributions to the distribution function for a given value of the distance to the axis of the wedge.

2.3.2. Pressure tensor

As in the case of an empty slit, the consideration is based on the Irving–Kirkwood stress tensor, Eqn (10).[67, 68] This time, however, the first term on the right-hand side of Eqn (10) is not zero because of a fluid present. Both the one- and two-particle distribution functions of the fluid are taken into account and are processed as was explained above. The result for the pressure tensor can be represented in two alternative forms, since all the components of the pressure tensor are functions of three arguments, which can be taken as θ, θ_1 and either the distance to the slit edge r_0 or the local slit width H (see Fig. 2). The relations between r_0, H, and the distances of the calculation point to the slit walls h_i ($i = 1, 2$) in variables θ and θ_i are set by the geometry of the system:

$$H = r_0\frac{\sin\theta_1 + \sin(\theta - \theta_1)}{\cos(\theta/2)} = 2r_0\tan(\theta/2)\cos(\theta/2 - \theta_1) \quad (53)$$

$$h_i = r_0\sin\theta_i = \frac{H\sin\theta_i}{2\tan(\theta/2)\cos(\theta/2 - \theta_1)} \quad (54)$$

Separating the dependence on angles and distances, the final formulas for the pressure tensor can be written in two alternative forms:

$$\hat{p} = \hat{p}^{\alpha} + \frac{C_1}{H^3}\left[\hat{F}_1(\theta_1) + \hat{F}_2(\theta_2)\right] + \frac{C_2}{H^3}\hat{F}_3(\theta, \theta_1) \quad (55)$$

$$\hat{p} = \hat{p}^{\alpha} + \frac{C_1}{r_0^3}\left[\hat{J}_1(\theta_1) + \hat{J}_2(\theta_2)\right] + \frac{C_2}{r_0^3}\hat{J}_3(\theta, \theta_1) \quad (56)$$

where

$$C_1 \equiv \pi\sum_{p,q} A_{pq}\left(\rho_p^{\beta} - \rho_p^{\alpha}\right)\rho_q^{\alpha}, C_2 \equiv \pi\sum_{p,q} A_{pq}\left(\rho_p^{\beta} - \rho_p^{\alpha}\right)\left(\rho_q^{\beta} - \rho_q^{\alpha}\right) \quad (57)$$

The tensorial functions $\hat{F}_i$ and $\hat{J}_i$ are defined by the following expressions:

$$\hat{F}_i(\theta, \theta_i) = \left[\frac{2\tan(\theta/2)\cos(\theta/2 - \theta_i)}{\sin\theta_i}\right]^3\left(\hat{1}\frac{v(\theta_i)}{12} - \frac{5\hat{I}_i(\theta_i)}{32}\right) \quad (58)$$

($i = 1, 2$)

$$\hat{F}_3(\theta, \theta_1) = \frac{\cos^3(\theta/2 - \theta_1)}{\cos^6(\theta/2)}\left(-\frac{5\hat{I}_3(\theta, \theta_1)}{32}\right) \quad (59)$$

$$\hat{J}_i(\theta_i) = \frac{1}{\sin^3\theta_i}\left(\hat{1}\frac{v(\theta_i)}{12} - \frac{5\hat{I}_i(\theta_i)}{32}\right) (i = 1, 2) \quad (60)$$

$$\hat{J}_3(\theta, \theta_1) = -\frac{5}{32}\frac{\hat{I}_3(\theta, \theta_1)}{\sin^3\theta} \quad (61)$$

Tensorial integrals $\hat{I}_i$ are defined as

$$\hat{I}_1(\theta_1) = \int_{\theta_1}^{\pi} \mathrm{d}\varphi\,\hat{\kappa}(\varphi)\,\sin^3(\varphi - \theta_1) \quad (62)$$

$$\hat{I}_2(\theta_2) = \int_{0}^{\pi-\theta_2} \mathrm{d}\varphi\,\hat{\kappa}(\varphi)\sin^3(\varphi + \theta_2) \quad (63)$$

$$\hat{I}_3(\theta_1, \theta_2) = \int_{\theta_1}^{\pi-\theta_2} \mathrm{d}\varphi\,\hat{\kappa}(\varphi)\,\frac{\sin^3(\varphi - \theta_1)\sin^3(\varphi + \theta_2)}{\sin^3\varphi} \quad (64)$$

Integral $\hat{I}_3(\theta_1, \theta_2)$ coincides with the integral in Eqn (27) and was considered in the previous section. The components of the first two tensorial integrals ($i = 1, 2$) are

$$I_{izz} = \frac{1}{5}\left(\frac{2}{3} + \cos\theta_i - \frac{1}{3}\cos^3\theta_i\right) \quad (65)$$

$$I_{i\varphi\varphi} = \frac{2}{15}(1 + \cos\theta_i)^3 \quad (66)$$

$$I_{irr} = \frac{8}{15} + \frac{3}{5}\cos\theta_i - \frac{2}{5}\cos^2\theta_i - \frac{7}{15}\cos^3\theta_i \quad (67)$$

$$I_{ir\varphi} = -\frac{1}{5}\sin\theta_i(1 + \cos\theta_i)^2 \quad (68)$$

As in the case of an empty slit, all the diagonal components of the pressure tensor are symmetric with respect to the median plane, whereas the non-diagonal component on the bisectorat $\theta_1 = \theta_2$ vanishes. Compared to a plane-parallel film, the corrections to the non-parallelism of the slit walls are opposite in sign to the main asymptotic terms in the expressions for the diagonal components of the tensor. Consequently, they will partially compensate for the main asymptotic contributions to the diagonal components of the pressure tensor. For small wedge angles, estimates are obtained for the effect of deviations from the film surface parallelism on the tensor components. The influence of the wedge-shape of a pore is practically negligible at $\theta \leqslant 20^\circ$ and very small at $\theta \leqslant 40^\circ$.

3. Conical surface

A cone-shaped cavity[69] can be considered as the first generalization for a cylindrical cavity in porous bodies, taking into account the deviation from parallelism of the generatrix. In addition, such systems arise with the growth of point defects from the surface into the solid bulk, which is characteristic of the process of destruction of solids. Consideration of such systems is similar to that carried out

above for the wedge-shaped slit filled with a fluid (Section 2.2). In the framework of the asymptotic approach, the computation program consists in finding all the components of the pressure tensor inside a cone-shaped cavity as functions of the spatial coordinates and the magnitude of the generatrix angle at a large distance from the vertex of the cone and from its walls. The cone is assumed to have an infinite smooth wall. All calculations are based on the local Irving–Kirkwood stress tensor and asymptotic expressions for the distribution functions.

In accordance with the symmetry of the problem, we choose the spherical coordinates r, ϑ, and φ. Denote the half-angle of the cone by θ. The position of the point in question in the wedge-shaped cavity is determined by its distance r_0 to the top of the cone and the angle θ_1 (Fig. 4). The origin of the spherical coordinates is placed at the point under consideration on a plane perpendicular to the vector **r**. The angle φ will be counted in this plane from the line connecting the point under consideration and the point of intersection of the plane with the axis of the cone (see Fig. 4).

The surface of the cone breaks the space into two parts. Denote the volume inside the cone as V_α and outside it as V_β. The asymptotic formula for the distribution function inside a cone-shaped cavity after a series of integrations takes the following form:

$$\rho_p(r,\theta_1,\theta) = \rho_p^\alpha + \frac{1}{3r^3}\sum_{s,t} A_{st}\frac{\partial\rho_p^\alpha}{\partial\mu_s}\left(\rho_t^\beta - \rho_t^\alpha\right) I_\rho(\theta_1,\theta) \tag{69}$$

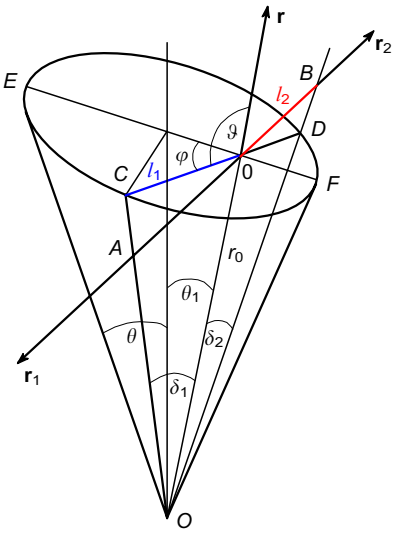


Figure 4. Cone-shaped cavity and its section passing through the end of vector **r** normal to it: O is the cone vertex; 0 is the origin of coordinates at the calculation point; A and B are the intersection points of the vectors $\mathbf{r}_1$ and $\mathbf{r}_2$ with the cone surface; C and D are the intersection points with the cone surface of the projections of vectors $\mathbf{r}_1$ and $\mathbf{r}_2$ onto the section plane; l_1 and l_2 are the lengths of the segments of vectors $\mathbf{r}_1$ and $\mathbf{r}_2$ equal to the distance from the origin of coordinates to points A and B, respectively; r_0 is the distance from the cone vertex to the point in question; θ is half the cone angle; θ_1 is the angle between the cone axis and vector **r**; ϑ is the angle between vector **r** and the CD line; φ is the angle between the section axis EF and the CD line intersecting this axis; δ_1 is the angle between vector **r** and the cone generatrix OC; and δ_2 is the angle between vector **r** and the cone generatrix OD.[69]

where

$$I_\rho(\theta_1,\theta) \equiv \int_0^{2\pi}\frac{\mathrm{d}\varphi}{\sin^3\delta_1}\int_{\delta_1}^{\pi}\sin\vartheta\sin^3(\vartheta-\delta_1)\mathrm{d}\vartheta \tag{70}$$

$$\sin\delta_{2,1} = \frac{\sin\theta_1\cos\theta\cos\varphi \pm \cos\theta_1(\sin^2\theta - \sin^2\theta_1\sin^2\varphi)^{1/2}}{1-\sin^2\theta_1\sin^2\varphi} \tag{71}$$

In Eqn (71), the top sign plus in the numerator refers to δ_2 and the sign minus to δ_1. Although the integral with respect to ϑ in Eqn (70) can be taken analytically, the result looks too cumbersome since angles δ_1 and δ_2 depend in a complex way on φ according to Eqn (71). Taking into account the subsequent integration over φ, the integral in Eqn (70) is taken numerically.

For the pressure tensor, we again select the Irving–Kirkwood expression, Eqn (10), and apply the same computational scheme as in the case of a wedge-shaped slit.[67] With the above choice of local coordinates in a cone-shaped cavity, the pressure tensor is of the structure

$$\hat{p} = \begin{pmatrix} p_{rr} & p_{r\vartheta} & 0 \\ p_{\vartheta r} & p_{\vartheta\vartheta} & 0 \\ 0 & 0 & p_{\varphi\varphi} \end{pmatrix} \tag{72}$$

with three diagonal and one off-diagonal component. The latter, $p_{r\vartheta}$, corresponds to shear stresses arising due to the external impact on the fluid phase varying along the surface. Finally, the formula for the pressure tensor after integration over r_1 and r_2 can be rewritten as

$$\hat{p} = \hat{p}^\alpha + \frac{C_1}{3r^3}I_\rho(\theta_1,\theta)\hat{1} - \frac{C_1}{2r^3}\left[\hat{I}_1(\theta_1,\theta) + \hat{I}_2(\theta_1,\theta)\right] - \frac{C_2}{2r^3}\hat{I}_3(\theta_1,\theta) \tag{73}$$

where

$$C_1 \equiv \sum_{p,q} A_{pq}(\rho_p^\beta - \rho_p^\alpha)\rho_q^\alpha, C_2 \equiv \sum_{p,q} A_{pq}\left(\rho_p^\beta - \rho_p^\alpha\right)\left(\rho_q^\beta - \rho_q^\alpha\right) \tag{74}$$

$$\hat{I}_1(\theta_1,\theta) = \int_0^{\pi}\frac{\mathrm{d}\varphi}{\sin^3\delta_1}\int_{\delta_1}^{\pi}\hat{\kappa}(\varphi,\vartheta)\sin\vartheta\sin^3(\vartheta-\delta_1)\,\mathrm{d}\vartheta \tag{75}$$

$$\hat{I}_2(\theta_1,\theta) = \int_0^{\pi}\frac{\mathrm{d}\varphi}{\sin^3\delta_2}\int_0^{\pi-\delta_2}\hat{\kappa}(\varphi,\vartheta)\sin\vartheta\sin^3(\vartheta+\delta_2)\,\mathrm{d}\vartheta \tag{76}$$

$$\hat{I}_3(\theta_1,\theta) = \int_0^{\pi}\frac{\mathrm{d}\varphi}{\sin^3(\delta_1+\delta_2)}\int_{\delta_1}^{\pi-\delta_2}\frac{\hat{\kappa}(\varphi,\vartheta)}{\sin^2\vartheta}\sin^3(\vartheta-\delta_1)\sin^3(\vartheta+\delta_2)\,\mathrm{d}\vartheta \tag{77}$$

and $\hat{\kappa}$ is a tensor whose components are

$$\kappa_{rr} = \cos^2\vartheta \tag{78}$$

$$\kappa_{\vartheta\vartheta} = \sin^2\vartheta\cos^2\varphi \tag{78a}$$

$$\kappa_{\varphi\varphi} = \sin^2\vartheta\sin^2\varphi \tag{78b}$$

$$\kappa_{r\vartheta} = \sin\vartheta\cos\vartheta\cos\varphi \tag{78c}$$

It should be noted again that the formulas obtained describe the local dependence of the components of the pressure tensor in a region sufficiently far from the top of

the cone and from its surface. Obviously, if these conditions are not met, the formulas obtained will lead to divergent values. This follows from such factors on the right-hand side of the formulas as r^{-3} and $\sin^{-3}\delta_i$. An alternative spatial behaviour of local functions can be characterized if, along with the angles θ and θ_1, we specify the radius a of a circular section passing through the point **r**. The quantities a and r are related as

$$r = \frac{\cos\theta}{\sin\theta\cos\theta_1}\, a \tag{79}$$

Then, to obtain the angular dependence of the quantities under consideration, each of the integrals must be multiplied, respectively, by $(\tan\theta\cos\theta_1)^3$. Using the quantities a, θ, and θ_1 to determine the spatial dependence of the pressure tensor components and the distribution functions is convenient in the case of small values of angle θ_1.

In the general case, the analytical calculation of all integrals is hampered by the fact that, as noted above, the values of angles δ_1 and δ_2, contained in the limits of the integrals over ϑ, are complex functions of φ, θ, and θ_1 according to Eqn (71). But the situation is simplified for points on the cone axis where $\theta_1 = 0$ and $\delta_1 = \delta_2 = \theta$. In addition, due to symmetry, the off-diagonal component disappears, and the two diagonal components become equal to each other, $p_{\vartheta\vartheta} = p_{\varphi\varphi}$. In the case of small values of θ_1, these two components are the normal pressure p_N whereas the p_{rr} component corresponds to the tangential pressure p_T. In this case, a number of integrals will be identical with those obtained in the case of a wedge-shaped slit (Section 2.2). Obviously, this will take place in a certain small region near the axis where the main dependence will be the dependence on θ. The smaller this angle, the greater will be the integral values because of factors $\sin^{-3}\delta_i$ standing before the integrals with respect to ϑ and being finite for any values of θ and θ_1. Therefore, in such cases it is more convenient to use the set of variables a, θ, and θ_1 since $\sin^3\theta\sin^{-3}\delta_i \to 1$ as $\delta_i \to \theta$, and, therefore, the divergence in the expressions disappears. In the limit $\theta \to 0$, we obtain the results for a cylindrical cavity of radius a, which coincides with the main asymptotic contributions to the components of the pressure tensor.[52] The limiting expressions for the normal and tangential pressures on the cylinder axis are

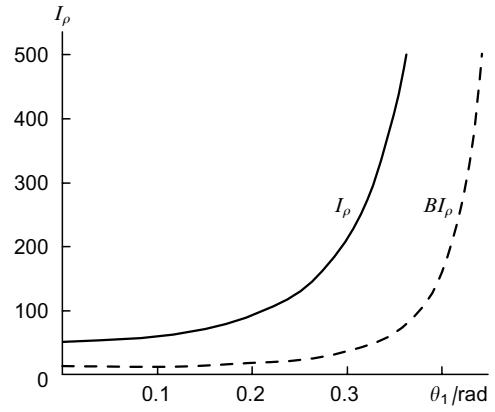


Figure 5. Spatial dependence of integrals I_ρ and BI_ρ characterizing the local density inside the cone-shaped cavity at $\theta = 30^\circ$.[69]

$$p_N = p^\alpha + \frac{\pi^2}{32a^3}\left(3C_1 - \frac{5}{16}C_2\right) \tag{80}$$

$$p_T = p^\alpha + \frac{\pi^2}{16a^3}\left(3C_1 - \frac{1}{16}C_2\right) \tag{81}$$

According to Eqn (74), the sign of the second term in Eqns (80) and (81) depends on the relative densities of the coexisting phases α and β. For a fluid in a solid cavity, an additional to p^α pressure will be positive if phase β is denser than phase α, and negative otherwise. At the same time, the additional term to p^α is larger (in absolute value) for the tangential pressure than for the normal one.

Due to the complexity of the expressions for the components of the pressure tensor in a cone-shaped pore, a detailed analysis of the angular dependence of the pressure tensor is easier to perform using numerical integration. It is obvious that such calculations can be carried out only by specifying the values of angles θ and θ_1 or r. Figures 5 and 6 show some of the angular dependences of the local density and the components of the pressure tensor on the position inside the cavity. The behaviour of local density characterizes the integrals I_ρ and BI_ρ. The dependence of the local density on the position in the cavity for a given value of $\theta = 30^\circ$ is shown in Fig. 5. The general nature of the

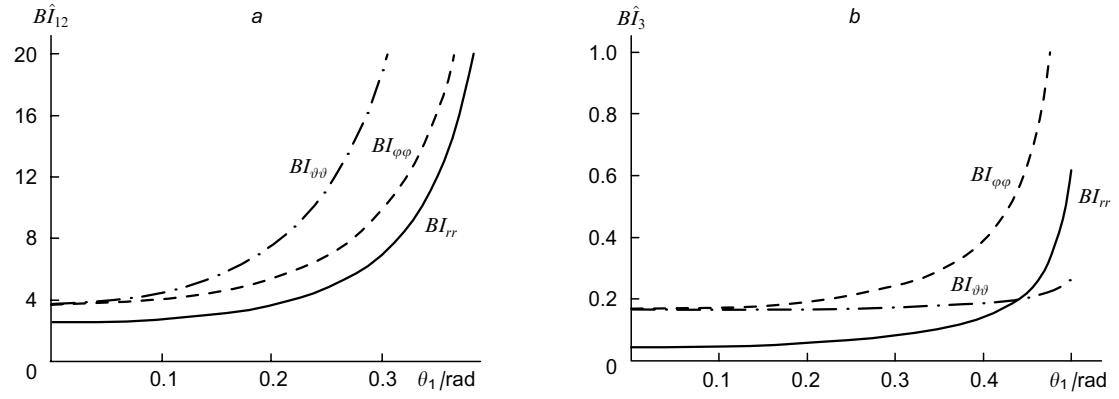


Figure 6. The dependence of the diagonal components of integrals $B\hat{I}_1$ and $B\hat{I}_2$ (*a*) and $B\hat{I}_3$ (*b*) on θ_1 at $\theta = 30^\circ$.[69]

angular dependence of both functions is the same, although the change in density at a fixed value of the section radius (BI_ρ) is much smaller in absolute value and is characterized by a slower increase when approaching the surface of the cavity.

The spatial dependence of the components of tensors $B\hat{I}_1$ and $B\hat{I}_2$ inside the cone-shaped cavity is represented in Fig. 6. It should be noted that to obtain the dependence of the pressure tensor itself, it is necessary to sum up the contributions from the local density, Eqn (69), and the tensors expressed in Eqns (75)–(76), multiplying them by the corresponding coefficients in accordance with the general expression (73). The type of dependences for all functions is the same and is characterized by a slow change in the paraxial region and divergence at $\theta_1 \to \theta$. In this case, the contribution is significantly larger from $B(\hat{I}_1 + \hat{I}_2)$ than from $B\hat{I}_3$. It should be said that by the degree of closeness of the values of the components $\vartheta\vartheta$ and $\varphi\varphi$, it is possible to determine the region where it is permissible to use the simple formulas of the cylindrical approximation, Eqns (80) and (81). In this example, $\theta_1 < 0.15$ radians.

In conclusion, it can be said that the main conclusion from the calculation carried out is the statement that a significant contribution of deviations of pore shape from cylindrical to local density and pressure tensor is observed when the cone angle exceeds 0.2 radians, which is about 10°.

4. Parallel semi-infinite flat surfaces

Considering non-parallel semi-infinite flat surfaces and a wedge-shaped slit with angle θ (Section 2), we found that passing to the limit of parallel surfaces ($\theta \to 0$) yields not semi- but fully-infinite surfaces. In other words, the case of parallel semi-infinite flat surfaces cannot be a particular case of non-parallel semi-infinite flat surfaces and requires separate consideration. The case is well illustrated by Fig. 7 depicting the end of a plane-parallel slit of width H between interacting bodies where the point for calculating the pressure tensor is at distances h and s from the slit walls ($H = h + s$) and x is the distance to the slit end. Considering this point as an origin of the Cartesian coordinates, vectors $\mathbf{r}_1$ and $\mathbf{r}_2$ indicate incidental locations of two interacting molecules.

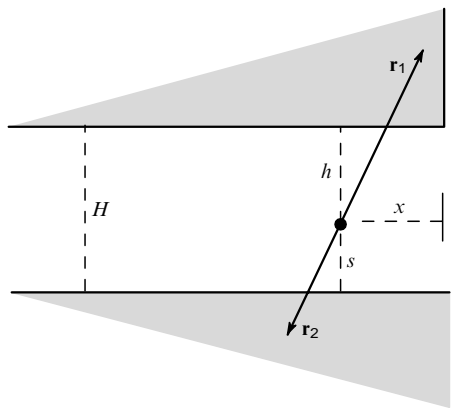


Figure 7. The end of a plane-parallel slit of width H with a point where the pressure tensor is calculated at distances h and s from the slit walls and distance x from the slit end, vectors $\mathbf{r}_1$ and $\mathbf{r}_2$ indicating the positions of interacting molecules.[70]

4.1. Pressure tensor

Comparing with the case of infinite surfaces, the pressure tensor becomes more complicated to the form

$$\hat{p} = \begin{pmatrix} p_{xx} & 0 & p_{xz} \\ 0 & p_{yy} & 0 \\ p_{zx} & 0 & p_{zz} \end{pmatrix} \tag{82}$$

so that the four pressure tensor components (including the off-diagonal component $p_{xz} = p_{zx}$ provided the z-axis is directed normally to the surfaces) should be calculated. The problem was solved [70, 71] using the following simplifications: the interaction occurs in a vacuum [then the first term on the right-hand side of Eqn (10) disappears] and with non-retarded dispersion forces [$\lambda = 6$ in Eqn (13)]; both interacting bodies are solids with constant molecular number densities c_s so that $\rho_{st}^{(2)} = \rho_s^{(1)}\rho_t^{(1)} = c_s c_t$. The resultant expressions are

$$p_{xx} = -\frac{15\pi}{32} A \left\{ \int_h^\infty \frac{\mathrm{d}z_1}{(z_1+s)^4} \left[\frac{x^3}{3(z_1^2+x^2)^{3/2}} - \frac{x^5}{5(z_1^2+x^2)^{5/2}} \right] + \right.$$
$$\left. + \int_{-\infty}^{-s} \frac{\mathrm{d}z_2}{(h-z_2)^4} \left[\frac{x^3}{3(z_2^2+x^2)^{3/2}} - \frac{x^5}{5(z_2^2+x^2)^{5/2}} \right] \right\} \tag{83}$$

$$p_{yy} = -\frac{3\pi}{32} A \left\{ \int_h^\infty \frac{\mathrm{d}z_1}{(z_1+s)^4} \left[\frac{x}{(z_1^2+x^2)^{1/2}} - \frac{x^3}{3(z_1^2+x^2)^{3/2}} \right] + \right.$$
$$\left. + \int_{-\infty}^{-s} \frac{\mathrm{d}z_2}{(h-z_2)^4} \left[\frac{x}{(z_2^2+x^2)^{1/2}} - \frac{x^3}{3(z_2^2+x^2)^{3/2}} \right] \right\} \tag{84}$$

$$p_{zz} = -\frac{15\pi}{32} A \left\{ \int_h^\infty \frac{\mathrm{d}z_1}{(z_1+s)^4} \left[\frac{x}{(z_1^2+x^2)^{1/2}} - \frac{2x^3}{3(z_1^2+x^2)^{3/2}} + \right.\right.$$
$$\left. + \frac{x^5}{5(z_1^2+x^2)^{5/2}} \right] + \int_{-\infty}^{-s} \frac{\mathrm{d}z_2}{(h-z_2)^4} \left[\frac{x}{(z_2^2+x^2)^{1/2}} - \right.$$
$$\left.\left. - \frac{2x^3}{3(z_2^2+x^2)^{3/2}} + \frac{x^5}{5(z_2^2+x^2)^{5/2}} \right] \right\} \tag{85}$$

$$p_{xz} = \frac{3\pi}{32} A \left[\int_h^\infty \frac{z_1^5 \mathrm{d}z_1}{(z_1+s)^4 (z_1^2+x^2)^{5/2}} + \right.$$
$$\left. + \int_{-\infty}^{-s} \frac{z_2^5 \mathrm{d}z_2}{(h-z_2)^4 (z_2^2+x^2)^{5/2}} \right] \tag{86}$$

where $A \equiv \sum_{s,t} A_{st} c_s c_t$. Since the integration in Eqns (83)–(86) required special procedures and would lead to cumbersome expressions, it was reasonable to retain Eqns (83)–(86) as the most compact forms of representation for all nonzero components of the pressure tensor.

According to Eqns (83)–(86), all of the pressure tensor components are dependent on distance x. As it should be, the diagonal components in Eqn (82) become equal to zero at the slit edge ($x = 0$). In the opposite limit $x \to \infty$, in both the integrals of Eqn (85) for the normal pressure $p_N \equiv p_{zz}$, the sum in brackets yields 8/15. Then, after integration, we obtain

$$p_{\mathrm{N}} = -\frac{\pi A}{6H^3} \tag{87}$$

which corresponds to Eqn (4). Similarly, in the same limit $x \to \infty$, the diagonal components in Eqns (83) and (84) become equal and identical to yield the tangential pressure $p_T \equiv p_{xx} = p_{yy}$ as

$$p_{\mathrm{T}} = -\frac{\pi A}{24H^3} \tag{88}$$

which is also a well-known result for infinite surfaces. This result shows that not only normal but also tangential pressure is independent of the location inside an empty infinite slit (another case is for a filled slit).

Turning now to the off-diagonal component, Eqn (86), we have, first of all, to realize the difference in signs of z_1 and z_2. In fact, there is not a sum but a difference in the brackets. One can see that p_{xz} becomes zero not only at $x = 0$ and, evidently, at $x = \infty$, but also in the general case at $s = h$ for any $x \geqslant 0$. The latter follows from the symmetry that appears when the calculation point is equally far from the slit walls. It is of note that the very fact of existence of the off-diagonal component has important implications for the normal pressure. In the case under consideration, the mechanical equilibrium condition, Eqn (11), yields

$$\frac{\partial p_{zz}}{\partial z} + \frac{\partial p_{xz}}{\partial x} = 0 \tag{89}$$

Since p_{xz} is dependent on x, p_{zz} can no longer be constant along the z-axis according to Eqn (59), though the derivative $\partial p_{zz}/\partial z$ becomes zero at the middle plane of the slit.

4.2. Disjoining pressure

Similarly to the case of non-parallel semi-infinite surfaces (Section 2), we now have a variable normal pressure at the slit end. Therefore, there is again a need for generalizing the definition of disjoining pressure. Taking the definition given in Eqn (44), we can write it, in our case ($p^{\alpha} = 0$), as

$$\Pi = p_{zz}|_{h \oplus s = 0} \tag{90}$$

We already have an expression for p_{zz}. Setting first $s = 0$ (then $h = H$) and putting Eqn (85) in Eqn (90), we have

$$\Pi = -\frac{15\pi}{32} A \left\{ \int_H^{\infty} \frac{\mathrm{d}z_1}{z_1^4} \left[\frac{x}{(z_1^2 + x^2)^{1/2}} - \frac{2x^3}{3(z_1^2 + x^2)^{3/2}} + \right. \right. \tag{91}$$

$$\left. + \frac{x^5}{5(z_1^2 + x^2)^{5/2}} \right] + \int_{-\infty}^{-s} \frac{\mathrm{d}z_2}{(h - z_2)^4} \left[\frac{x}{(z_2^2 + x^2)^{1/2}} - \right.$$

$$\left. \left. - \frac{2x^3}{3(z_2^2 + x^2)^{3/2}} + \frac{x^5}{5(z_2^2 + x^2)^{5/2}} \right] \right\}$$

Although the variables in both integrals are different, the same function appears in square brackets. Denoting it by f, we write Eqn (91) in the form

$$\Pi = -\frac{15\pi}{32} A \left[\int_H^{\infty} \frac{\mathrm{d}z_1}{z_1^4} f(z_1) + \int_{-\infty}^{0} \frac{\mathrm{d}z_2}{(H - z_2)^4} f(z_2) \right] \tag{92}$$

Alternatively, we can set $h = 0$ (then $s = H$) to determine the disjoining pressure on the opposite wall of the slit as

$$\Pi = -\frac{15\pi}{32} A \left[\int_0^{\infty} \frac{dz_1}{(z_1 + H)^4} f(z_1) + \int_{-\infty}^{-H} \frac{\mathrm{d}z_2}{z_4^2} f(z_2) \right] \tag{93}$$

Formally, Eqns (92) and (93) refer to different surfaces, which, as already noted, may also have a different nature. It is easy to show, however, that Eqns (92) and (93) are identical. To do this, it is enough to replace the variable z_2 with $-z_2$ and take into account that the function f is even. This proves that the disjoining pressure on the opposite walls of the slit is the same, and the symmetry of the dependence of p_{zz} on z relative to the median plane is confirmed.

For definiteness, we will address Eqns (91) and (92) for further calculations. The first integral in it is easily taken, and the second is just as complex as the integrals in Eqns (83)–(86), which give (in the strict version) difficult-to-see cumbersome results. There is only one way out, the choice of an approximate approach with the least possible loss of accuracy. As already noted, in the limit $x \to \infty$ functions $f(z_1)$ and $f(z_2)$ take the same value of 8/15. Therefore, one can search for a small parameter when considering the difference of the functions. To begin with, we combine both the integrals in Eqn (92) into one. For this purpose, we introduce a new variable $\zeta \equiv H - z_2$ in the second integral and perform the transformation

$$\int_{-\infty}^{0} \frac{\mathrm{d}z_2}{(H - z_2)^4} f(z_2) = \int_H^{\infty} \frac{\mathrm{d}\zeta}{\zeta^4} f(H - \zeta) = \int_H^{\infty} \frac{\mathrm{d}\zeta}{\zeta^4} f(\zeta - H) \tag{94}$$

the transition to the third record being due to the parity of the function f. Substituting Eqn (94) into Eqn (93) and passing to the general impersonal variable z, we get

$$\Pi = -\frac{15\pi}{32} A \int_H^{\infty} \frac{\mathrm{d}z}{z^4} \left[f(z) + f(z - H) \right] \tag{95}$$

Functions $f(z)$ and $f(z - H)$ in Eqn (95) are given by the expressions

$$f(z) \equiv \frac{x}{(z^2 + x^2)^{1/2}} - \frac{2x^3}{3(z^2 + x^2)^{3/2}} + \frac{x^5}{5(z^2 + x^2)^{5/2}} \tag{96}$$

$$f(z - H) \equiv \frac{x}{\left[(z - H)^2 + x^2 \right]^{1/2}} - \tag{97}$$

$$- \frac{2x^3}{3\left[(z - H)^2 + x^2 \right]^{3/2}} + \frac{x^5}{5\left[(z - H)^2 + x^2 \right]^{5/2}}$$

Let us consider the sum of functions $f(z) + f(z - H)$ term by term. The sum of the first terms in Eqns (96) and (97) can be written in the form

$$\frac{x}{(z^2 + x^2)^{1/2}} \left\{ 1 + \left[1 + \frac{2zH - H^2}{(z - H)^2 + x^2} \right]^{1/2} \right\} = \tag{98}$$

$$= \frac{x}{(z^2 + x^2)^{1/2}} \left\{ 1 + \left[1 + \frac{2\tilde{z} - 1}{(\tilde{z} - 1)^2 + \tilde{x}^2} \right]^{1/2} \right\}$$

where we marked with a wave dimensionless quantities measured in units of H ($\tilde{z} > 1$ in accordance with the limits of integration). Just here a small parameter is revealed

$$\delta \equiv \frac{2\tilde{z} - 1}{(\tilde{z} - 1)^2 + \tilde{x}^2} \tag{99}$$

whose smallness is due to the fact that variable $\tilde{z}$ in the numerator is raised to the first power, whereas $\tilde{z}$ and $\tilde{x}$ in the denominator is raised to the second power. For a given $\tilde{x}$, function $\delta(\tilde{z})$ is characterized by a single maximum in the region of small values of $\tilde{z}$. The maximum height decreases, and its position shifts towards larger values of $\tilde{z}$ with an increase in $\tilde{x}$. Even when $\tilde{x} = 3$, the maximum value of δ is only 0.39, and its average value (which could be taken out of the integral sign according to the average theorem) is much less. Therefore, we can conclude that in the zero approximation, we can neglect the parameter δ in comparison with unity and set the value in curly brackets in Eqn (98) equal to two.

The same small parameter δ, Eqn (99), arises in the pairwise summation of the second and third terms of Eqns (96) and (97). Then we can say that the sum of the functions $f(z) + f(z - H)$ can be replaced in the zero approximation by the double value of $f(z)$. As a result, we can formulate the zero approximation for the disjoining pressure at the edge of the plane-parallel slit as

$$\Pi = -\frac{15\pi}{16} A \int_H^\infty \frac{\mathrm{d}z}{z^4} f(z) \tag{100}$$

Putting Eqn (96) in Eqn (100) and carrying out the integration, we obtain

$$\Pi = -\frac{\pi A}{6x^3}\left[\frac{(x^2 + H^2)^{3/2}}{H^3} - \frac{3(x^2 + H^2)^{1/2}}{2H} - \frac{1}{4} + \right. \tag{101}$$
$$\left. + \frac{3H}{8(x^2 + H^2)^{1/2}} + \frac{3H^3}{8(x^2 + H^2)^{3/2}}\right]$$

or, passing to dimensionless variable $\tilde{x} \equiv x/H$,

$$\Pi = -\frac{\pi A}{6H^3\tilde{x}^3}\left[(\tilde{x}^2 + 1)^{3/2} - \frac{3}{2}(\tilde{x}^2 + 1)^{1/2} - \right. \tag{102}$$
$$\left. - \frac{1}{4} + \frac{3}{8}(\tilde{x}^2 + 1)^{-1/2} + \frac{3}{8}(\tilde{x}^2 + 1)^{-3/2}\right]$$

As $\tilde{x} \to \infty$, only $\tilde{x}^3$ remains in the square brackets in Eqn (102), and the disjoining pressure takes on the value known for an infinitely long slit, Eqn (4). Denoting this limiting value as Π_∞, we can write Eqn (102) in the dimensionless form

$$\frac{\Pi}{\Pi_\infty} = \frac{1}{\tilde{x}^3}\left[(\tilde{x}^2 + 1)^{3/2} - \frac{3}{2}(\tilde{x}^2 + 1)^{1/2} - \frac{1}{4} + \right. \tag{103}$$
$$\left. + \frac{3}{8}(\tilde{x}^2 + 1)^{-1/2} + \frac{3}{8}(\tilde{x}^2 + 1)^{-3/2}\right]$$

The plot of dependence of Π/Π_∞ on $\tilde{x}$ (Fig. 8) shows that the disjoining pressure at the slit edge takes a constant value practically at $\tilde{x} > 3$. Nevertheless, one has to remember that Eqn (103) is asymptotic and the grater $\tilde{x}$, the more accurate the equation.

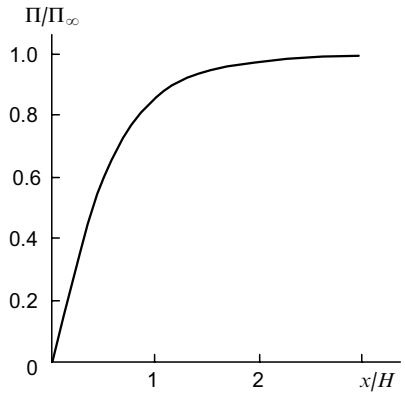


Figure 8. The plot of Π/Π_∞ *vs.* $\tilde{x}$.[71]

5. Interactions with participation of nanoparticles

Theoretically, considering a nanoparticle means, first of all, accounting for a finite size of the particle. In our case of analyzing interactions, this causes the appearance of two additional factors. While the interaction of macroscopic bodies of a given nature is determined by their separation, the interaction with participation of nanoparticles also depends on their contact surface area and particle dimensions. With this in mind, for example, we can qualify the interaction between a nanoparticle and a macroscopic body as an interaction between finite and infinite surfaces with at least one additional parameter (say, the particle size at a given particle shape). In connection with the peculiarities of nanoparticles, nanoscience compared to the classical colloid science, formulates quite new problems. Among them, there is finding the dependence of the disjoining pressure of a film (as average normal pressure) not only on the film thickness, but also on the film area.

Considering interactions with participation of nanoparticles, we introduce the following simplifications. First, we assume the particle contact surface to be circular. Second, we assume interacting surfaces to be parallel. This gives the whole system a cylindrical symmetry and facilitates the calculations. In addition, within the cylindrical symmetry, we can develop theory both for rod- and disk-shaped nanoparticles, which belong to the most important objects of nanoscience.

5.1. Interaction between finite and infinite surfaces

In this section, we consider the interaction between the circular end face of a cylindrical particle and the plane infinite surface of a macroscopic body. The case automatically includes rod- and disk-shaped particles, but first we consider, as a preliminary, the simplest example of a cylinder with an infinite length.

5.1.1. Cylinder of an infinite length

Let us consider the interaction of a semi-infinite nanocylinder (body *1*) with a macroscopic solid (body *2*) located so that the cylinder axis is perpendicular to the flat infinite surface of the solid (Fig. 9). A round nano-slit with a radius equal to the cylinder radius a, is formed between the two

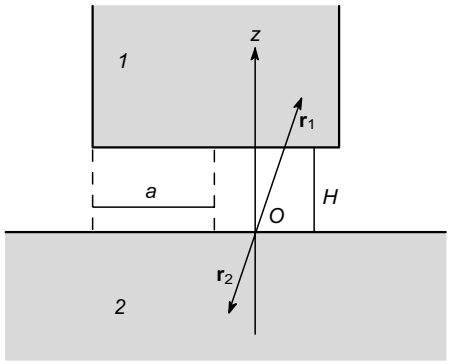


Figure 9. Plane-parallel slit between the cylinder end face and an infinite plane: a is the cylinder radius and H is the slit width, vectors $\mathbf{r}_1$ and $\mathbf{r}_2$ determine the location of interacting molecules with respect to the point of calculation.[72]

surfaces. In such a system, there is no longitudinal symmetry plane typical of flat films. Therefore, we will call this slit asymmetric. In this case, the normal pressure cannot be constant and equal on the opposite sides of the slit. This can be illustrated, for example, by the mechanical equilibrium condition. Using Cartesian coordinates with the z-axis normal to the surfaces, we obtain from Eqn (11)

$$\frac{\partial p_{xz}}{\partial x}+\frac{\partial p_{yz}}{\partial y}+\frac{\partial p_{zz}}{\partial z}=0 \tag{104}$$

Since the first two derivatives on the right-hand side of Eqn (104) are non-zero because of asymmetry, the third derivative is non-zero too. This means that the normal pressure $p_N \equiv p_{zz}$ is dependent on z and, as a consequence, has different values on the opposite sides of the slit. The spatial distribution of the pressure tensor components seems to be more complex in the case under consideration, and this was confirmed by direct calculations.[72, 73] Some results of calculations are presented below.

5.1.1.1. Pressure tensor in an asymmetric empty slit

For a system with a cylindrical symmetry, it is natural to use cylindrical coordinates r, φ, z with the z-axis coinciding with the symmetry axis. We have already considered the pressure tensor in cylindrical coordinates in Section 2.1. Now, however, the pressure tensor has a different structure as

$$\hat{p}=\begin{pmatrix} p_{rr} & 0 & p_{rz} \\ 0 & p_{\varphi\varphi} & 0 \\ p_{zr} & 0 & p_{zz} \end{pmatrix} \tag{105}$$

with three diagonal components (the normal component $p_N \equiv p_{zz}$ and two tangential components p_{rr} and $p_{\varphi\varphi}$) and the off-diagonal component $p_{rz}=p_{zr}$. Correspondingly, the mechanical equilibrium condition, Eqn (11) yields

$$\frac{\partial p_{\mathrm{rr}}}{\partial r}+\frac{p_{rr}-p_{\varphi\varphi}}{r}=0 \tag{106}$$

$$\frac{1}{r}\frac{\partial (r p_{rz})}{\partial r}+\frac{\partial p_{zz}}{\partial z}=0 \tag{107}$$

$$\frac{\partial p_{\varphi\varphi}}{\partial \varphi}=0 \tag{108}$$

When calculating the pressure tensor, we will proceed from Eqn (10), in which, taking into account a vacuum between the bodies, only the second term remains. In the latter, the two-particle distribution function $\rho_{st}^{(2)}$ is replaced by the product of the single-particle distribution functions $\rho_s^{(1)}\rho_t^{(1)}=c_s c_t$ where c_s is a constant particle density in the solid (assumed to be quite uniform). In addition to the above cylindrical coordinates, we now introduce the Cartesian coordinates with the origin at the calculation point O on one of the slit walls and with the z-axis parallel to the cylinder axis (see Fig. 9). The positions of two interacting molecules, one of which is located in body 1 (the cylinder) and the other in body 2, is characterized by the vectors $\mathbf{r}_1$ and $\mathbf{r}_2$. Obviously, they are directed oppositely, but lie on one straight line, since a straight line segment of length R connecting two interacting molecules must pass through the calculation point (see Fig. 9).

Let us replace variables $\mathbf{R}$ and η by x_1, y_1, z_1 (the components of vector $\mathbf{r}_1$) and z_2 (the z-component of vector $\mathbf{r}_2$). Denoting the volumes of the bodies as V_1 and V_2, taking into account Eqn (1) for the potential of dispersion forces Φ_{st}, we write the expression for the pressure tensor

$$\hat{p} \;=\; -6\sum_{s,t} A_{st}c_s c_t \int\limits_{V_1} \frac{\mathbf{r}_1\times\mathbf{r}_1}{r_1^8} z_1^4 \mathrm{d}\mathbf{r}_1 \int\limits_{V_2} \frac{\mathrm{d}z_2}{(z_1-z_2)^4} \tag{109}$$

For our purposes, it is more convenient to represent the components of tensor $\mathbf{r}_1\times\mathbf{r}_1$ in cylindrical coordinates whose origin coincides with the calculation point. Retaining r as the distance from the calculation point to the symmetry axis, we denote the cylindrical coordinates as ρ, φ, z. The diagonal components of tensor $\mathbf{r}_1\times\mathbf{r}_1$ are

$$[\mathbf{r}_1\times\mathbf{r}_1]_{zz}=z_1^2 \tag{110}$$

$$[\mathbf{r}_1\times\mathbf{r}_1]_{rr}=\rho^2\cos^2\varphi \tag{110a}$$

$$[\mathbf{r}_1\times\mathbf{r}_1]_{\varphi\varphi}=\rho^2\sin^2\varphi \tag{110b}$$

and the off-diagonal components are

$$[\mathbf{r}_1\times\mathbf{r}_1]_{rz}=z_1\rho\,\cos\varphi \tag{111}$$

$$[\mathbf{r}_1\times\mathbf{r}_1]_{z\varphi}=z_1\rho\,\sin\varphi \tag{111a}$$

$$[\mathbf{r}_1\times\mathbf{r}_1]_{r\varphi}=\rho^2\cos\varphi\,\sin\varphi \tag{111b}$$

Like in the previous section, we introduce the notation $A\equiv\sum_{s,t}A_{st}c_s c_t$. With this notation and accounting for Eqns (110) and (111), the expressions for the components of the pressure tensor following from Eqn (109) become

$$p_{zz}(H,r,a)=-6A\int\limits_{V_1}\mathrm{d}\varphi\rho\mathrm{d}\rho\mathrm{d}z_1\frac{z_1^6}{(\rho^2+z_1^2)^4}\int\limits_{V_2}\frac{\mathrm{d}z_2}{(z_1-z_2)^5} \tag{112}$$

$$p_{rr}(H,r,a)=-6A\int\limits_{V_1}\cos^2\varphi\mathrm{d}\varphi\rho^3\mathrm{d}\rho\mathrm{d}z_1\frac{z_1^4}{(\rho^2+z_1^2)^4}\int\limits_{V_2}\frac{\mathrm{d}z_2}{(z_1-z_2)^5} \tag{113}$$

$$p_{\varphi\varphi}(H,r,a) = -6A \int\limits_{V_1} \sin^2\varphi \mathrm{d}\varphi\rho^3\mathrm{d}\rho\mathrm{d}z_1 \frac{z_1^4}{(\rho^2+z_1^2)^4} \int\limits_{V_2} \frac{\mathrm{d}z_2}{(z_1-z_2)^5} \tag{114}$$

$$p_{rz}(H,r,a) = -6A \int\limits_{V_1} \cos\varphi \mathrm{d}\varphi\rho^2\mathrm{d}\rho \frac{z_1^5}{(\rho^2+z_1^2)^4} \int\limits_{V_2} \frac{\mathrm{d}z_2}{(z_1-z_2)^5} \tag{115}$$

When considering a point at the end face of the cylinder and at the infinite wall, the expressions for the pressure tensor will differ only in the limits of integration. The regions of variation of polar coordinates ρ and φ are shown in Fig. 10.

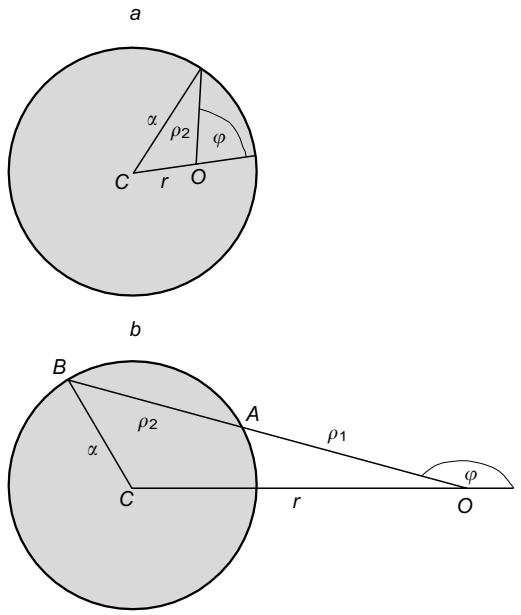


Figure 10. To the calculation of the pressure tensor components on the cylinder end face (*a*) and on the opposite infinite wall (*a*, *b*) of the slit: *C* is the central point of the cylinder face, *O* is the cylindrical coordinate system origin at the point of calculation, *a* is the cylinder radius, *r* is the distance between the point of calculation and the central point, and ρ_1 and ρ_2 are the lower and upper limiting values of cylindrical coordinate ρ; Fig. 10 *a* and Fig. 10 *b* are the cases with $r < a$ and $r > a$, respectively.[72]

In the choice of the limits of integration, the difference between the choice of a point on the end face of the cylinder or on the infinite wall of body *2* is clearly visible, since in the latter case the point may be outside the slit itself (see Fig. 10 *b*). It should be established that φ is measured from a straight line passing through the calculation point *O* (which is the origin of coordinates) and the central point *C* of the slit on a solid surface. The slit asymmetry also influences the range of variation of coordinates ρ and φ. Marking lower and upper limits with subscripts 1 and 2, respectively, we can write

$$\rho_1 \leqslant \rho \leqslant \rho_2 \tag{116}$$

$$\varphi_1 \leqslant \varphi \leqslant \varphi_2 \tag{116a}$$

If the distance of the calculation point to the cylinder axis on any of the surfaces is smaller than the cylinder radius ($r < a$), we have the limiting values (see Fig. 10 *a*).

$$0 \leqslant \rho \leqslant -r\cos\varphi + \sqrt{a^2 - r^2\sin^2\varphi} \tag{117}$$

$$0 \leqslant \varphi \leqslant 2\pi \tag{117a}$$

If the point is on the infinite surface of a solid with $r > a$, the limiting values are (Fig. 10 *b*)

$$-r\cos\varphi - \sqrt{a^2 - r^2\sin^2\varphi} \leqslant \rho \leqslant -r\cos\varphi + \sqrt{a^2 - r^2\sin^2\varphi} \tag{118}$$

$$\pi - \arcsin\frac{a}{r} \leqslant \varphi \leqslant \pi + \arcsin\frac{a}{r} \tag{118a}$$

For further formulation, it is also convenient to introduce dimensionless quantities $x_1 \equiv \rho_1/H$, $x_2 \equiv \rho_2/H$.

5.1.1.2. Local normal pressure

Let us consider in more detail the local behaviour of the normal component of the pressure tensor $p_N \equiv p_{zz}$, Eqn (112), on both contact surfaces.[72,73] Integration over z_1 and z_2 is easy in both cases. For the cylinder end face, the final formula for the normal component of the pressure tensor is

$$p_{\mathrm{N}}(r,H,a) = -\frac{\pi A}{6H^3}[1 - f_{\mathrm{N}}(r,H,a)] \tag{119}$$

where

$$f_{\mathrm{N}}(r,H,a) = \frac{3}{16\pi}\int\limits_0^{2\pi} F_1(x_2)\mathrm{d}\varphi \tag{120}$$

$$F_1(x) \equiv \frac{1}{6(1+x^2)^6}\left[16 - 768x^2 + 288x^4 + \right. \tag{121}$$

$$+ 1024x^6 - 48x^8 + \pi(3x^9 + 108x^7 - 990x^5 + 780x^3 - 45x) -$$

$$\left. -(960x^6 - 2304x^4 + 576x^2)\ln x\right]$$

As for an infinite wall (subscript ∞), the normal pressure is given by the expressions

$$p_{\mathrm{N}\infty}(r,H,a) = -\frac{\pi A}{6H^3}\left[1 - f_{\mathrm{N}\infty}(r,H,a)\right] \tag{122}$$

where

$$f_{\mathrm{N}\infty}(r,H,a) = \frac{3}{16\pi}\int\limits_0^{2\pi} F_2(x_2)\,\mathrm{d}\varphi \quad (r \leqslant a) \tag{123}$$

$$f_{\mathrm{N}\infty}(r,H,a) = 1 + \frac{3}{16\pi}\int\limits_0^{2\pi}[F_2(x_2) - F_2(x_1)]\mathrm{d}\varphi \quad (r > a) \tag{124}$$

$$F_2(x) \equiv \frac{2}{(x^2+1)^2} - \frac{1}{x^2(x^2+1)} + \frac{\pi}{2x^3} - \frac{1}{x^3}\arctan\frac{1}{x} \tag{125}$$

In Eqns (119) and (123), the factor in front of the square bracket corresponds to the normal pressure in a plane-parallel slit between two infinite surfaces. Therefore, the second term in the brackets is a correction for the finiteness of one of the interacting surfaces. Indeed, $F_1(x) \to 0$ and $F_2(x) \to 0$ as $x \to \infty$. In the other limiting case of an infinite

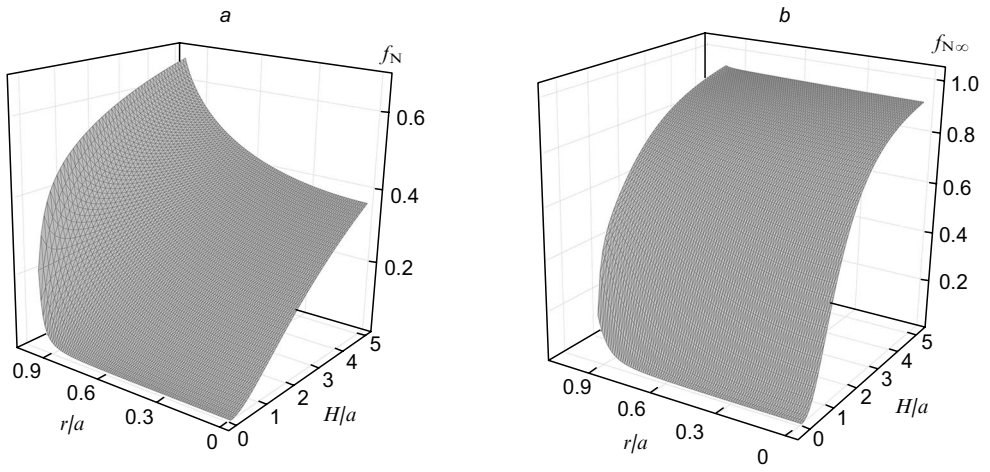


Figure 11. Corrections to p_N on the cylinder end face (*a*) and the infinite wall (*b*).[72]

growth of the slit width H for a finite cylinder radius, $F_1(x) \to 8/3$ at $x \to 0$. In this case, the correction term itself in Eqn (119) tends to unity, and, therefore, the normal pressure in the slit vanishes. In this case, the pressure on the infinite wall also becomes zero, since $F_2(x)/H^3 \to 0$ as $H \to \infty$.

Figure 11 shows the correction terms to the local normal pressure on the cylinder end face (Fig. 11 *a*) and on the infinite surface (Fig. 11 *b*) as functions of r/a and H/a for a fixed value of the cylinder radius a. It can be seen that the functions are characterized by close values in narrow slits ($H/a \ll 1$). Moreover, the values are small, especially near the cylinder axis. This means that nanoscale effects are negligible in this case. With an increase in the slit width, the correction on an infinite surface grows much faster compared with the corresponding correction on the opposite cylinder end surface. Consequently, the local pressure on the cylinder end face is more sensitive to dimensional restrictions than the pressure at the opposite surface.

5.1.1.3. Tangential components of the pressure tensor

Along with the normal component, we calculated the edge effects for other components of the pressure tensor in an empty circular slit.[74] Omitting the details of calculation, we present the final expression for the tangential component p_{rr} with the correction $f_{rr}(r, H, a)$ in the form

$$p_{rr}(r, H, a) \equiv -\frac{\pi A}{24H^3}[1 - f_{rr}(r, H, a)] \tag{126}$$

A similar formula can be written for the second tangential component, $p_{\varphi\varphi}$ with a correction $f_{\varphi\varphi}(r, H, a)$. It should be noted that the difference between the two tangential components becomes visible only near the cylinder edge.

Figure 12 shows the correction $f_{rr}(r, H, a)$ at the cylinder end face (as f_T, Fig. 12 *a*) and at the infinite surface (as $f_{T\infty}$, Fig. 12 *b*) as functions of r/a and H/a. Qualitatively, the results for the tangential component on the two walls of the asymmetric slit are close to those obtained above for the normal component. Edge effects for surfaces are relatively weak far from the boundary in fairly narrow slits: $r < 0.4a$ and $H < 0.5a$. Near the symmetry axis ($r \ll a$), the correction term in all cases rather weakly depends on the distance to the axis. Therefore, for $r < 0.4a$, one can use estimates of the edge effects for $r = 0$. In wider slits, the contribution of the correction term becomes significant even far from the

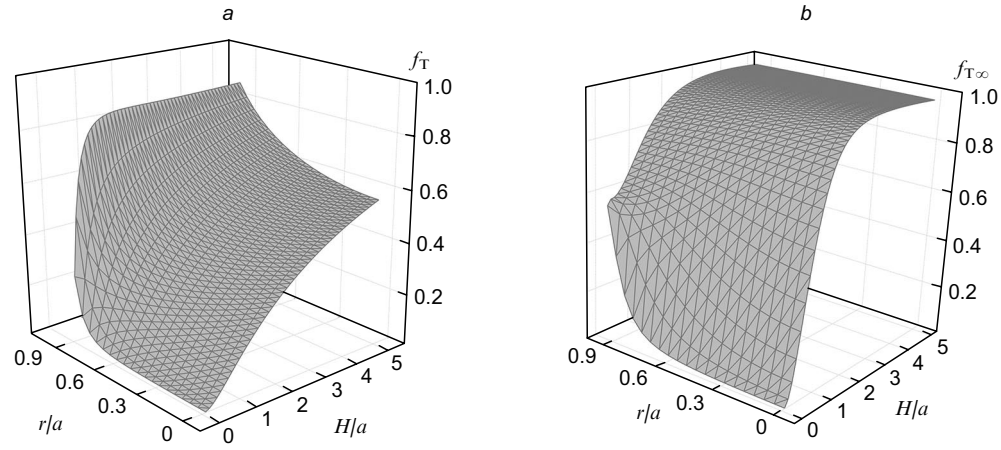


Figure 12. Surface finite size corrections for the tangential pressure p_{rr} with $r < a$ on the cylinder end face (*a*) and on the infinite surface (*b*).[74]

slit edge. Only in very narrow slits, corrections to the tangential pressure can be neglected near the slit axis at $r < 0.5a$.

Similarly to the above-discussed normal component, the local dependence of the tangential components of the pressure tensor in the asymmetric slit is different for the two sides of the slit.[74] Namely, edge effects are more pronounced on the endless wall. This rather physically predictable result for the local pressure components is associated with a difference in the wall areas since the integral values of the pressure components (*i.e.* the components of the total force of interaction) must be the same for both walls.

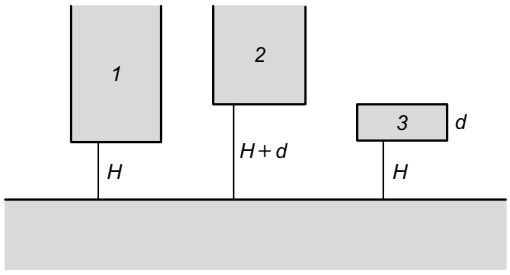


Figure 13. The scheme for finding the pressure tensor in the slit between a cylinder of thickness d and an infinite surface (case *1* − case *2* = case *3*).[75]

5.1.2. Cylinder of a finite length

Not changing the system configuration, the problem is complicated only by adding one more parameter, the cylinder length d. The system simultaneously includes a rod-shaped nanoparticle ($a \ll d$) oriented perpendicularly to the infinite surface and a disk-shaped nanoparticle ($a \gg d$) oriented parallel to the infinite surface as particular cases. To study the interaction between a nanoparticle and a macroscopic body with an infinite surface, we have to calculate the pressure tensor in the slit between them.[75] However, it is unnecessary to repeat the above computational scheme because the results we need are already contained in the above formulas. Indeed, if we solve the problem with a semi-infinite cylinder subsequently for the slit width H and $H+d$, the difference of the solutions will just yield the solution for a finite cylinder of length d (Fig. 13). By doing this, we immediately get the pressure tensor between a finite cylinder and an infinite surface.

We present the result for the normal component of the pressure tensor at the cylinder end face:

$$p_{\mathrm{N}}(H,r,a,d) = -\frac{\pi A}{6H^3}\left\{1 - \frac{H^3}{(H+d)^3} - \right. \tag{127}$$
$$\left. - \frac{3}{16\pi}\int_0^{2\pi} \mathrm{d}\varphi \left[F_1\left(\frac{\rho_a}{H}\right) + \frac{H^3}{(H+d)^3} F_1\left(\frac{\rho_a}{H+d}\right)\right]\right\}$$

where function is defined by Eqn (121). All corrections on the right-hand side of Eqn (127) are positive. This means that the normal pressure in the slit between the nanocylinder and a macroscopic solid body is in absolute value less than for the case of an infinite slit or a finite slit between a semi-infinite cylinder and an infinite flat surface, Eqn (119). Combining all the amendments, Eqn (127) can be rewritten as

$$p_{\mathrm{N}}(H,r,a,d) = -\frac{\pi A}{6H^3}\left[1 - f_{\mathrm{Nd}}(H,r,a,d)\right] \tag{128}$$

where

$$f_{\mathrm{Nd}}(H,r,a,d) \equiv \frac{H^3}{(H+d)^3} + \tag{129}$$
$$+ \frac{3}{16\pi}\int_0^{2\pi} \mathrm{d}\varphi \left[F_1\left(\frac{\rho_2}{H}\right) - \frac{H^3}{(H+d)^3} F_1\left(\frac{\rho_2}{H+d}\right)\right]$$

Function f_{Nd} for several values of the cylinder length is shown in Fig. 14. For a rod-shaped nanoparticle with $d = 5a$, the function is almost the same as in Fig. 11 *a*. This means that cylinders with $d/a > 5$ can be considered infinite when evaluating their interaction with a solid. Figures 14 *b* and 14 *c* show that with a decrease in the cylinder length and turning it into a disk, the correction term increases rapidly. Therefore, the force of interaction of a nanoparticle with the solid surface decreases. In this case, it noticeably reduces the slit width region where the correction for nano-effects can be neglected. For a fixed value of the slit width, the dependence of the local correction f_{Nd} on

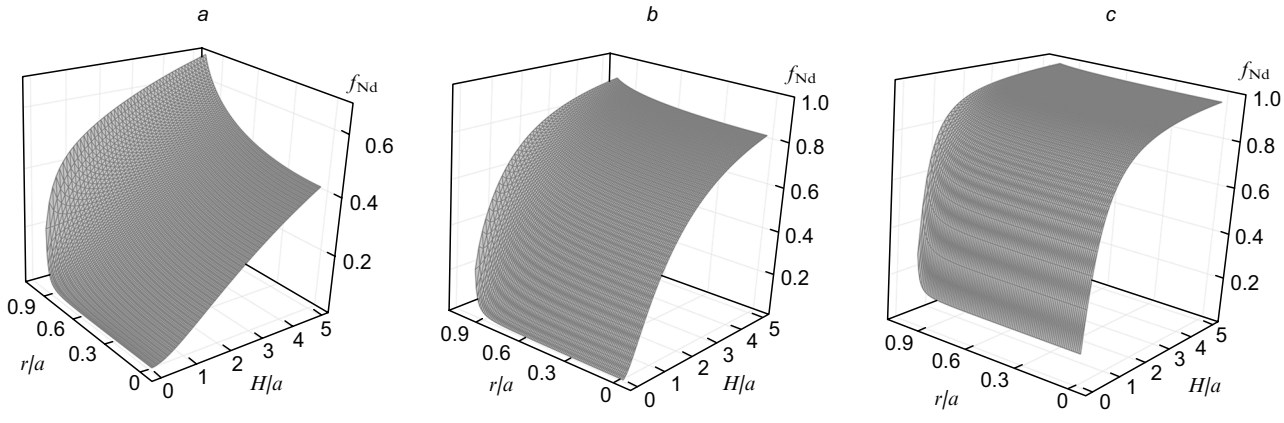


Figure 14. Correction f_{Nd} as a function of r/a and H/a at a fixed d for rod-shaped and disk-shaped nanoparticles: $d = 5a$ (*a*), $d = 0.5a$ (*b*), $d = 0.1a$ (*c*).[75]

the distance to the cylinder axis decreases with diminishing d. When $d = 0.1a$, it becomes almost constant and only slightly increases when approaching the very edge of the disk.

Function $f_{Nd}(H,r,a,d)$ describes the total contribution to the normal pressure from both the finite section of the cylinder and its finite length. Obviously, the latter will be especially noticeable in the case of disks. To estimate it, we consider separately the correction from the finite length of the cylinder and, introducing the notation Δ_d for it, we write it in the form

$$\Delta_d(H,r,a,d) \equiv \frac{H^3}{(H+d)^3}\left[1+\frac{3}{16\pi}\int_0^{2\pi} d\varphi F_1\left(\frac{\rho_2}{H+d}\right)\right] \quad (130)$$

Function $\Delta_d(H,r,a,d)$ is shown in Fig. 15 for two values of d. When approaching the disk edge, this local correction (related to the finite disk thickness) weakens somewhat in contrast to the behaviour of the local correction related to the finite slit length. For a disk of thickness $0.5a$, the maximum contribution of Δ_d is about 45% in the middle of the slit and decrease to 20% near its edge. The dependence of Δ_d on the slit width is more complex. For a thin disk with a thickness of less than half its radius, the additive Δ_d grows rather rapidly with an increase in the width of the slit and reaches its maximum at $H \approx 2a$. Then Δ_d decreases somewhat, remaining finite. With an increase in the thickness of the disk, the maximum in the Δ_d *vs.* H plot disappears. Obviously, when a disk is turned into a cylinder ($d > 2a$), the value of Δ_d becomes negligible.

5.1.3. Disjoining pressure

In an empty flat-parallel slit, the normal pressure on the wall is just a local disjoining pressure. Since the local normal pressures on opposite walls do not coincide in the asymmetric slit under consideration, the question arises which of them can be defined as a disjoining pressure. The question is solved definitely in a situation when the slit narrows by the movement of only one of the walls. Typically, this is the wall of a nanoparticle, as it is more mobile. Then the normal pressure on this wall is the disjoining pressure Π to be dependent not only on the slit width H, but also on the cylinder radius a and the distance r from the axis in the case of an semi-infinite cylinder:

$$\Pi(r,H,a) \equiv p_N(r,H,a) = -\frac{\pi A}{6H^3}[1-f_N(r,H,a)] \quad (131)$$

Where Eqn (119) has been used and is defined by Eqn (120).

Function $f_N(r,H,a)$ describes the influence of the cross-section dimensions of the cylinder on the disjoining pressure. Since this function is positive, the disjoining pressure is obvious to be smaller than for an infinitely extended slit of the same width. Obviously, for finite disks, a dependence on the disk thickness appears in disjoining pressure to be described now by Eqn (127). Finally, if we average the correction over the slit area, we get an estimate of the average deviation $\Delta\Pi$ of the disjoining pressure from its value Π for an infinite slit. Introducing a dimensionless quantity $\Delta\Pi/\Pi$, Fig. 16 shows how it depends on H/a.

The local correction to the disjoining pressure increases with the slit width, although, naturally, the disjoining pressure itself decreases herewith. For a cylinder of a finite length ($d = 5a$), the correction is larger than for an infinite

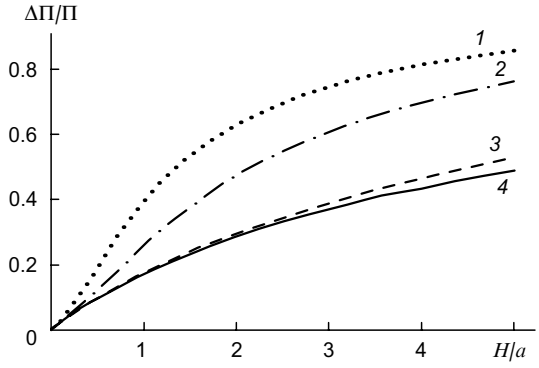


Figure 16. Relative correction to the average disjoining pressure of a slit as a function of H/a.[75]
$d = 0.5a$ (1), a (*b*), $5a$ (*3*), ∞ (*4*).

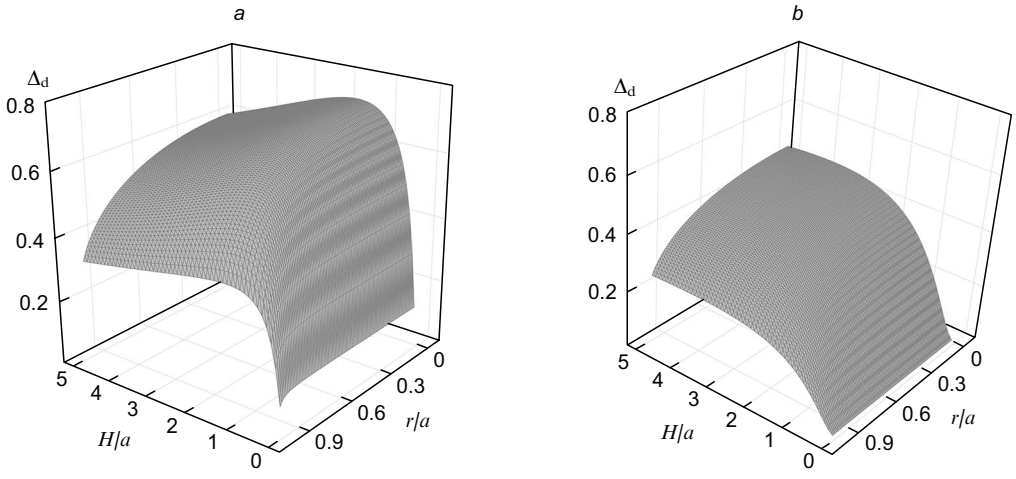


Figure 15. Correction Δ_d defined by Eqn (130) as a function of r/a and H/a for a disk-shaped nanoparticle at $d = 0.1a$ (*a*) and $d = 0.5a$ (*b*).[75]

cylinder and it becomes especially noticeable for disks. It can be seen, however, that even at $d = 5a$, the difference from the correction for an infinite disk becomes insignificant. In the case of disks, the deviation of the disjoining pressure from its value for the infinite slit is the greater, the thinner the disk.

It should be clarified here that the discussed nanoscale effects on the disjoining pressure are derived from the average value of the local normal pressure at the cylinder end face. This value differs from that obtained on the basis of Hamaker's classical non-local approach, which will be discussed below in connection with the influence of the shape of nanoparticles on their interaction with a solid (Section 5.3). In Hamaker's approach for the asymmetric slits in question, the normal pressure in a finite slit coincides with the pressure in an infinite slit. Therefore, it is impossible to estimate the effect of longitudinal slit size within Hamaker's approach.

As is seen from Fig. 17, Hamaker's method yields a larger value for the attraction force. This arises from the fact that Hamaker's approach takes into account all pairwise interactions including not only the end face, but also the lateral cylinder surface. Therefore, the larger the axial size of the cylinder, the greater should be the difference in the two above calculation methods. This is also well seen from Fig. 16.

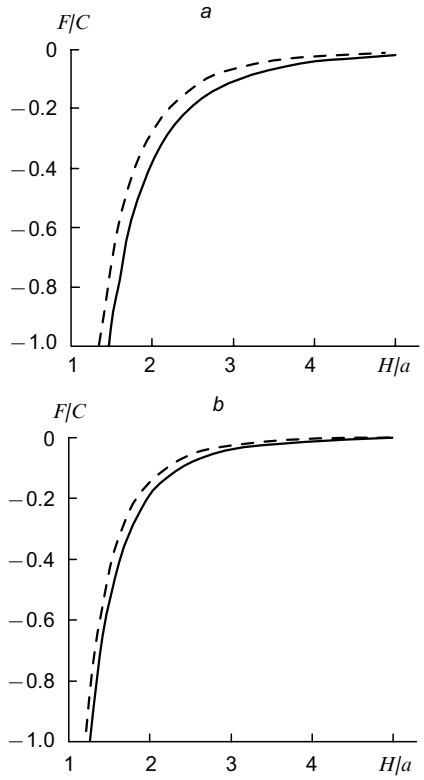


Figure 17. Comparison of the forces of interaction of a cylinder with an infinite solid surface, calculated following Hamaker, through the interaction potential (the solid line) and through the normal component of the pressure tensor (the dashed line), as functions of H/a for a rod-shaped particle with $d = 5a$ (*a*) and a disk-shaped particle with $d = 0.5a$ (*b*), the force F being measured in the units of Hamaker's constant $C = \pi A/6$.[75]

5.2 Symmetrical slit with finite surfaces

We now turn to the interaction of two identical bodies. In the case of flat-parallel faces of the bodies, symmetry is restored with respect to the longitudinal middle plane in the system. As a consequence, the behaviour of the local components of the pressure tensor will be the same on both slit surfaces. Such a slit will be called symmetric. We start with considering the interaction between two semi-infinite coaxial cylinders with the parallel end faces of nanoscaled dimensions.[76]

5.2.1. Slit between two semi-infinite cylinders

The case under consideration is illustrated by Fig. 18. Comparing with the case studied in Section 5.1 (see Fig. 9), we have the only change in the volume and shape of body *2*. The latter is now the same semi-infinite cylinder of radius a as body *1*. Since the slit walls are identical, the components of the local pressure tensor will be the same on both walls.

When considering the pressure tensor, we will follow the same computational scheme as in the previous section with the same choice of coordinates. Equations (112)–(115) for the components of the pressure tensor remain also valid for the case under consideration.As for the asymmetric slit, we first calculate the normal component of the pressure tensor.[76]

5.2.1.1. Pressure tensor in an empty slit

After integrating over z_2 and z_1 and partially integrating over ρ, the expression for the normal component of the pressure tensor can be represented as follows:

$$p_N(r, H, a) = -\frac{\pi A}{6H^3}[1 - f_N(H, r, a)] \tag{132}$$

where

$$f_N(r, H, a) = \frac{3H^3}{16\pi}\int_0^{2\pi} d\varphi F_1(\rho_1) + \tag{133}$$

$$+\frac{9H^3}{\pi}\int_0^{2\pi} d\varphi \int_0^{\rho_1(\varphi)} d\rho F_2(\rho)\frac{\rho^5}{(\rho^2+\rho_2^2)^4}$$

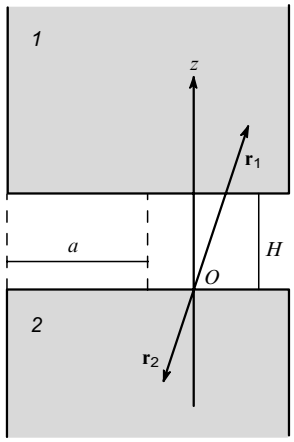


Figure 18. A slit between two solid cylinders: a is the cylinder radius, H is the slit width, and vectors $\mathbf{r}_1$ and $\mathbf{r}_2$ denote the positions of interacting molecules with respect to the point of calculation taken for the coordinate origin.[76]

$$F_1(\rho) \equiv \frac{2H}{(\rho^2+H^2)^2} - \frac{H}{\rho^2(\rho^2+H^2)} + \frac{\pi}{2\rho^3} - \frac{1}{\rho^3}\arctan\frac{H}{\rho} \quad (134)$$

$$F_2(\rho) \equiv \frac{H}{6(H^2+\rho^2)^3} - \frac{H}{24\rho^2(H^2+\rho^2)^2} - \quad (135)$$
$$- \frac{H}{16\rho^4(H^2+\rho^2)} + \frac{\pi}{32\rho^5} - \frac{1}{16\rho^5}\arctan\frac{H}{\rho}$$

The limiting values ρ_1 and ρ_2 of the variable ρ are determined by the formulas

$$\rho_1 = -r\cos\varphi + \sqrt{a^2 - r^2\sin^2\varphi} \quad (136)$$

$$\rho_2 = r\cos\varphi + \sqrt{a^2 - r^2\sin^2\varphi} \quad (136a)$$

and are shown in Fig. 19.

The integration over ρ in Eqn (133) can be performed analytically to yield an extremely cumbersome result. Since the subsequent integration over the polar angle is analytically impossible, it is reasonable to transform the integrand expression in such a way as to separate the main asymptotic terms as the usual expression for an infinitely long slit, and combine the rest terms as a function $f_N(H,r,a)$ for numerical integration. The function $f_N(H,r,a)$ characterizes the edge correction. This function is shown in Fig. 20 *a* for a fixed value of radius a.

Comparing $f_N(H,r,a)$ with similar functions for an asymmetric slit (see Fig. 11), it can be seen that the dimensional corrections to the local normal pressure on the symmetric slit walls are larger than on the cylinder end face in an asymmetrical slit. This is an obvious consequence of the fact that two identical nanoparticles interact with each other more weakly than a similar particle with a larger one.

Along with the normal component, we estimated edge effects for other components of the pressure tensor in an empty circular slit.[74] As in the case of an asymmetric slit, we represent the final expression for the tangential pressure p_T with a correction in the form

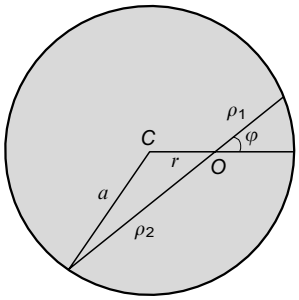


Figure 19. To calculating the normal pressure on the cylinder end face as the slit wall: C is the central point of the cylinder face, O is the origin of cylindrical coordinates at the point of calculation, a is the cylinder radius, r is the distance between the point of calculation and the central point, and ρ_1 and ρ_2 are the limiting values for coordinate ρ at a given φ [Eqns (136) and (136a)].[76]

$$p_T(r,H,a) \equiv -\frac{\pi A}{24H^3}[1 - f_T(r,H,a)] \quad (137)$$

where subscript T refers both to rr and $\varphi\varphi$ components. The behaviour of both components is very similar, and a noticeable difference appears only near the edge of the slit.

Fig. 20 *b* shows the function $f_T \equiv f_{rr}$, which can be compared with the correction to the normal pressure in Fig. 20 *a*. It can be seen from the Figure that the edge effects for both components of the pressure tensor are relatively weak far from the boundary in fairly narrow slits with $r < 0.6a$ and $H < 0.5a$. Near the axis, the correction term in all cases depends rather weakly on the distance to the axis. Therefore, as in an asymmetric slit, one can use estimates of edge effects on the disk axis ($r = 0$) for $r < 0.4a$. In wider slits, the contribution of the correction term becomes significant even far from the slit edge. From a comparison of Fig. 20 *a* and Fig. 20 *b*, it can be seen that, on average, the influence of edge effects in the symmetric gap on the tangential pressure is noticeably stronger compared to the normal pressure. Only in very narrow slits, corrections to the tangential pressure can be neglected near the slit axis at $r < 0.5a$. In slits wider than $2a$, the correction term compensates for up to 95% of the tangential pressure. Con-

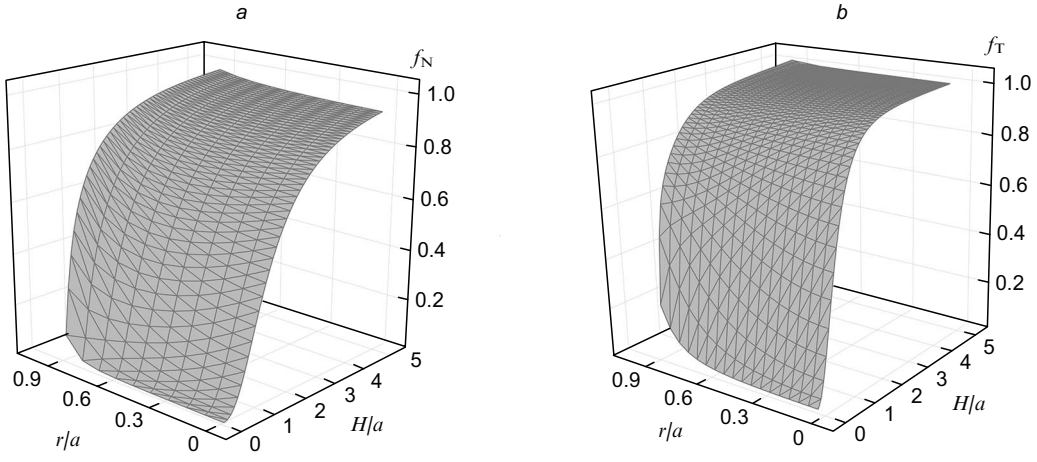


Figure 20. The 3d-presentation of functions $f_N(H,r,a)$ (*a*) and $f_T(H,r,a)$ (*b*).[74]

sequently, the tangential pressure in a finite slit becomes substantially smaller in absolute value than in an infinite slit. Although this conclusion was obtained for an empty slit, it can be assumed to remain valid for a slit filled with fluid. Then we should expect a decrease in the tension of a finite film compared to an infinite analogue. If we compare the behaviour of the tangential pressure components in symmetrical and asymmetrical slits, we see that the correction on the infinite wall is more similar in behaviour to the analogous quantity of a symmetrical slit. If we compare the behaviour of the tangential and normal components, the former are more sensitive to the presence of the slit boundary.

Concluding consideration of the local components of the pressure tensor, we briefly discuss the off-diagonal component, which we write for a point on the wall of a symmetric slit after integration over z_2 and z_1 as

$$p_{rz}(r,H,a) = -\frac{A}{8}\int_0^{2\pi}\cos\varphi\,\mathrm{d}\varphi\int_0^{\rho_1}\frac{\rho^2}{(\rho^2+H^2)^3}\left[1-\frac{\rho^4}{(\rho+\rho_2)^4}\right]\mathrm{d}\rho \tag{138}$$

The rest of the integration over ρ and φ is carried out numerically. The result for a symmetric slit in the interval $H > 0.4a$ is shown in Fig. 21. It can be seen that this component is a small positive value, which varies non-monotonically as it approaches the slit edge. It acquires the greatest values in narrow slits with $H < 0.5a$. The non-monotonic behaviour of p_{rz} is simply explained. By virtue of the symmetry of the slit, p_{rz} vanishes at $r = 0$, and due to the limited size of the slit in vacuum, it also vanishes at the boundary of the slit together with other components of the pressure tensor. As noted above when discussing other components, a region is observed near the slit axis, where the pressure tensor weakly depends on the distance to the axis. Therefore, the maximum of the off-diagonal component is located closer to the edge of the slit.

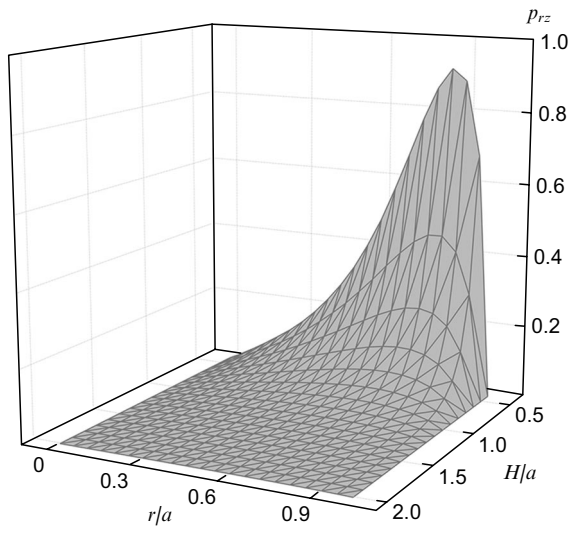


Figure 21. Off-diagonal component $p_{rz} = p_{zr}$ in a symmetric slit expressed in the A units.[74]

5.2.1.2. Slit filled with a fluid

So far, we dealt with an empty circular slit between interacting bodies. If a fluid appears in the slit, the distribution functions of the fluid components will affect the interaction of the bodies.[77,78] The consideration of such effect is the goal of this section. The configuration of the system is maintained (see Fig. 18). We only introduce, in addition, the phase designations (α for a fluid and β for the solid phase of both cylinders) and the calculation point location inside the slit with distances h and s ($h+s=H$) from the slit walls (Fig. 22). In such system, the fluid distribution functions will depend not only on h and s, but also on the distance r from the cylinder axis and on the cylinder radius a.[77]

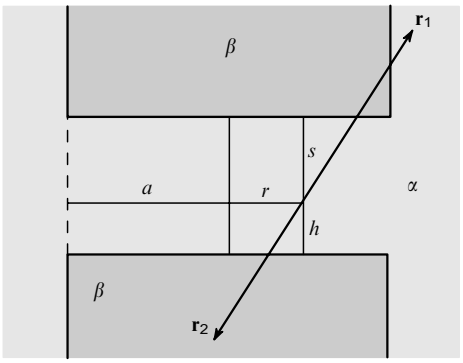


Figure 22. Slit between the cylinder (phase β) end faces filled with a fluid (phase α).[77]

Using the distribution functions and Eqn (1) for not retarded dispersion forces, the local pressure tensor inside the slit can be calculated on the basis of Eqn (10) as a whole.[78] When considering the spatial dependence of the components of the pressure tensor, it is necessary to use the condition of finding points on the straight line segment connecting points $\mathbf{r}_1$ and $\mathbf{r}_2$ (see Fig. 22). This leads to the dependence of the limits of integration on the position of the point in question. So, the interval for the variation of z_2 will be

$$-z_1\frac{\rho}{\rho_2} \leqslant z_2 \leqslant -h \tag{139}$$

The limits of changing the coordinates of point $\mathbf{r}_1$ will depend on r. When $r \leqslant a|H-2h|/H$, we have $H-h \leqslant z_1 \leqslant \infty$, $0 \leqslant \rho \leqslant \rho_1$, $0 \leqslant \varphi \leqslant 2\pi$. When $r > a|H-2h|/H$, the ranges of variation of polar radius ρ and polar angle φ will depend on a parameter $\tilde{\rho} \equiv \rho_2 z_1/h$. When $\rho_1 < \tilde{\rho}$, we have the ranges $0 \leqslant \rho \leqslant \rho_1$, $-\tilde{\varphi} \leqslant \varphi \leqslant \tilde{\varphi}$, and $\tilde{\varphi}$ is the solution of Eqn (140).

$$\left(\frac{z_1}{h}+1\right)r\cos\tilde{\varphi} + \left(\frac{z_1}{h}-1\right)\sqrt{a^2-r^2\sin^2\tilde{\varphi}} = 0 \tag{140}$$

At $\rho_1 > \tilde{\rho}$, we have $0 \leqslant \rho \leqslant \tilde{\rho}$, $\tilde{\varphi} \leqslant \varphi \leqslant \pi + \tilde{\varphi}$.

The above requirements greatly complicate the integration over $\mathbf{r}_1$. Not to deal with a number of cumbersome resulting expressions, we confine ourselves by presenting the normal component of the pressure tensor as

$$p_{\mathrm{N}}(r,h,H,a) = p^{\alpha} - \sum_{s,t} A_{st}\rho_t^{\alpha}(\rho_s^{\beta} - \rho_s^{\alpha})F_{\alpha}(r,h,H,a) - \qquad (141)$$
$$-\frac{\pi}{6H^3}\sum_{s,t} A_{st}(\rho_s^{\beta} - \rho_s^{\alpha})(\rho_t^{\beta} - \rho_t^{\alpha})[1 - F_{\mathrm{N}}(r,h,H,a)]$$

where only functions $F_{\alpha}(r,h,H,a)$ and $F_{\mathrm{N}}(r,h,H,a)$ need specification. For given H and a, function $F_{\alpha}(r,h,H,a)$ depends on h and r and is represented as the sum of two contributions from h and $H-h$ in the form

$$F_{\alpha}(h,r) \equiv \frac{3}{32}[F_1(h,r) + F_1(H-h,r)] \qquad (142)$$

where

$$F_1(h,r) = \frac{1}{64}\int_0^{2\pi}\frac{\mathrm{d}\varphi}{\rho_1^3}\left[\frac{\pi}{2} - \frac{2h\rho_1^3}{3(h^2+\rho_1^2)^2} - \frac{3h\rho}{8(h^2+\rho_1^2)} - \arctan\left(\frac{h}{\rho_1}\right)\right] \qquad (143)$$

a similar expression for $F_1(H-h,r)$ being written with the replacement of h by $H-h$ in Eqn (143).

Function $F_{\mathrm{N}}(r,h,H,a)$ describes the contribution from the fluid phase to the pressure tensor and is written at constant H and a as

$$F_{\mathrm{N}}(h,r) \equiv \frac{6H^3}{\pi}[I_1(h,r)\Theta(x) + (I_2(h,r) + I_3(h,r))\Theta(-x)] +$$
$$+\frac{6H^3}{\pi}[I_1(H-h,r)\Theta(x) + [I_2(H-h,r) + I_3(H-h,r)]\Theta(-x)] \qquad (144)$$

where $x \equiv |H-2h|/H - r/a$ and $\Theta(x)$ is the Heaviside step function,

$$I_1(h,r) \equiv \frac{1}{2}\int_0^{\pi}\mathrm{d}\varphi\int_s^{\infty}\frac{z_1^6\mathrm{d}z_1}{(z_1+h)^4(\rho_1^2+z_1^2)^3} - \qquad (145)$$
$$-3\int_0^{\pi}\mathrm{d}\varphi\int_0^{\rho_1}\frac{\rho^5\mathrm{d}\rho}{(\rho+\rho_2)^4}\int_s^{\infty}\frac{z_1^2\mathrm{d}z_1}{(\rho^2+z_1^2)^4}$$

$$I_2(h,r) \equiv -\frac{1}{2}\int_s^{\infty}\frac{z_1^6\mathrm{d}z_1}{(z_1+h)^4}\int_0^{\tilde{\varphi}}\frac{\mathrm{d}\varphi}{(\rho_1^2+z_1^2)^3} - \qquad (146)$$
$$-3\int_s^{\infty}z_1^2\mathrm{d}z_1\int_0^{\rho_1}\frac{\rho^5\mathrm{d}\rho}{(\rho^2+z_1^2)^4}\int_0^{\tilde{\varphi}}\frac{\mathrm{d}\varphi}{(\rho+\rho_2)^4}$$

$$I_3(h,r) \equiv -\frac{1}{2}\int_s^{\infty}\frac{z_1^6\mathrm{d}dz_1}{(z_1+h)^4}\int_{\tilde{\varphi}}^{\pi}\frac{\mathrm{d}\varphi}{(\tilde{\rho}^2+z_1^2)^3} - \qquad (147)$$
$$-3\int_s^{\infty}z_1^2\mathrm{d}z_1\int_{\tilde{\varphi}}^{\pi}\mathrm{d}\varphi\int_0^{\tilde{\rho}}\frac{\rho^5\mathrm{d}\rho}{(\rho+\rho_2)^4(\rho^2+z_1^2)^4}$$

On the right-hand side of Eqn (141), the second term is the contribution to the normal pressure in the finite slit from the molecules of a fluid phase α located outside the slit. Naturally, this term is absent in the case of an infinite slit. Function $F_{\alpha}(h,r)$ is the sum of the contributions from both walls. In Fig. 23, this function is shown for a slit of width $H = a$. It can be seen that the function is significantly different from zero only near the slit edge at $r > 0.8a$ and in a very narrow region near the walls ($h < 0.2a$), where $F_{\alpha}(h,r)$ can reach high values. Due to its additivity and the rapid decline when moving away from the walls, function $F_{\alpha}(h,r)$ is significantly dependent on the slit width only in the region of very narrow slits. For the same reason, the limiting values of this function weakly depend on the width of the slit.

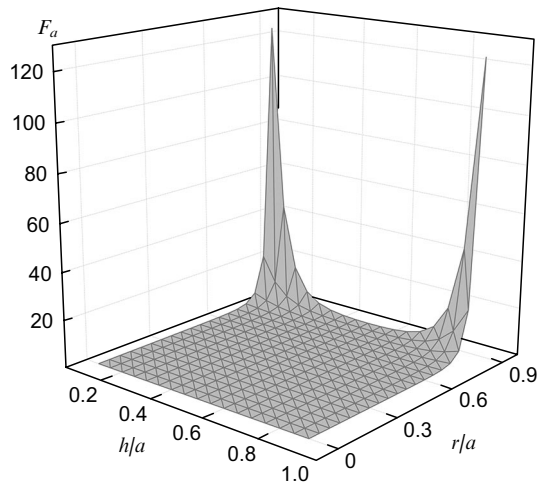


Figure 23. Function $F_{\alpha}(h,r)$ for a slit of width $H = a$.[77]

The third term in Eqn (141) describes the contribution to the normal pressure in a fluid film from the interaction of the solids. The multiplier in front of the square bracket corresponds to the case of an infinite slit and describes the disjoining pressure in the slit.[43] Function $F_{\mathrm{N}}(h,r,H,a)$ determines the addition to the normal pressure due to the finite slit size. For two slits, this function is presented in Fig. 24.

$F_{\mathrm{N}}(h,r)$ is a positively definite function. Unlike the multiplier in front of the square bracket in Eqn (141), $F_{\mathrm{N}}(h,r)$ depends on the position in the slit, being thus a local quantity. At the very edge of the slit at $r = a$, $F_{\mathrm{N}}(h,r)$ becomes equal to unity and the contribution from the square brackets in Eqn (141) disappears. Then the pressure behaviour in the slit is determined only by the second term in Eqn (141). As expected, function $F_{\mathrm{N}}(h,r)$ is symmetrical with respect to the middle plane of the slit. $F_{\mathrm{N}}(h,r)$ acquires the greatest values on the slit walls. This means that there is an extreme of $F_{\mathrm{N}}(h,r)$ in the middle of the slit. It turns out that the nature of this extreme changes as it moves from the axis to the edge of the slit (see Fig. 24). In the near-axial region, this function takes the minimum value in the middle of the slit. When moving to the edge of the slit, the minimum disappears, giving way to a flat maximum. Obviously, the larger the $F_{\mathrm{N}}(h,r)$ value, the stronger the influence of the finite slit size on the pressure in the slit. It can be seen that the role of $F_{\mathrm{N}}(h,r)$ increases with the slit width, with the interval of its values decreasing. At $H = a$, the contribution from the finite slit size exceeds 70% already. Naturally, at $h = 0$ or $h = H$, the values of $F_{\mathrm{N}}(h,r)$ coincide with the previously obtained values of a correction to the normal pressure on the wall of an empty symmetrical slit (Section 5.2.1.2). Obviously, for local pressure throughout the empty slit we would get the same function $F_{\mathrm{N}}(h,r)$. Consequently, for this term in the formula for local pressure, the difference in behaviour in the empty and fluid-filled slits reduces only to replacing ρ_s^{β} by $\rho_s^{\beta} - \rho_s^{\alpha}$ in accordance with the asymptotic principle of interaction of

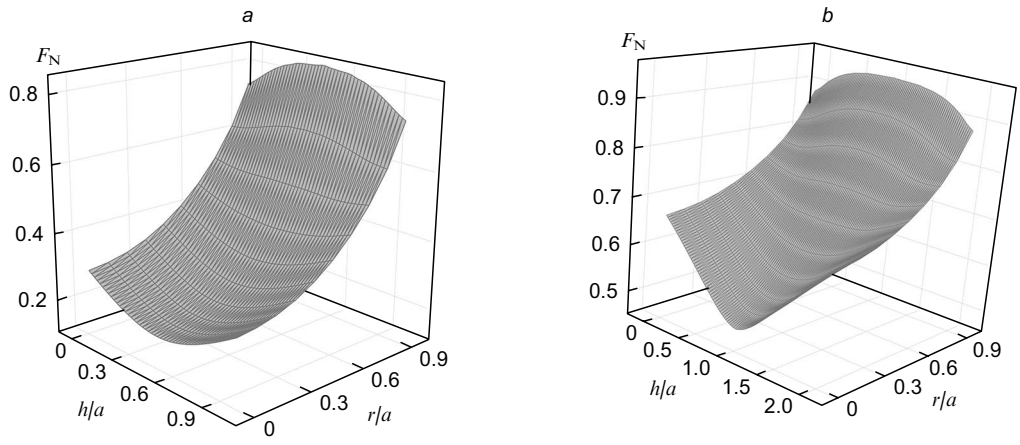


Figure 24. Function $F_N(h, r)$ for slits with widths $H = a$ (*a*) and $H = 2a$ (*b*).[78]

bodies in a fluid medium (Section 2). This should lead to weakening with the attraction of solids in a fluid compared to the empty slit. However, the second local term in Eqn (141), which is present only in the case of bodies immersed in a fluid, will enhance the mutual attraction of the bodies. In conclusion, worth mentioning is the obvious consequence of all the calculations described in this section that all the effects discussed should disappear as the radius of the circular slit tends to infinity.

5.2.2. Empty slit between two finite cylinders

In the previous section, we estimated the effect of nanoscale size of a slit on the behaviour of the pressure tensor in the slit. We now turn to three-dimensional nanoparticles and determine the contribution of their size to the interparticle interaction in terms of the local pressure tensor.[79] The solution of this problem is especially important for colloid science dealing with nanoparticles. Compared with the edge effects of nano-slits discussed above, taking into account the size of nanoparticles themselves will make an additional contribution to the particle interaction. For simplicity, we consider the symmetric case of two coaxial nanocylinders of radius a and lengh d in vacuum at a distance H between the cylinder end faces (Fig. 25). With a sufficiently small length of a cylinder, it turns into disk, and the cylinder length d may also be called the disk thickness. Since we assume the two cylinders to be identical, parameter d is the only additional quantity as compared with the previous case considered, similarly to the case of interaction of a finite cylinder with a macroscopic body with an infinite surface (Section 5.1.2).

The calculation procedure is similar to that described above [see, *e.g.*, Eqn (112)] with the difference that the integration is carried out over limited volumes of V_1 and V_2 of disks *1* and *2* in Fig. 25, respectively. This is reflected in the choice of the limits of integration over z_1 and z_2. In the case of two disks with the integration over z_1, the upper limit is $H + d$. The integral over the V_2 volume of disk *2* requires some transforms. This integral can be represented as the difference of the integrals over volumes V_3 (Fig. 25 *b*) and V_4 (Fig. 25 *c*) of two semi-infinite cylinders. Each of the integrals corresponds to the interaction of disk *1* with semi-infinite cylinders with a separation of H or $H + d$, respectively. Let us consider the normal component of the

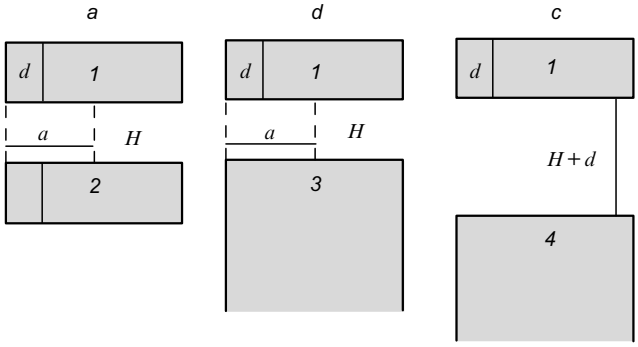


Figure 25. A slit of width H between two disks of radius a and thickness d(*a*); auxiliary drawings for integrating over the volume of disk *2* (*b*, *c*).[79]

pressure tensor on the end face of one of two coaxial interacting cylindrical particles of length d (two disks of thickness d). The calculation on the basis of Eqn (112) yields

$$p_N(r, H, a, d) = -\frac{\pi A}{6H^3}[1 - f_{Nd}(r, H, a, d)] \tag{148}$$

where

$$f_{Nd}(r, H, a, d) = \frac{2H^3}{(H+d)^3} - \frac{H^3}{(H+2d)^3} + \tag{149}$$

$$+\frac{3H^3}{2\pi}\int \mathrm{d}\varphi \int_H^{H+d} \frac{z_1^2 \mathrm{d}z_1}{(\rho_1^2 + z_1^2)^3} - \frac{3H^3}{2\pi}\int_H^{H+d} \frac{\mathrm{d}z_1}{(z_1+d)^4} \times$$

$$\times \left[\int_{(\rho_1 < \tilde{\rho})} \frac{z_1^6 \mathrm{d}\varphi}{(\rho_1^2 + z_1^2)^3} + \int_{(\rho_1 > \tilde{\rho})} \frac{d^6 \mathrm{d}\varphi}{(\rho_2^2 + d^2)^3} \right] +$$

$$+\frac{9H^3}{\pi}\int_H^{H+d} z_1^2 \mathrm{d}z_1 \int_{(\rho_1 > \tilde{\rho})} \mathrm{d}\varphi \int_{\tilde{\rho}}^{\rho_1} \frac{\rho^5 \mathrm{d}\rho}{(\rho^2 + z_1^2)^4 (\rho + \rho_2)^4}$$

$$\tilde{\rho} \equiv \frac{z_1 \rho_2}{d} \tag{149a}$$

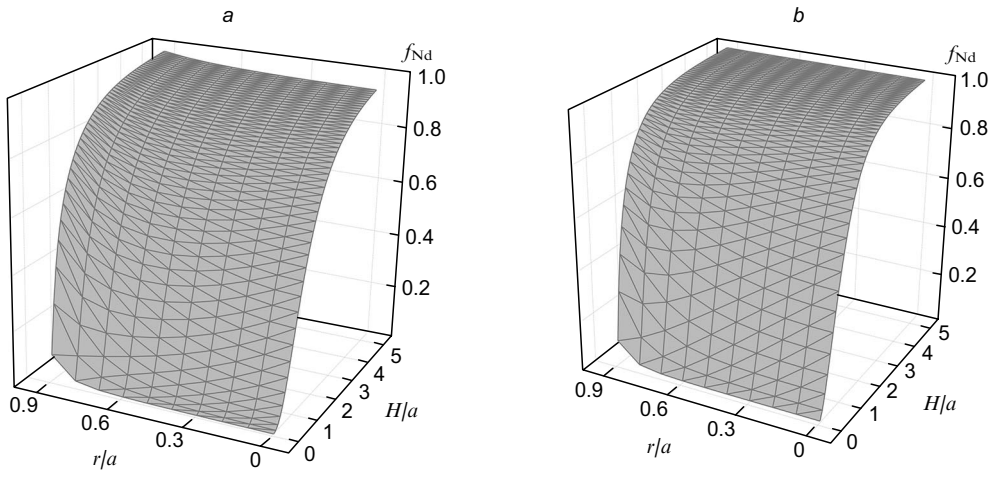


Figure 26. Correction f_{Nd} to the normal pressure on the cylinder end face in a slit between two rod-shaped nanoparticles with $d = 5a$ (*a*) and two disk-shaped nanoparticles with $d = 0.5a$ (*b*).[79]

and ρ_1 and ρ_2 are the limiting values for variable ρ (see Fig. 19).

Function $f_{Nd}(r, H, a, d)$ gives a relative correction to the normal pressure of an infinite slit due to the finite dimensions of both the slit itself and the disks forming the slit. Obviously, the smaller the disk thickness, the greater the normal pressure deviation from its value in the circular slit between semi-infinite cylinders, for which the correction due to the finite radius of the slit is given by Eqn (133). For several values of d, the corrections are shown in Fig. 26. It can be seen that at $d = 5a$ (rod-shaped particles) $f_{Nd}(r, H, a, d)$ is close to the analogous function, Eqn (133), for a slit between semi-infinite cylinders (see Fig. 20), which can be written as $f_N(r, H, a, \infty)$.

To exhibit the effect of the disk thickness separately from the effect of the slit width, we introduce a quantity

$$\Delta f_{Nd}(r, H, a, d) \equiv f_{Nd}(r, H, a, d) - f_N(r, H, a, \infty) \qquad (150)$$

Function Δf_{Nd} characterizes the contribution only from the finite size of the disks themselves.

Figure 27 shows function Δf_{Nd} for two disk thicknesses. The nonmonotonic dependence of these functions on the slit width is manifested in all cases. Obviously, this is explained by the fact that in narrow slits the contribution to the normal pressure from the disk thickness becomes close to the value for a semi-infinite cylinder and the difference between their values decreases with decreasing the slit width. In wide slits, both the contributions themselves and their difference tend to zero with an increase in the slit width. With an increase in the disk thickness, the maximum of Δf_{Nd} becomes wider and shifts from $0.5a$ for $d = 0.1a$ towards larger values of H. However, the absolute values of local deviations of the normal pressure from its value in the slit between semi-infinite cylinders quickly decrease. At $d = 2a$, they do not exceed 3% and practically disappear at $d = 5a$.

5.2.3. Disjoining pressure

We now turn to estimating the disjoining pressure in a symmetrical slit, which, unlike the asymmetric slit, does not depend on the choice of wall for the definition of the

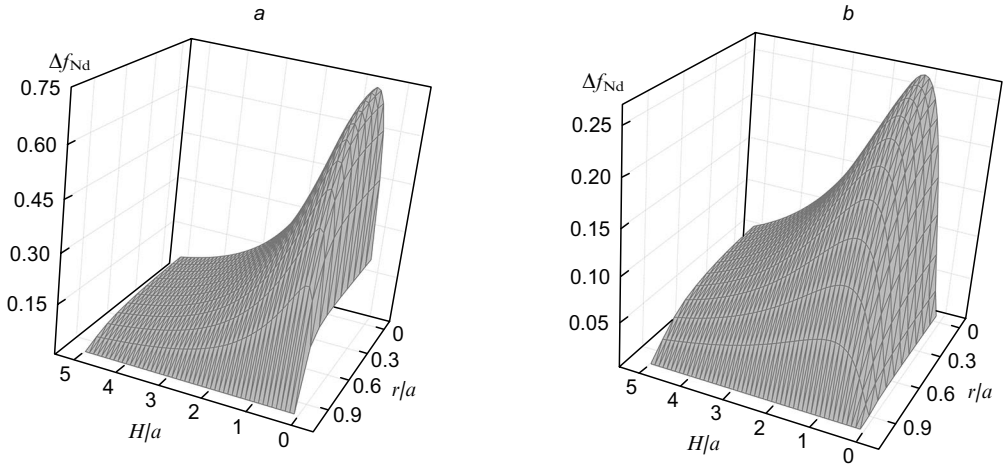


Figure 27. Function Δf_{Nd} for disks with $d = 0.1a$ (*a*) and $d = 0.5a$ (*b*).[79]

disjoining pressure. The local disjoining pressure at the end face of a semi-infinite and finite cylinder is described by Eqns (132) and (148), respectively. The relative contributions to the local disjoining pressure from the finite slit size and the size of particles themselves are described by functions f_N, Eqn (133), and f_{Nd}, Eqn (149), respectively. Comparison with disjoining pressure Π_∞ in an infinite slit is convenient to be carried out for the local disjoining pressure value averaged over the slit area. This average value of the disjoining pressure is denoted as $\Pi(H,a)$ for the case of infinite cylinders and as $\Pi_d(H,a,d)$ for the case of finite cylinders including disks. The relative deviations of the quantities Π and Π_d from Π_∞, $\Delta\Pi/\Pi_\infty$ and $\Delta\Pi_d/\Pi_\infty$, are shown in Fig. 28 *a*. Obviously, they should tend to unity with an unlimited increase in the slit width. The larger these deviations, the lower the disjoining pressure in the slit between two nanoparticles as compared with an infinite slit. In a symmetrical slit, the values of the disjoining pressure deviations are significantly greater than in an asymmetrical one (see Fig. 16).

A similar quantity $\Delta\Pi/\Pi_\infty$ for semi-infinite coaxial cylinders was estimated by Jaiswal and Beaudoin.[80] Their approximate formula [Eqn (23) from Ref. 80] can be written in our notation as

$$\frac{\Delta\Pi}{\Pi_\infty}=\frac{3H^2}{16a^2}+\frac{3}{8}\left(\frac{H}{a}-\frac{H^3}{3a^3}\right)\arctan\frac{2a}{H} \qquad (151)$$

The dependence following from this formula is also shown in Fig. 28 *a*. Equation (151) gives somewhat lower values than our data, although the difference is small. With the slit width of $H = 2a$, the difference becomes about 10%. The largest difference is observed in the interval of the slit width $1.5a < H < 3.5a$.

Especially significant difference is observed for nanoparticles. So, for disks with a thickness of $d = 0.1a$, the disjoining pressure almost disappears, starting with $H = a$. However, with an increase in the size of the interacting particles, their effect on the disjoining pressure quickly decreases. Already at $d = a$, the influence of particle size becomes less than 5% for $H > 3a$. In the case of nanoparticles, the influence of finite dimensions of interacting particles on the disjoining pressure becomes more obvious if we refer to the following characteristic:

$$\Delta_d\Pi(H,a,d)\equiv\frac{\Pi(H,a,d)-\Pi(H,a,\infty)}{\Pi_\infty} \qquad (152)$$

Function $\Delta_d\Pi$ is shown in Fig. 28 *b*. Like the local quantity f_{Nd}, Eqn (149), $\Delta_d\Pi$ is characterized by a maximum when the slit width varies. The origin of the maximum is of the same nature as for f_{Nd}. The maximum height decreases rapidly with increasing the disk thickness and becomes moderate when $d > a$. As mentioned above, within this thickness range the contribution to the relative correction to the normal pressure does not exceed 5%. It is obvious that the main changes in the disjoining pressure due to the finite dimensions of the interacting particles are concentrated in the range of variation of the slit width $H < 3a$.

Summing up the results obtained, we can conclude that the significant influence of the size of any small particles on their interaction cannot be neglected if the particle size does not exceed the interparticle distance. In addition, it is of note that, although our study was conducted for an empty slit, the conclusions remain valid for a slit filled with a fluid since the results were formulated for relative pressure changes in comparison with an infinite slit.

5.3. Shape factors of nanoparticle interaction

When considering a system with many particles, the question arises about the effect of the particle shape on the properties under study. In the literature, this issue has been actively discussed for many years.[4,7,80–91] Although the question of the influence of the particle shape on the particle interaction was studied in a multilateral way, no direct comparison of forces for different particles was undertaken until recently.[92] In order to estimate the effect of the shape, it is necessary to calculate the energy and force of interaction of particles of the same nature and volume, but geometrically different. We consider the problem in this section and restrict ourselves to simplest geometric shapes to obtain analytical solutions for the problem of interaction of particles of various shapes with an infinite solid surface [92] using the example of dispersion forces and Hamaker's approach.[4]

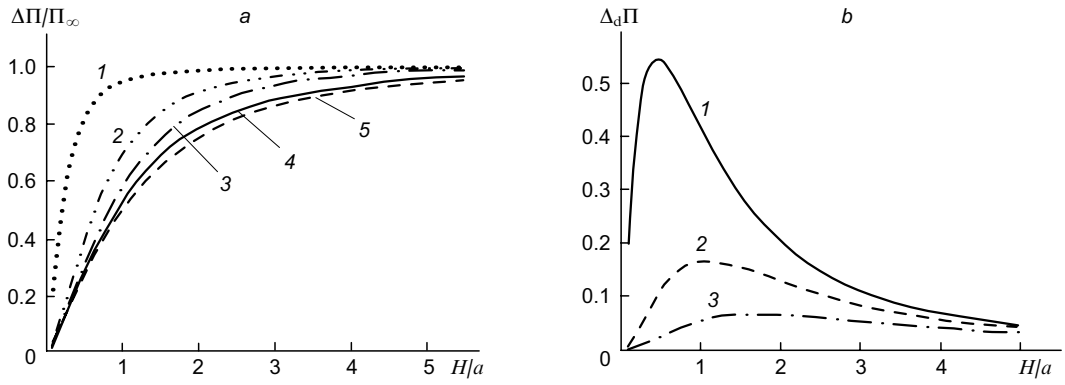


Figure 28. Plots of $\Delta\Pi/\Pi_\infty$ (*a*) and $\Delta_d\Pi$ (*b*) *vs.* H/a for various values of d.[79]
a: $d = 0.1a$ (*1*), $0.5a$ (*2*), a (*3*), ∞ (*4*), ∞ (Ref. 80) (*5*); *b*: $d = 0.1a$ (*1*), $0.5a$ (*2*), a (*3*)

5.3.1. Interaction of a nanoparticle of a given shape with a solid surface

We compare the interaction between a nanoparticle and a uniform flat solid surface for three types of particles: a sphere of radius a_c, a cylindrical disk of radius a_d and thickness d, and a cylindrical rod of radius and length L. Both of the two last particles are cylinders, but we give them different orientations with respect to a solid surface. We will call 'disk' a cylinder with an axis perpendicular to the surface. Accordingly, a rod is a cylinder with an axis parallel to the surface (Fig. 29). The disk can be considered as a model of lamellar nanoparticles, and the rod as a model of rod-shaped nanoparticles.

Let us turn to the calculation of the energy and force of the dispersion interaction of a nanoparticle with a solid substrate in the framework of Hamaker's approach. We refer subscripts 1 and 2 to the solid and to the particle, respectively. The energy of interaction of a single atom with a solid of volume V_1 at a distance z from the solid surface is known to be

$$U(z) = c_1 \int_{V_1} \mathrm{d}V_1 \Phi_{12} = -\frac{\pi c_1 A_{12}}{6z^3} \tag{153}$$

where the atomic density of the solid and Φ_{12} is the pair potential given by Eqn (1).

To obtain the energy of the interaction between the particle as a whole and the solid, we have to add the integration over the volume V_2 of the particle with the atomic density c_2. The result for a spherical particle of radius a_s was obtained by Hamaker [4] in the form

$$U_s = c_2 \int_{V_2} \mathrm{d}V_2 U(z) = -\pi A \left(\ln \frac{H}{H+2a_s} + \frac{a_s}{H} + \frac{a_s}{H+2a_s} \right) \tag{154}$$

where H is the closest distance between the ball and the solid surface (the width of the gap between them), $A \equiv A_{12} c_1 c_2$ is a constant. By differentiating energy U_s with respect to H with the direction of the z-axis from the solid surface to the ball, the expression for the force (formally, the z-component of the force vector) of attraction of the ball by the solid is [4]

$$F_s = -\frac{\partial U_s}{\partial H} = -A \frac{4\pi a_s^3}{H^2 (H+2a_s)^2} \tag{155}$$

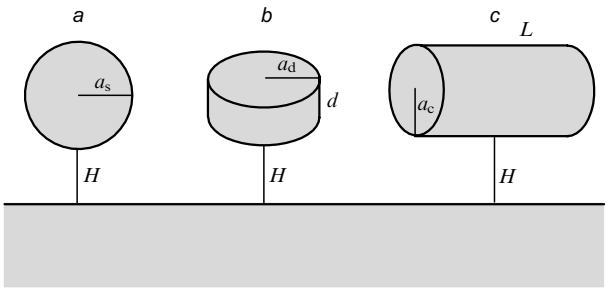


Figure 29. Nanoparticles of various shape near a solid surface: a ball of radius a_s (*a*), a cylindrical disk of thickness d and radius a_d (*b*), and a cylindrical rod of length L and radius a_c (*c*).[75]

Similarly, we find the formulas for the energy U_d and the force F_d of attraction of a cylindrical disk of radius a_d and thickness d:[92]

$$U_d = -A \frac{\pi a_d^2 d(2H+d)}{2H^2 (H+d)^2} \tag{156}$$

$$F_d = -A \frac{\pi a_d^2 d\left(3H^2 + 3Hd + d^2\right)}{H^3 (H+d)^3} \tag{157}$$

We also derive corresponding formulas for a cylindrical rod of radius a_c and length L:[92]

$$U_c = -A \frac{\pi a_c^2 L}{H^{3/2} (H+2a_c)^{3/2}} \tag{158}$$

$$F_c = -A \frac{3\pi a_c^2 L (H+a_c)}{H^{5/2} (H+2a_c)^{5/2}} \tag{159}$$

All the expressions obtained are monotonic functions of the distance H between the particles and the solid surface. The absolute values of both the energy and the force of interaction with a solid will decrease with increasing H and increase with increasing the particle size. If the particles have the same volume, but differ in shape, then the question arises: what is the ratio of the energies and forces of their interaction with a solid substrate. To secure equality of the particle volumes, the following conditions should be satisfied:

$$a_d^2 d = a_c^2 L = \frac{4}{3} a_s^3 \tag{160}$$

If we choose the value of a_d a unit for measuring distance, then for a given disk thickness d, the ball radius is uniquely determined, but one of the parameters of the rod can change independently.

Using the above formulas, one can compare the interaction with a solid for nanoparticles of different shapes. Figure 30 shows the dependence of forces on the reduced distance of the closest approach H/a_d for a sphere, a disk and two rods with $L = 10d$ and $L = 20d$ for three given values of d/a_d: 0.1 (*a*), 1 (*b*), and 5 (*c*). The force values are measured in units of A/a_d. In the interval of H/a_d under consideration, the force functions demonstrate a similar behavior. It can be seen that for $d \ll a_d$, the force of interaction of the ball with the solid is inferior to the forces for other particles. So in this criterion, the interaction of a ball with a solid is less energetically beneficial than for a disk and rods. It is worth paying attention to the change in the ratio of forces for the disk and rods with a change in the thickness of the disk. In the case of a thin disk with $d = 0.1a_d$, its interaction with a solid is more preferable than for rods, as can be seen from Fig. 30*a*. With an increase in the disk thickness to $d = a_d$, the ratios of forces change to the opposite (Fig. 30*b*). For rods, the obvious relation is preserved: the longer a rod, the stronger its interaction with a solid body (see Fig. 30).

Investigating the limiting values of the functions presented by Eqns (155) and (157) for $d \to \infty$, it is easy to verify that there is an interval of d where the interaction of a more compact ball particle will be stronger even in comparison with a semi-infinite cylinder. Therefore, we can expect a distance region to appear for sufficiently thick disks, where the interaction of the ball will exceed the interaction

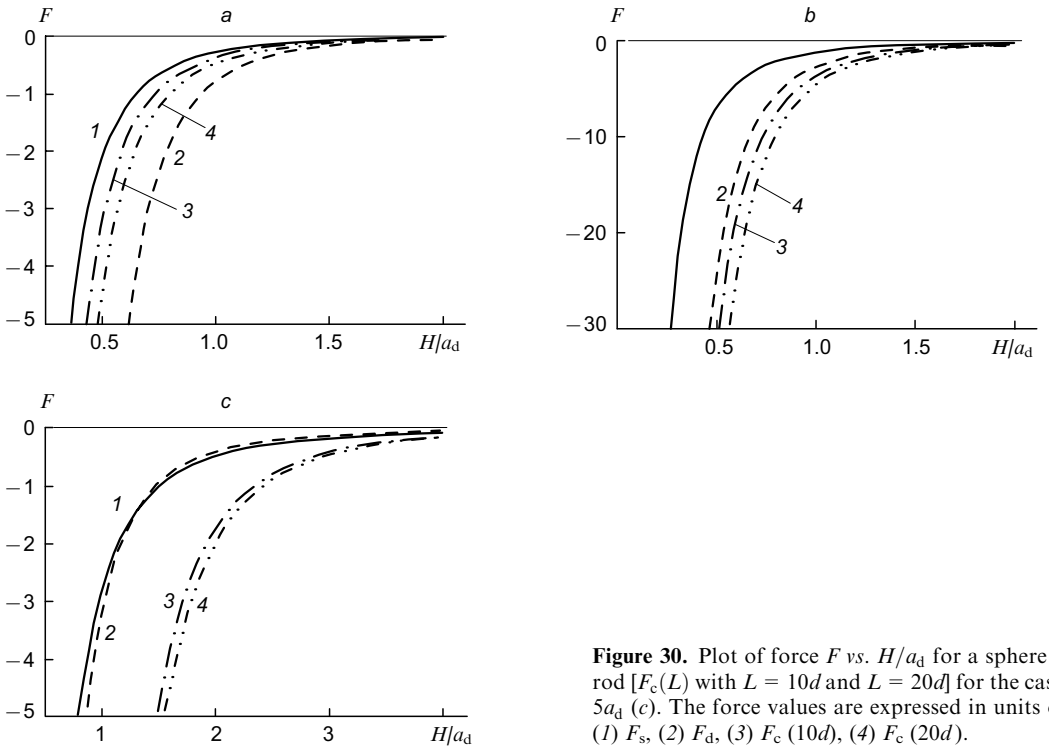


Figure 30. Plot of force F *vs.* H/a_d for a sphere (F_s), a disk (F_d), and a rod [$F_c(L)$ with $L = 10d$ and $L = 20d$] for the cases $d = 0.1a_d$ (*a*), a_d (*b*), $5a_d$ (*c*). The force values are expressed in units of A/a_d.[75] (*1*) F_s, (*2*) F_d, (*3*) F_c (10*d*), (*4*) F_c (20*d*).

of the disk. This is just what we see in Fig. 30 *c*. It can be seen that the attraction of a disk $5a_d$ thick will be stronger than that of a ball near the surface, but the ratio of forces for the ball and the disk is reversed with an increase in the gap. This happens at $H \approx 1.25a_d$.

The shape of a body is always associated with the distribution of substance of the body in space, and, therefore, with the position of its center of mass. Comparing the interaction of particles with a solid with the same gap, we do not exclude the difference in the position of their centers of mass, which actually means different removal of particles of different shapes from the surface of a solid and the associated trivial effect (the farther the particle, the it interacts less well). To exclude it, it is necessary to compare the intensity of the interaction of particles with a solid body at the same distance (we denote it H_0) of their centers of mass from the surface. To do this, we have to replace H with H_0 as for a sphere in Eqns (154) and (155), H with $H_0 - 0.5d$ for a disk in Eqns (156) and (157), and H with $H_0 - a_c$ for a rod in Eqns (158) and (159). In particular, this leads to relationships for the forces.

$$F_s(H_0) = -A\frac{4\pi a_s^3}{(H_0^2 - a_s^2)^2} \tag{161}$$

$$F_d(H_0) = -A\frac{\pi a_d^2 d(3H_0^2 + 0.25d^2)}{(H_0^2 - 0.25d^2)^3} \tag{162}$$

$$F_c(H_0) = -A\frac{3\pi a_c^2 L H_0}{(H_0^2 - a_c^2)^{5/2}} \tag{163}$$

On going to this method of description, the overall picture changes somewhat. First, for particles of different

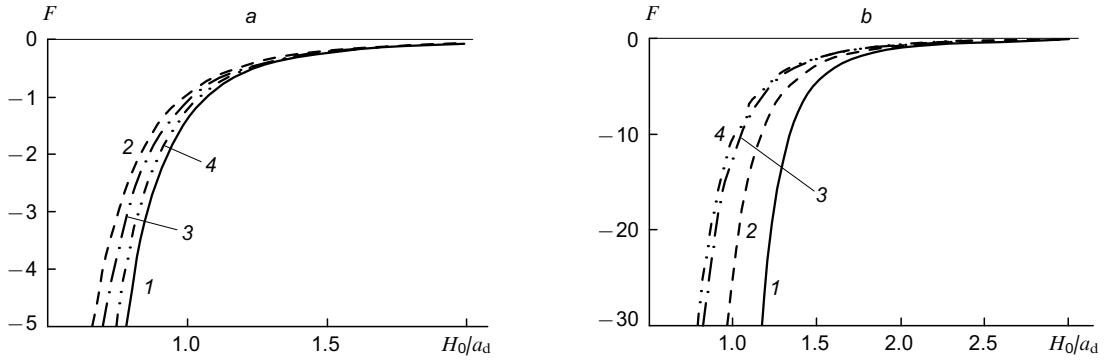


Figure 31. Dependence of the interaction force F on the distance from the centre of mass of a particle to the solid surface H_0 for a sphere (F_s), a disk (F_d), and rods [$F_c(L)$ at $L = 10d$ and $L = 20d$) for the cases with $d = 0.1a_d$ (*a*) and $d = a_d$ (*b*). The force is measured in the A/a_d units.[75] (*1*) F_s, (*2*) F_d, (*3*) F_c (10*d*), (*4*) F_c (20*d*).

types, the lower limit of the available distances will be different. Therefore, a comparison of functions of the particles must be carried out in the distance region, starting with the largest value of the lower boundary. In the case of thin disks and rods, it will be greatest for a ball whose energy and force will exceed, in absolute value, the corresponding characteristics of the other particles.

Figure 31 compares the forces calculated by Eqns (155), (157), and (159) for two cases: $d = 0.1a_d$ and $d = a_d$. The energy demonstrates the same character of dependencies. Obviously, for $d = a_d$, all dependences are shifted to the region of large values of the gap width. In this case, the predominance of the force of interaction of the ball with respect to both the disk and rod becomes more pronounced. The ratios of forces for the disk and rods will remain the same as when considering the dependences on the distance H of the closest approach. Namely, thin disks are superior to rods in both the energy and force of interaction. Conversely, thick disks lose interaction as compared to rods. It should be said that for $d \geqslant 2.45a_d$, when the distance from the solid surface to the centre of mass becomes larger for a disk than for a ball, the ratio of the interactions of a disk to a ball becomes more complex. As noted above, as the disk thickness increases, its interaction approaches the interaction of a semi-infinite cylinder. In this limit, it already becomes meaningless to describe its interaction in terms of the distance from the center of mass of a particle to the solid surface. Then one needs to return to using the closest distance H, as was mentioned above in the discussion of Fig. 30. In these cases, there is such a value of H at which the ratio of forces for the ball and the change in opposite directions.

5.3.2. Energy and force shape factors

Along with the energy and force of interaction themselves, we can introduce shape factors[93] for a more obvious comparison of the kinds of interaction of various particles. Usually the shape factor (we denote it as Θ) is the ratio of corresponding functions for bodies of the same volume but different shape. We will determine the shape factor for a particle in question with respect to the ball. In view of Eqns (154) and (156), the energy shape factor for a disk can be written in the form

$$\Theta_U^{\mathrm{d}} = \frac{a_{\mathrm{d}}^2 d(2H+d)}{2H^2(H+d)^2\left(\ln\dfrac{H}{H+2a_{\mathrm{s}}} + \dfrac{a_{\mathrm{s}}}{H} + \dfrac{a_{\mathrm{s}}}{H+2a_{\mathrm{s}}}\right)} \tag{164}$$

As for the force shape factor for a disk, it follows from Eqns (155) and (157) as

$$\Theta_F^{\mathrm{d}} = \frac{\left(3H^2+3Hd+d^2\right)(H+2a_{\mathrm{s}})^2}{3H(H+d)^3} \tag{165}$$

Similarly, using Eqns (154) and (158), the energy shape factor for a rod is

$$\Theta_U^{\mathrm{c}} = \frac{a_{\mathrm{c}}^2 L}{H^{3/2}(H+2a_{\mathrm{c}})^{3/2}\left(\ln\dfrac{H}{H+2a_{\mathrm{s}}} + \dfrac{a_{\mathrm{s}}}{H} + \dfrac{a_{\mathrm{s}}}{H+2a_{\mathrm{s}}}\right)} \tag{166}$$

and, on the basis of Eqns (155) and (159), the force shape factor for a rod is

$$\Theta_F^{\mathrm{c}} = \frac{(H+a_{\mathrm{c}})(H+2a_{\mathrm{s}})^2}{H^{1/2}(H+2a_{\mathrm{c}})^{5/2}} \tag{167}$$

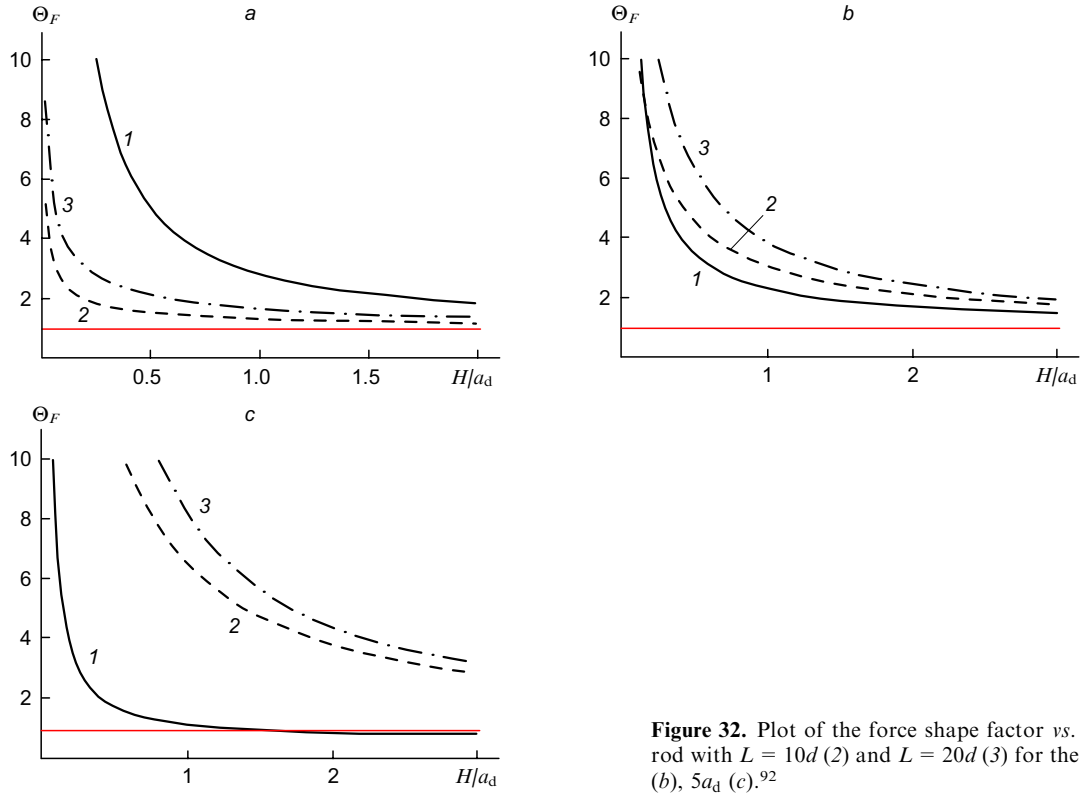


Figure 32. Plot of the force shape factor *vs.* H/a_{d} for a disk (*1*), a rod with $L = 10d$ (*2*) and $L = 20d$ (*3*) for the cases $d = 0.1a_{\mathrm{d}}$ (*a*), a_{d} (*b*), $5a_{\mathrm{d}}$ (*c*).[92]

Obviously, with an infinite increase in the distance of the particles to the surface, all the shape factors of the particles will tend to unity. Figure 32 compares the force shape factors calculated by Eqns (165) and (167) for $d = 0.1a_d$, $d = a_d$, and $d = 5a_d$. The same character of dependencies is demonstrated by the energy shape factors.

Obviously, with an infinite increase in the distance of the particles to the surface, all the shape factors of the particles will tend to unity. Figure 32 compares the force shape factors calculated by Eqns (165) and (167) for $d = 0.1a_d$, $d = a_d$, and $d = 5a_d$. The same character of dependencies is demonstrated by the energy shape factors.

In the case of a thin disk with $d = 0.1a_d$, its interaction with a solid is more preferable than for rods, and the force shape factor for it exceeds the shape factors for rods (curve *1* in Fig. 32 *a*). As the disk thickness increases to $d = a_d$, the ratios of the shape factors (as well as the forces themselves) change to the opposite (curve *1* in Fig. 32 *b*). For the case of a disk with $d = 5a_d$, with increasing distance, a range appears where the shape factor is less than unity (Fig. 32 *c*). If we recall that the shape factor in the limit should tend to unity, we conclude that the shape factor for disks with large values of d will pass through a minimum value. As for rods, the obvious relation is preserved: the longer a rod, the stronger its interaction with a solid (curves *3* and *4* in Fig. 32).

As for energy and force, the corresponding shape factors can be compared at the same distance of their centers of mass from the surface. To do this, we replace H with $H_0 - 0.5d$ for a disk in Eqns (164) and (165) and H with $H_0 - a_c$ for a rod in Eqns (166) and (167). In particular, for the force shape factor of the particles, we obtain the following formulas

$$\Theta_F^{d}(H_0) = \frac{(3H_0^2 + 0.25d^2)(H_0^2 - a_s^2)^2}{3(H_0^2 - 0.25d^2)^3} \tag{168}$$

$$\Theta_F^{c}(H_0) = \frac{H_0(H_0^2 - a_s^2)^2}{(H_0^2 - a_c^2)^{5/2}} \tag{169}$$

Figure 33 shows the force shape factors of various particles with respect to the ball, depending on the distance of the center of mass of the particles H_0 to the solid surface, obtained from Eqns (168) and (169).

Obviously, with an increase in the distance from the solid surface, functions $\Theta_F^{d}(H_0)$ and $\Theta_F^{c}(H_0)$ tend to unity as well as functions $\Theta_F^{d}(H)$ and $\Theta_F^{c}(H)$, but in quite different ways. In the latter case, the shape factors tend to unity from above large values in narrow slits, whose width can be arbitrarily small (see Fig. 32). When passing to the center of mass of the particles, the region of infinitely narrow slits becomes inaccessible to the ball, which limits from below the domain of definition of the functions under consideration. As the slit width increases, these functions of H_0 tend to unity from below beginning from infinitely small values in narrow slits. When comparing the shape factors of disks and rods, it can be seen that with an increase in the thickness of the disk, its force shape factor increases with respect to the rod (see Fig. 33). Thus, when comparing nanoparticles with a different shape, but with the same volume and the same distance of their centers of mass from a solid surface, the interaction of the ball with the solid surface is stronger than the others. This conclusion is valid in the range of the disk thickness $d \leqslant 2.45a_d$, until the center of mass of the ball limits the range of accessible distances from the surface of a solid. However, spherical particles lose their advantage if the gap (H) between the solid surface and a particle is the same for all particles.

6. Contribution of dispersion forces to surface, line, and point tension

6.1. Basic concepts

Adjacent bulk phases are known to create surfaces. Intersection of surfaces creates lines, as well as intersection of lines creates points. Phase volumes, surfaces, lines, and points are basic elements of every heterogeneous system. Correspondingly, the work of their formation and their thermodynamic characteristics including surface, line, and point tensions, are basic elements of surface science. Since Gibbs discovered the duality of surface tension of solids,[93] the problem of a definition of this quantity became a subject of multiple discussions (see surveys[48,49,94,95]). We here consider the thermodynamic surface tension (designated as σ by Gibbs and different from the ordinary mechanical surface tension) defined as a half of the work of cleavage per unit surface area. The latter is the work of disjoining two pieces of a solid (divided by a plane) from the intermolecular distance δ in the solid to infinity in a vacuum. So the definition of σ can be written as

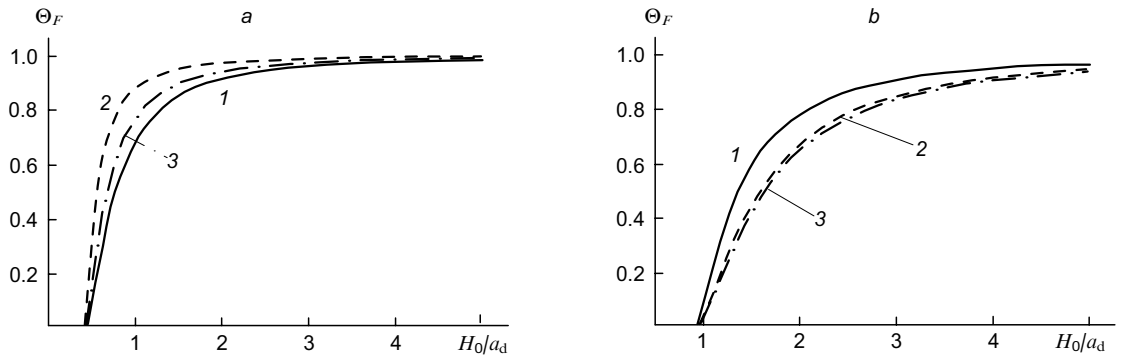


Figure 33. Figure 33. Plot of the force shape factor Θ_F *vs.* H/a_d for a disk (*1*) and a rod with $L = 10d$ (*2*) and $L = 20d$ (*3*) for the cases $d = 0.1a_d$ (*a*) and $d = a_d$ (*b*).[92]

$$2\sigma = \int_{\delta}^{\infty} f(H)\mathrm{d}H \tag{170}$$

where H is the width of a slit between the pieces and $f(H)$ is the cohesive force per unit area. Equation (170) implies the work process to be isothermal, which corresponds to the choice of free energy as a thermodynamic potential.

Similarly to the surface tension, the line tension can also have multiple interpretations.[94] We here deal with the thermodynamic line tension κ as the work of formation of the solid edge per unit length. This additional work originates from the fact that surface tension changes when approaching an edge at the nano-scale. If σ is the surface tension value sufficiently far from the edge and $\sigma(x)$ is the local surface tension value on the distance x from the edge, the thermodynamic line tension at the edge is

$$\kappa \equiv \frac{1}{L}\sum\int[\sigma(x)-\sigma]\mathrm{d}A \tag{171}$$

where L is the edge length and A is the surface area, the integration is carried out over each surface and summation over all surfaces meeting at the edge.

The point tension η is defined analogously. If the edge line is restricted and has an end, the local line tension $\kappa(x)$ is a function of distance x from the edge end. Then the point tension is defined by the following expression:

$$\eta \equiv \sum\int[\kappa(x)-\kappa]\mathrm{d}L \tag{172}$$

where κ is $\kappa(x)$ at $x = \infty$. The integration is carried out over whole length L and summation over all lines meeting at the point. The result of integration is dependent on L provided L lies within the nano-scale. Otherwise, the integrand in Eqn (172) practically vanishes for sufficiently large x, and the point tension acquires the status of a constant.

As is well seen from Eqns (170)–(172), the calculation of all tensions becomes possible if one can estimate the cohesive force $f(H)$ not as an average but as a local quantity. This is attained by using the Irving–Kirkwood stress tensor, Eqn (10), which, in this way, acts as a direct tool for calculating the surface, line, and point tensions. Such calculations require a pair potential not only for large R, but for all R beginning from δ as an intermolecular distance in a solid. This can be a model potential, for example, the classical Lennard-Jones potential

$$\Phi(R) = 4\varepsilon_{\mathrm{LJ}}\left[\left(\frac{\sigma_{\mathrm{LJ}}}{R}\right)^{12} - \left(\frac{\sigma_{\mathrm{LJ}}}{R}\right)^{6}\right] \tag{173}$$

with constants $\varepsilon_{\mathrm{LJ}}$ and σ_{LJ} and with the second attractive term corresponding to dispersion forces, Eqn (1). The distance δ corresponds to the balance of attraction and repulsion forces in a solid. When integrating over $R > \delta$, repulsion forces dramatically decrease, and their resulting contribution to the integral value can be small as compared with the contribution of dispersion forces. This means that using Eqn (1) instead of Eqn (173), we obtain a result at least of the same order of magnitude. However, strictly speaking, we estimate only a contribution of dispersion forces to a quantity under question when using Eqn (1).

According to the definition formulated in Eqn (170) through isothermal work, a certain temperature should be chosen and a corresponding pair potential should be taken for calculations. If the temperature is absolute zero (which is typical for quantum chemistry), the difference between energy and free energy disappears. Then one can say that Eqn (170) determines not only surface tension but also surface energy. As the temperature grows, the difference between surface tension and surface energy rapidly increases because of entropy. However, surface energy changes slightly, and, in contrast with surface tension, the surface energy value calculated at zero temperature can be useful for higher temperatures. The same may be said about line and point energy.

The concept of thermodynamic surface and line tensions has found wide application in the theory of cracks.[53] As for solid edges, only the case of a rectilinear edge of a semi-infinite slit [70, 71, 96, 97] was also reviewed in Ref. 53. Later on, the general case of a curved solid edge was analyzed.[98] We present the result below. Line tension is also one of central concepts of the thermodynamics of graphene as a two-dimensional structure [99] where line tension plays the same role as surface tension for three-dimensional bodies. The line energy of graphene was calculated up to a numerical value.[99, 100] As for the point energy, an analog of surface energy for three-dimensional bodies, there was no data to be included in Ref. 100. Only recently, the estimation of the contribution of dispersion forces to the point energy of graphene was made.[101] We will also present this result in Section 6.3, which plays the role of a certain supplement to Ref. 100.

6.2. Line tension at the curved edge of a molecular solid

Let us return to the case of two coaxial cylinders of radius a separated by distance H (Section 5.2) and investigate the line tension of the circular edge.[98] According to the computational scheme described in Section 6.1, we have, as a preliminary, to calculate the local thermodynamic surface tension on both sides of the circular slit between the two cylinders. Addressing first an infinite slit of width H and using Eqn (87), we can write

$$f(H) = -p_{\mathrm{N}}(H) = \frac{\pi A}{6H^3} \tag{174}$$

where, to remind, $A \equiv \sum_{s,t} A_{st}c_s c_t$ [see Eqn (24)], c_s being the molecular concentration of component s (the two cylinders can be of different nature and composition). Then putting Eqn (174) in Eqn (170) yields a macroscopic value for surface tension

$$\sigma = \frac{\pi A}{24\delta^2} \tag{175}$$

As for the local (as a function of the radial coordinate r) surface tension on the circular slit surface, we can define it as

$$2\sigma(r,a,\delta) = -\int_{\delta}^{\infty} p_{\mathrm{N}}(r,a,H)\mathrm{d}H \tag{176}$$

similarly to Eqn (170). Using Eqns (132) and (175), we can accomplish analytically the integration over the slit width to obtain

$$\sigma(\tilde{r},\tilde{a}) = \sigma[1 - f_{\sigma}(\tilde{a},\tilde{r})] \tag{177}$$

where

$$f_\sigma(\tilde{a},\tilde{r}) = \frac{3}{8\pi}\left[\int_0^{2\pi} \mathrm{d}\varphi F_1(\tilde{\rho}_{1a}) + 3\int_0^{2\pi}\mathrm{d}\varphi\int_0^{\tilde{\rho}_{1a}} \tilde{\rho}\mathrm{d}\tilde{\rho}\,\frac{F_2(\tilde{\rho})}{(\tilde{\rho}+\tilde{\rho}_{2a})^4}\right] \quad (178)$$

$$F_1(\tilde{\rho}_{1a}) \equiv \frac{1}{\tilde{\rho}_{1a}^2+1} + \frac{1}{\tilde{\rho}_{1a}^2} + \frac{1}{\tilde{\rho}_{1a}^3}\left(\arctan\frac{1}{\tilde{\rho}_{1a}} - \frac{\pi}{2}\right) \quad (179)$$

$$F_2(\tilde{\rho}) = 2 - \frac{7}{3(\tilde{\rho}^2+1)} + \frac{4}{3(\tilde{\rho}^2+1)^2} + \frac{1}{\tilde{\rho}}\left(\arctan\frac{1}{\tilde{\rho}} - \frac{\pi}{2}\right) \quad (180)$$

and tilde means the ratio of a corresponding quantity to the intermolecular distance δ: $\tilde{r} \equiv r/\delta, \tilde{a} \equiv a/\delta$, and $\tilde{\rho} \equiv \rho/\delta$. Figure 34 exhibits the function $\sigma(\tilde{r},\tilde{a})/\sigma$ as a result of numerical integration.

It is seen from Fig. 34 that local surface tension in the central part of a circular slit only slightly differs from its macroscopic value σ: the deviation is smaller than 1% at and is noticeable only on the nanoscale at $a < 20\delta$. However, essential deviations appear at the slit edge where the function $\sigma(\tilde{r},\tilde{a})/\sigma$ dramatically decreases giving evidence of existing a negative line tension.

Following Eqn (111), we now can calculate line tension as

$$\kappa(a) = \frac{1}{a}\int_0^a [\sigma(r,a) - \sigma]\, r\mathrm{d}r = \frac{1}{a}\int_0^a \sigma(r,a)\, r\mathrm{d}r - \frac{\sigma a}{2} \quad (181)$$

Substituting Eqn (177) in Eqn (181) yields

$$\frac{\kappa(\tilde{a})}{\sigma\delta} = -\frac{1}{\tilde{a}}\int_0^{\tilde{a}} \tilde{r}\mathrm{d}\tilde{r} f_\sigma(\tilde{a},\tilde{r}) \quad (182)$$

where $f_\sigma(\tilde{a},\tilde{r})$ is given by Eqn (178). The result of integration of Eqn (182) is shown in Fig. 35.

The figure shows line tension to be negative and strongly dependent on the edge curvature on the nanoscale. The smaller the curvature radius, the lower the line tension in its absolute value. In the opposite limit of a large radius, line tension tends to its constant value for a rectilinear edge. The approximate limiting value was estimated as -0.676,[96] which is in good agreement with Fig. 35. This is the only fact which can confirm the validity of this result because there are no data on the dependence of line tension on the edge curvature in the literature.

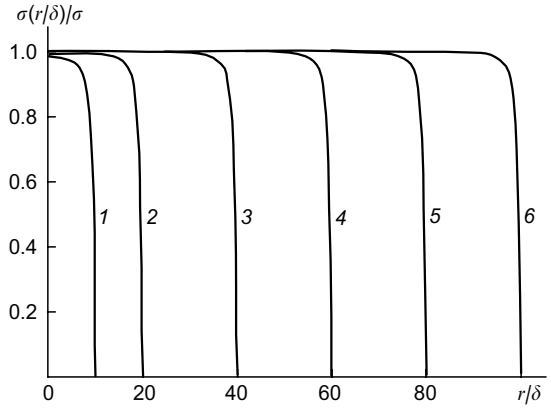


Figure 34. Plot of the relative local surface tension $\sigma(\tilde{r},\tilde{a})/\sigma$ *vs.* $\tilde{r}$ for the slit radius $\tilde{a}$ of 10 (curve *1*), 20 (*2*), 40 (*3*), 60 (*4*), 80 (*5*), and 100 (*6*).[98]

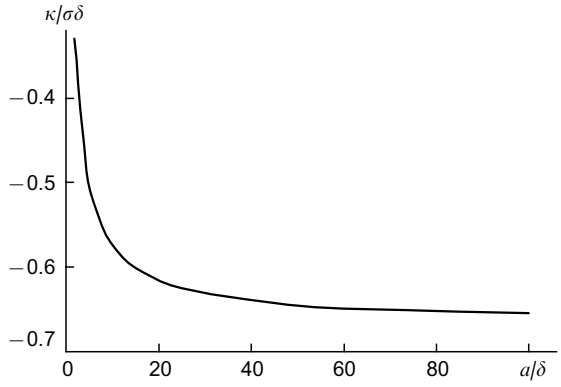


Figure 35. Dependence of line tension on the line radius.[98]

Concluding the section, note that our calculations implied the existence of a certain pair potential constructed for a given temperature. The parameters of the potential remained unknown, but this did not prevent the creation of a new theory due to the fact that the result was expressed in relative terms. A general regularity, the curvature dependence of line tension, was established. However, we did not calculate the numerical value of line tension because that operation would require the pair potential parameters. Since quantum chemistry produces pair potentials typically for zero temperature, the numerical estimation of thermodynamic surface, line, and point tensions becomes possible at zero temperature. According to the said in Section 6.1, we are talking about surface, line, and point energy in this case. Such calculation is illustrated below using the example of the line and point energy of graphene.

6.3. Line and point energy of graphene

Bearing in mind graphene, silicene, germanene, and analogous two-dimensional structures of the future, we split this section into two parts. In the first part, we construct a general theory similar to the given above for line tension and applicable to any two-dimensional body. The second part is devoted to calculating specific parameters of graphene on the basis of the general theory. Addressing the calculations to zero temperature, we will replace thermodynamic tension with energy.

6.3.1. General relationships for two-dimensional structures

On passing to two-dimensional bodies, the role of surface energy goes to line energy ε. Correspondingly, Eqn (170) is replaced by the relationship

$$2\varepsilon = \int_\delta^\infty f(H)\mathrm{d}H \quad (183)$$

where $f(H)$ is the cohesive force per unit length of a two-dimensional rectilinear slit of width H between two coplanar graphene sheets with parallel boundaries. Width H is not a local quantity and is the same at every point of the slit. However, if the slit is finite and x is the distance from the slit end, $f(H)$ acquires a local meaning $f(H,x)$. Then, following Eqn (183), the local line energy $\varepsilon(x)$ is defined as

$$2\varepsilon(x) = \int_{\delta}^{\infty} f(H,x)\mathrm{d}H \tag{184}$$

By analogy with Eqn (172), we define the point energy (with the same notation as point tension at zero temperature)

$$\eta \equiv \int [\varepsilon(x) - \varepsilon]\mathrm{d}L \tag{185}$$

where ε is the line energy value far from the slit end (where ε does not depend on x). After giving necessary definitions, we can proceed to calculations.

6.3.1.1. Cohesive force

To calculate the cohesive force, we identify it with the normal component E_N of the stress tensor on one of the boundary lines of the two-dimensional slit:

$$f(H,x) = E_{\mathrm{N}} \tag{186}$$

This quantity can be calculated by means of the Irving–Kirkwood stress tensor, Eqn (10), which, being formulated in tensoric and vector forms, is easily applicable to the two-dimensional case. Retaining only the force term in Eqn (10), we can write

$$\hat{E}(\mathbf{r}) = \frac{1}{2}\sum_{s,t}\int \frac{\mathbf{R}\times\mathbf{R}}{R}\Phi'_{st}(R)\mathrm{d}\mathbf{R}\int_0^1 \rho_{ij}^{(2)}(\mathbf{r}-\eta\mathbf{R}, r-\eta\mathbf{R}+\mathbf{R})\mathrm{d}\eta \tag{187}$$

Turning to calculations, let us imagine that we are at the edge of a macroscopic graphene sheet of rectangular shape and make a sheet cut normal to the edge. Then we disjoin the sheet part 1 and 2 at a distance H in the same plane (Fig. 36). The whole operation is done in a vacuum (which is why we need only the force part of the stress tensor). We have now only two Cartesian coordinates, x and y, and the normal stress tensor is defined as $E_{\mathrm{N}} \equiv E_{yy}$.

Let us first transform Eqn (187). We place the calculation point $\mathbf{r}$ (at which the stress tensor is sought) on the lower side of the slit at a distance x from the slit edge (see Fig. 36). Set the origin of the Cartesian coordinates at the calculation point to direct the x-axis along the cut line to its end and the y-axis perpendicular to the cut line from the bottom to the top. As is usual, vectors $\mathbf{r}_1$ and $\mathbf{r}_2$ are directed oppositely, but lie on one straight line, since a straight line segment of length R connecting two interacting molecules must pass through the calculation point (see Fig. 36). We can then write

$$\mathbf{r}_1 = (1-\eta)\mathbf{R} \tag{188}$$

$$\mathbf{r}_2 = -\eta\mathbf{R}$$

so that $\mathbf{R} = \mathbf{r}_1 - \mathbf{r}_2$.

As applied to the two-dimensional case under consideration, the integration in Eqn (187) is performed by three variables: R_x, R_y, and η. It is convenient to change the variables to x_1, y_1 (the components of vector $\mathbf{r_1}$), and y_2 (the y-component of vector $\mathbf{r}_2$). Passing to the new variables, we also may write, as it follows from Eqn (188),

$$\mathbf{R} = \mathbf{r}_1\frac{y_1 - y_2}{y_1} \tag{189}$$

$$R = r_1\frac{y_1 - y_2}{y_1}$$

where r_1 is the modulus of vector $\mathbf{r}_1$. From Eqn (189), it follows the relation

$$\frac{\mathbf{R}\times\mathbf{R}}{R} = \frac{\mathbf{r}_1\times\mathbf{r}_1}{r_1}\cdot\frac{y_1 - y_2}{y_1} \tag{190}$$

We now turn to the two-particle distribution function $\rho_{ij}^{(2)}$ in Eqn (187). For the solid two-dimensional object under consideration, assuming it to be uniform in density, we can represent the two-particle distribution function as a product of one-particle distribution functions in regions 1 and 2:

$$\rho_{12}^{(2)} = \rho_1^{(1)}\rho_2^{(1)} \tag{191}$$

We set the one-particle distribution functions in the form

$$\rho_1^{(1)}(y) = \rho \ (y_1 > H) \tag{192}$$

$$\rho_1^{(1)}(y) = 0 \ (y_1 < 0) \tag{192a}$$

$$\rho_2^{(1)}(y) = \rho \ (y_2 < 0) \tag{192b}$$

$$\rho_2^{(1)}(y) = 0 \ (y_2 > H) \tag{192c}$$

where ρ is the two-dimensional density (the number of carbon atoms per unit area) of graphene (to be a constant). Inside the empty slit between regions 1 and 2, this density is obvious to be zero. In addition, both conditions in Eqns (192)–(192c) do work only within the slit length. There is no substance beyond the slit length, and, therefore, the Irving–Kirkwood stress tensor is zero. It is easy to compare that it is also zero at the slit end. Indeed, if we place the calculation point at the very edge of the slit (at $x = 0$), then the straight line segment R passing through the point can only move in the following way. If one of the segment ends is located in region 1 or in region 2 with a substance, the second end inevitably falls into vacuum. In any case, there will be no interaction.

After all above transformations, Eqn (187) acquires the form [101]

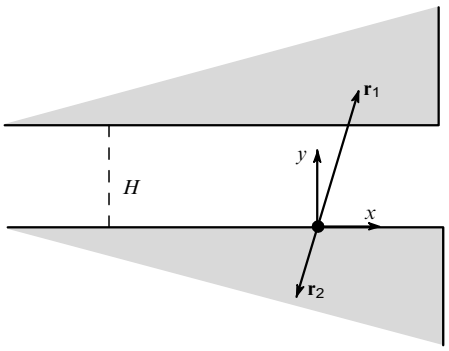


Figure 36. The formation of two corners by cutting a semi-infinite graphene sheet: H is the distance between the two parts of the sheet, vectors $\mathbf{r}_1$ and $\mathbf{r}_2$ show the location of the atoms interacting through the point (the black circle) where the stress tensor is searched.[101]

$$\hat{E} = -\rho^2 \int_H^\infty \mathrm{d}y_1 \int_{-\infty}^0 \mathrm{d}y_2 \int_{xy_1/y_2}^x \mathrm{d}x_1 \frac{\mathbf{r}_1 \times \mathbf{r}_1}{r_1} \times \tag{193}$$

$$\times \frac{y_1 - y_2}{y_1^2} \Phi'_{12}\left[\frac{r_1(y_1 - y_2)}{y_1}\right]$$

Eqn (193) is valid for pair potential of any kind. Turning now to dispersion forces (without retardation), we write Eqn (1) as

$$\Phi_{12}(R) = -\frac{\lambda}{R^6} (R \geqslant \delta) \tag{194}$$

where $\lambda \equiv A_{12}$ (for the sake of brevity and accordance with the notation given in Ref. 99). Accounting for Eqn (189), Eqn (194) becomes

$$\Phi_{12}\left[\frac{r_1(y_1 - y_2)}{y_1}\right] = -\frac{\lambda y_1^6}{r_1^6 (y_1 - y_2)^6} \tag{195}$$

Then substituting Eqns (194)–(195) in Eqn (193) yields

$$\hat{E} = 6\lambda\rho^2 \int_H^\infty y_1^5 \mathrm{d}y_1 \int_{-\infty}^0 \frac{\mathrm{d}y_2}{(y_1 - y_2)^6} \int_{xy_1/y_2}^x \mathrm{d}x_1 \frac{\mathbf{r}_1 \times \mathbf{r}_1}{r_1^8} \tag{196}$$

Further calculations need to be made for each component of the stress tensor separately. In accordance with Eqn (186), we are interested in the normal component $E_\mathrm{N} \equiv E_{yy}$. Replacing $\mathbf{r}_1 \times \mathbf{r}_1$ by y_1^2 and, on the way, r_1 by $(x_1^2 + y_1^2)^{1/2}$, from Eqn (186) we obtain an expression for the local cohesive force

$$f(H, x) = E_\mathrm{N} = 6\lambda\rho^2 \int_H^\infty y_1^7 \mathrm{d}y_1 \int_{-\infty}^0 \frac{\mathrm{d}y_2}{(y_1 - y_2)^6} \int_{xy_1/y_2}^x \frac{\mathrm{d}x_1}{(x_1^2 + y_1^2)^4} \tag{197}$$

For $x \to \infty$, Eqn (197) takes an easily integrable form to yield

$$f(H) = \frac{3\pi\lambda\rho^2}{32H^4} \tag{198}$$

As for Eqn (197) in general, its integrals, of course, are also taken, but the results would look too cumbersome. Below we give a final formula of this type, but for now we leave Eqn (197) as the most compact notation for the local cohesive force.

6.3.1.2. Local line energy

From Eqns (184) and (198), we find the contribution of dispersion forces to the line energy of the infinitely long rectilinear boundary of the graphene sheet as

$$\varepsilon = \frac{1}{2} \int_\delta^\infty f(H) \mathrm{d}H = \frac{3\pi\lambda\rho^2}{64} \int_\delta^\infty \frac{\mathrm{d}H}{H^4} = \frac{\pi\lambda\rho^2}{64\delta^3} \tag{199}$$

which is consistent with the result of the calculation by other means.[99, 100] As for the local line energy near the corner of a two-dimensional structure, from Eqns (184) and (197), we find

$$\varepsilon(x) = 3\lambda\rho^2 \int_\delta^\infty \mathrm{d}H \int_H^\infty y_1^7 \mathrm{d}y_1 \int_{-\infty}^0 \frac{\mathrm{d}y_2}{(y_1 - y_2)^6} \int_{xy_1/y_2}^x \frac{\mathrm{d}x_1}{(x_1^2 + y_1^2)^4} \tag{200}$$

Expressing now x_1, y_1, y_2, and H in units of δ and using Eqn (199), we simplify Eqn (200) to the form

$$\frac{\varepsilon(x)}{\varepsilon} = \frac{192}{\pi} \int_1^\infty \mathrm{d}H \int_H^\infty y_1^7 \mathrm{d}y_1 \int_{-\infty}^0 \frac{\mathrm{d}y_2}{(y_1 - y_2)^6} \int_{xy_1/y_2}^x \frac{\mathrm{d}x_1}{(x_1^2 + y_1^2)^4} \tag{201}$$

Omitting the calculation details,[101] here we immediately give the final result of integration in Eqn (201)

$$\frac{\varepsilon(x)}{\varepsilon} = \big[9\pi - 18x + 54\pi x^2 - 102x^3 + 135\pi x^4 \tag{202}$$

$$-714x^5 + 810\pi x^6 + 634x^7 - 810\pi x^8 + 1242x^9 +$$

$$+ 558\pi x^{10} + 78x^{11} + 243\pi x^{12} + 130x^{13} + 90\pi x^{14} + 30x^{15} +$$

$$+ 15\pi x^{16} + (30x^4 + 180x^6 + 450x^8 + 600x^{10} + 450x^{12} +$$

$$+ 180x^{14} + 30x^{16}) \arctan x - (18 + 108x^2 + 270x^4 +$$

$$+ 360x^6 + 270x^8 + 108x^{10} + 18x^{12}) \arctan(x^{-1}) -$$

$$-(288x^5 - 2112x^7 + 1440x^9) \ln x]/30\pi x^4 (1 + 6x^2 +$$

$$+ 15x^4 + 20x^6 + 15x^8 + 6x^{10} + x^{12})$$

where, to remind, x should be considered as x/δ.

The graphical representation of the function given in Eqn (202) looks much simpler (Fig. 37) and predictably demonstrates an asymptotic approximation of $\varepsilon(x)$ to its constant value ε within the nano-range $0 \leqslant x/\delta \leqslant 5$. Since $\varepsilon(x) < \varepsilon$ throughout the graph, we can say in advance that, according to Eqn (185), the contribution of the dispersion forces to the point energy of a two-dimensional structure should be negative.

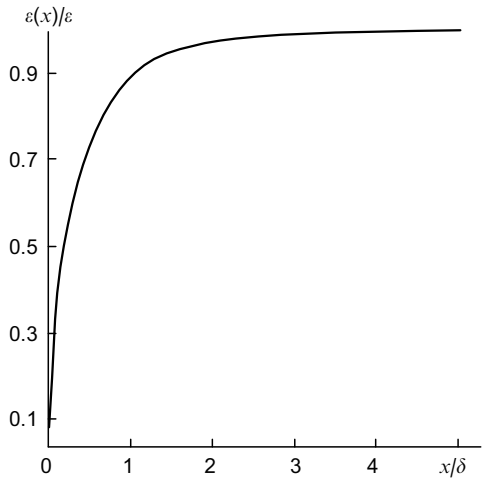


Figure 37. Approximation of the line energy of graphene $\varepsilon(x)$ to its constant value ε when moving away from the corner of a graphene sheet (δ is the minimum interatomic distance across the boundary line).[101]

6.3.1.3. Point energy

It remains to find the expression for the contribution of dispersion forces to the point energy η of a two-dimensional structure. We transform Eqn (185) to the form (where x is calculated in units of δ)

$$\frac{\eta}{\varepsilon\delta} = \int_0^\infty \left[\frac{\varepsilon(x)}{\varepsilon} - 1\right] \mathrm{d}x \tag{203}$$

Now, substituting Eqn (137) in Eqn (138) and integrating, we get

$$\eta = -\frac{4}{3\pi}\varepsilon\delta \tag{204}$$

After putting Eqn (199), Eqn (204) becomes

$$\eta = -\frac{\lambda\rho^2}{48\delta^2} \tag{205}$$

After the general relations for two-dimensional structures have been established, one can proceed to concrete calculations for graphene.

6.3.2. Characteristics of graphene

In graphene, the σ-bond length is $b = 0.142$ nm, and in a two-dimensional hexagonal packing, the relationship between ρ (the number of carbon atoms per unit area) and b is found as follows.[99, 100] With the length of the side of a regular hexagon b, the hexagon area is $(3/2)\sqrt{3}b^2$. Therefore, the number of hexagons per unit area will be $2/3\sqrt{3}b^2$. Each hexagon includes six carbon atoms, but each atom belongs to three hexagons at once, so

$$\rho = \frac{4}{3\sqrt{3}b^2} \approx \frac{0.7698}{b^2} \tag{206}$$

With the above value of b, Eqn (206) yields $\rho \approx 38.177$ nm^{-2}. By substituting Eqn (206) into Eqns (199) and (205), we obtain for line energy

$$\varepsilon = \frac{\pi\lambda}{108b^4\delta^3} \tag{207}$$

and for point energy

$$\eta = -\frac{\lambda}{81b^4\delta^2} \tag{208}$$

To do the calculations, we also need to set the dispersion constant λ for graphene. For this, we use the classical Lennard-Jones equation, which has been well studied in relation to the carbon–carbon (CC) pair interaction:

$$\Phi(R) = 4\varepsilon_{CC}\left[\left(\frac{\sigma_{CC}}{R}\right)^{12} - \left(\frac{\sigma_{CC}}{R}\right)^{6}\right] \tag{209}$$

The refined values of the constants of Eqn (209) are: $\varepsilon_{CC} = 0.03550 \times 10^{-20}$ J and $\sigma_{CC} = 0.34585$ nm.[99] Comparing Eqns (194) and (209), we find

$$\lambda = 4\varepsilon_{CC}\sigma_{CC}^6 \tag{210}$$

which, with the above values, gives $\lambda = 2.43005 \times 10^{-78}$ J m^6. It remains to find parameter δ, but δ is worthy of a special discussion.

6.3.2.1. Choice of parameter δ

Until now, it was only stated that δ was a minimum distance for calculations. Now it is time to specify this parameter for graphene. First of all, it is necessary to choose the direction of the cut of a graphene sheet to create a linear boundary. In this case, it is desirable to find such a direction for which the work of the section would be minimal and, therefore, corresponded to the natural linear boundary (if one tries to break a graphene sheet, then it will likely to tear in this direction). This question was discussed in detail,[99, 100] and it was found that such a cut corresponds to the breaking of σ-bonds of graphene along the zigzag-shaped border (Fig. 38). The fact that this direction corresponds to the real linear boundary of graphene was also confirmed by Li *et al.*[102] Below we will address this boundary. Further considerations require some model concepts of carbon atoms.

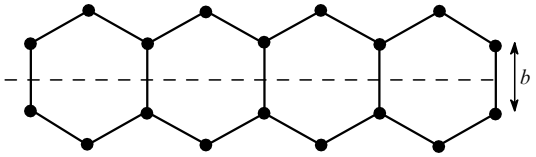


Figure 38. The boundary line of a graphene sheet across σ-bonds of length b.[101]

6.3.2.2. Model of hard balls with dispersion forces

Usually, hard balls simulate repulsive forces, but we will add a chemical bond to them. In other words, in this model, it is believed that with the slightest increase in the distance between carbon atoms in graphene, the chemical bond is broken and does not manifest itself in the future, as well as repulsive forces. This means that the dispersion forces immediately contribute to the work of separation of two pieces of graphene, as soon as the distance between the carbon atoms exceeds the lattice parameter b, *i.e.* $\delta = b$. Then Eqn (207) for line energy takes the form

$$\varepsilon = \frac{\pi\lambda}{108b^7} \tag{211}$$

and Eqn (208) for point energy becomes

$$\eta = -\frac{\lambda}{81b^6} \tag{212}$$

With the above values of λ and b, Eqns (211) and (212) yield $\varepsilon \approx 0.607 \times 10^{-10}$ J m^{-1} and $\eta \approx -0.366 \times 10^{-20}$ J.

6.3.2.3. The Lennard-Jones model

Let us imagine now that the situation with chemical bonds remains the same (they immediately break with increasing intermolecular distance in graphene), and repulsive forces acquire a small long-range action according to Eqn (173). In this case, immediately after the chemical bonds are broken by external forces, the system enters the region of repulsive forces and spontaneously (abruptly) increases the gap between the disconnected parts of the graphene sheet to a certain distance δ corresponding to the equilibrium between the forces of attraction and repulsion. A further increase in the distance will already require the work of external forces, and it is the value δ that you need to start with in the work calculations. The calculation of the

equilibrium quantity δ itself is easily carried out using Eqn (209) and gives the result [99]

$$\delta = \left(\frac{21}{80}\right)^{1/6} \sigma_{CC} \approx 0.277 \text{ nm} \quad (213)$$

which is almost twice the lattice parameter b. Now, using Eqns (210) and (213), we can express line and point energy in terms of Lennard-Jones potential parameters. From Eqn (207), we find for line energy

$$\varepsilon = \frac{\pi}{27}\left(\frac{80}{21}\right)^{1/2} \frac{\varepsilon_{CC}}{b}\left(\frac{\sigma_{CC}}{b}\right)^3 \quad (214)$$

and, from Eqn (214), for point energy

$$\eta = \frac{4}{81}\left(\frac{80}{21}\right)^{1/3} \varepsilon_{CC}\left(\frac{\sigma_{CC}}{b}\right)^4 \approx 0.077\varepsilon_{CC}\left(\frac{\sigma_{CC}}{b}\right)^4 \quad (215)$$

For given values of ε_{CC}, σ_{CC}, and b, Eqns (214) and (215) yield $\varepsilon \approx 0.818 \times 10^{-11}$ J m^{-1} and $\eta \approx 0.962 \times 10^{-21}$ J. For line energy, this is 7.4 times, and for point energy, 3.8 times less than in the calculation based on the hard ball model. The result is clear: in this case of the Lennard-Jones model, the calculation starts from a much larger distance δ, when the forces of attraction are already significantly weakened.

With respect to the line energy of graphene, the resulting Eqn (214) [101] is consistent with Ref. 99 where the calculation was based on the Lennard-Jones potential taking into account repulsive forces but without chemical bonds (the calculation of the point energy was not performed there). In this variant, the contribution to the line energy of graphene is about 0.545×10^{-11} J m^{-1} (Ref. 99), from where (in comparison with the above value) it can be seen that the repulsive forces 'eat up' a third of the calculated dispersion component of the graphene line energy.

To conclude the section, we note two circumstances. It was previously shown that the main contribution to the line energy of graphene was made by chemical bonds between carbon atoms, while the contribution of the dispersion forces is an order of magnitude less.[99] Does this mean that such a relationship should be preserved for point energy? Rather not necessarily. The fact is that the line energy is directly found from the work of cohesion, whereas the point energy is found from the excess of the work of cohesion associated with the proximity to the corner of a rectangular piece of graphene. Here the contribution of specific forces depends on their long-range action. In the two above models with zero long-range chemical forces, only dispersion forces contribute to point energy, which, in this case, is fully calculated. The real contribution of chemical forces to point energy has not yet been determined, and only after it is found it will be possible to judge the relative contribution of the dispersion forces to the point energy of graphene. The calculation of the contribution of chemical bonds to the point energy of graphene remains a challenge to modern quantum chemistry.

The second circumstance that needs to be noted is that the structure of graphene was considered unchanged in the process of separation of its two regions. In reality, the process of relaxation of the boundary zones develops. It is difficult to calculate it, but computer modelling shows that the greatest distortions occur just near the corners of a sample.[103] This underlines, on the one hand, the importance of calculating the point energy of a two-dimensional structure, and, on the other, the incompleteness of the calculation carried out in this direction. A rigorous estimate of the graphene point energy should include taking into account not only chemical bonds, but also the relaxation of the graphene structure (the local density of carbon atoms) near the line and the corner of the cut.

In the manipulation of the unshakable structure in the form of a corner, another nuance arises. After all, each corner has two sides, two lines. We operated on one of them, which can be called active, because it interacts with the opposite line of a two-dimensional slit. The second line (oriented perpendicularly to the slit, Fig. 36) was inactive. However, both lines must be the same in the final state of equilibrium, when one part of graphene is removed from the other at an infinite distance and behaves independently. Obviously, the final unification of the sides of the corner is achieved by redistributing the internal energy, and since the remote part of the body is in a vacuum and does not interact with any other bodies, this process does not require additional work. Thus, although we dealt with only one of the sides, the calculated work of the formation of the corner gives the point energy value, which is true for the final state in the absence of relaxation.

7. Concluding remarks

Of course, the review is not exhaustive. After all, it is not called 'Dispersion forces', but 'Dispersion forces in nanoscience'. We did not deal with questions related to the nature of dispersion forces and the Lifshitz theory.[104–108] For us, dispersion forces are a given, and it is only important to describe how they are used in theoretical nanoscience. In this case, we focused on the direction that was undeservedly bypassed in previous reviews. But here too, the incompleteness of coverage is very visible. We did not touch upon the area of the computer experiment, although we ourselves were pioneers in it (with the world's first calculation of the surface tension of an argon cluster with dispersion forces using the molecular dynamics method [109]). To date, this area has grown so much that it can be the subject of an independent review.

It should also be noted that the theoretical description in the review is given more concisely, with the loss of many details in comparison with the original publications. Thus, in asymptotic relations, only the principal terms are often retained and the correction terms are omitted. Meanwhile, comparing the first and second helps to establish the scope of the asymptotics. In the reviewed works, such assessments were made repeatedly, and it was established that the width of the restricted area is expressed in angstroms! There are many other interesting details that the reader will find in the original articles. After all, the purpose of the review is to indicate such publications.

Numerous calculations performed in the reviewed papers are based on statistical mechanics, hence requiring one- and two-particle distribution functions. The first is easily determined: it is simply the local density of the number of molecules. As for the second, in the simplest case it is equal to the product of one-particle distribution functions. This technique has often been used in calculations either on the basis of the condition for weakening correlations at large distances, or when working with a solid

when the molecules are fixed in space. In the latter case, the molecules are arranged randomly if we are talking about an amorphous solid, and in strict order in crystals. Here we need to make one technical note. We did calculations by integrating, but for crystals, strictly speaking, it should be replaced by summation. The error that occurs when replacing the summation by integration, the greater the larger the lattice constant. A good illustrative example is graphite, which is sknown to consist of sheets of graphene. The interplanar distance in graphite is so large (0.3354 nm) that replacing the summation by integration reduces the energy of dispersion interaction of sheets with each other by 7 times.[99] So the use of integration is unacceptable here. By contrast, the use of integration instead of summation is quite acceptable inside each sheet of graphene, where the distance between adjacent carbon atoms is only 0.142 nm.

It is appropriate to note that for crystalline solids, in many cases, chemical bonds are most important, which explains the strength of crystals. Dispersion forces fade into the background here. However, the analysis of the role of chemical bonds in nano-systems lags far behind such studies for dispersive forces. On the example of the Irving–Kirkwood stress tensor, we see that statistical mechanics is ready to work with any pair potentials and expects that quantum mechanics will generate such potentials for chemical forces. So we see that further development of the theory of dispersion forces in nanoscience depends on the progress in quantum chemical calculations.

References

1. F.London. *Z. Phys.*, **63**, 245 (1930)
2. F.London. *Z. Phys. Chem.*, **11**, 222 (1930)
3. H.B.G.Casimir, D.Polder. *Phys. Rev., C*, **73**, 360 (1948)
4. H.C.Hamaker. *Physica*, **4**, 1058 (1937)
5. B.V.Derjaguin. *Kolloidn. Zh.*, **17**, 207 (1955)
6. A.I.Rusanov. *Phasengleichgewichte und Grenzflächenerscheinungen*. (Berlin: Akademie-Verlag, 1978)
7. B.V.Derjaguin, N.V.Churaev, V.M.Muller. *Surface Forces*. (Consultants Bureau, Plenum Press, New York, 1987)
8. A.I.Rusanov. *Colloid J.*, **69**, 39 (2007)
9. B.V.Derjaguin, L.D.Landau. *Acta Physicochim. URSS*, **14**, 633 (1941)
10. J.Mahanty, B.W.Ninham. *Dispersion Forces*. (London: Academic Press, 1976)
11. E.M.Lifshitz. *Sov. Phys. JETP*, **2**, 73 (1956)
12. I.E.Dzyaloshinskii, E.M.Lifshitz, L.P.Pitaevskii. *Sov. Physics-Uspekhi*, **4**, 153 (1961)
13. D.Langbein. *Springer Tracts in Modern Physics*. Vol. 72. (Berlin; Heidelberg: Springer, 1974)
14. O.Sinanoglu. *Chem. Phys. Lett.*, **1**, 340 (1967)
15. O.Sinanoglu. In *Intermolecular Forces, Advances in Chemical Physics*. Vol. 12. (Ed. J.O.Hirschfelder). (New York: Wiley, 1967). P. 283
16. T.Halicioglu, O.Sinanoglu. *J. Chem. Phys.*, **49**, 996 (1968)
17. T.Morita, K.Hiroike. *Prog. Theor. Phys.*, **25**, 537 (1961)
18. J.L.Lebowitz, J.K.Percus. *J. Math. Phys.*, **4**, 116 (1963)
19. F.M.Kuni. *Vestnik Leningrad. Univ.*, (22), 7 (1964)
20. F.M.Kuni. *Vestnik Leningrad. Univ.*, (4), 11 (1965)
21. J.E.Enderby, T.Gaskell, N.H.March. *Proc. Phys. Soc.*, **85**, 217 (1965)
22. T.Gaskell. *Proc. Phys. Soc.*, **86**, 693 (1965)
23. F.M.Kuni. *Phys. Lett.*, **26A**, 305 (1968)
24. F.M.Kuni. *Dokl. Akad. Nauk SSSR (Sov. Phys. Dokl.)*, **179**, 129 (1968)
25. F.M.Kuni. *Vestnik Leningrad. Univ.*, (4), 30 (1968)
26. F.M.Kuni. V.L.Kuzmin, *Phys. Lett.*, **27A**, 4 (1968)
27. J.H.Irving, J.G.Kirkwood. *J. Chem. Phys.*, **18**, 817 (1950)
28. J.G.Kirkwood, F.P.Buff. *J. Chem. Phys.*, **17**, 338 (1949)
29. F.P.Buff. *J. Chem. Phys.*, **23**, 419 (1955)
30. A.Harasima. *Proc. Phys.-Math. Soc. Jpn*, **23**, 983 (1941)
31. A.Harasima. In *Advances in Chemical Physics*. Vol. 1. (Ed. I.Prigogine). (New York: Interscience Publ., 1958). P. 203
32. F.M.Kuni, A.I.Rusanov. *Russ. J. Phys. Chem.*, **42**, 443 (1968)
33. A.I.Rusanov, F.M.Kuni. *Russ. J. Phys. Chem.*, **42**, 621 (1968)
34. F.M.Kuni, A.I.Rusanov. *Russ. J. Phys.Chem.*, **42**, 903 (1968)
35. A.I.Rusanov, F.M.Kuni. *Russ. J. Phys. Chem.*, **42**, 1353 (1968)
36. F.M.Kuni, A.I.Rusanov. *Russ. J. Phys. Chem.*, **42**, 1356 (1968)
37. A.I.Rusanov, F.M.Kuni. *Russ. J. Phys. Chem.*, **42**, 1523 (1968)
38. A.I.Rusanov, F.M.Kuni, E.N.Brodskaya. *Russ. J. Phys. Chem.*, **44**, 419 (1970)
39. A.I.Rusanov, F.M.Kuni, E.N.Brodskaya. *Russ. J. Phys. Chem.*, **44**, 423 (1970)
40. A.I.Rusanov, F.M.Kuni, E.N.Brodskaya. *Russ. J. Phys. Chem.*, **44**, 1231 (1970)
41. A.I.Rusanov, F.M.Kuni. In *Research in Surface Forces*. Vol. 3. (Ed. B.V.Derjaguin). (New York; London: Consultants Bureau, 1971). P. 111
42. E.N.Trofimova, F.M.Kuni, A.I.Rusanov. *Colloid J. USSR*, **31**, 4 (1969)
43. F.M.Kuni, A.I.Rusanov, E.N.Brodskaya. *Colloid J. USSR*, **31**, 6 (1969)
44. J.A.Mann, K.C.Porzio. In *Physical Chemistry. Series Two*. Vol. 7. (Ed. M.Kerker). (London; Boston: Surface Chemistry and Colloids, Butterworths, 1975). P. 47
45. F.M.Kuni, A.I.Rusanov. *Colloid J. USSR*, **32**, 2 (1970)
46. F.M.Kuni, A.I.Rusanov. *Colloid J. USSR*, **33**, 1 (1971)
47. F.M.Kuni, A.I.Rusanov. *Colloid J. USSR*, **33**, 2 (1971)
48. A.I.Rusanov. *Surf. Sci. Rep.*, **23**, 173 (1996)
49. A.I.Rusanov. *Surf. Sci. Rep.*, **58**, 111 (2005)
50. F.M.Kuni, A.I.Rusanov. In *Physical Adsorption from Multicomponent Phases*. (Eds M.M.Dubinin, V.V.Serpinsky). (Moscow: Nauka, 1972). P. 182
51. E.N.Brodskaya, F.M.Kuni, A.I.Rusanov. *Colloid J. USSR*, **32**, 6 (1970)
52. E.N.Brodskaya, F.M.Kuni, A.I.Rusanov. *Colloid J. USSR*, **33**, 1 (1971)
53. A.I.Rusanov. *Surf. Sci. Rep.*, **67**, 117 (2012)
54. B.Goetzelmann, R.Evans, S.Dietrich. *Phys. Rev. E*, **57**, 6785 (1998)
55. J.R.Henderson. *Physica A*, **305** 381 (2002)
56. J.R.Henderson. *Phys. Rev. E*, **69**, 061613-1 (2004)
57. J.R.Henderson. *J. Chem. Phys.*, **120**, 1535 (2004)
58. D.J.Diestler, M.Schoen. *Phys. Rev. E*, **62**, 6615 (2000)
59. A.I.Rusanov, A.K.Shchekin. *Mol. Phys.*, **103**, 2911 (2005)
60. A.I.Rusanov, A.K.Shchekin. *Mol. Phys.*, **105**, 3185 (2007)
61. A.I.Rusanov, A.K.Shchekin. *Colloid J.*, **67**, 205 (2005)
62. A.I.Rusanov, A.K.Shchekin. *Colloid J.*, **70**, 260 (2008)
63. E.N.Brodskaya, A.I.Rusanov. *Colloid J.*, **71**, 22 (2009)
64. A.I.Rusanov, E.N.Brodskaya. *Colloid J.*, **71**, 712 (2009)
65. E.N.Brodskaya, A.I.Rusanov. *Colloid J.*, **71**, 459 (2009)
66. E.N.Brodskaya, F.M.Kuni, A.I.Rusanov. *Colloid J.*, **72**, 301 (2010)
67. E.N.Brodskaya, A.I.Rusanov, F.M.Kuni. *Colloid J.*, **72**, 602 (2010)
68. E.N.Brodskaya, A.I.Rusanov, F.M.Kuni. *Colloid J.*, **72**, 612 (2010)
69. E.N.Brodskaya. *Colloid J.*, **74**, 280 (2012)
70. A.I.Rusanov, F.M.Kuni. *J. Chem. Phys.*, **131**, 106101-1 (2009)
71. A.I.Rusanov, F.M.Kuni. *Colloid J.*, **72**, 49 (2010)
72. A.I.Rusanov, E.N.Brodskaya. *Colloid J.*, **75**, 3091 (2013)

73. E.N.Brodskaya, A.I.Rusanov. *Colloid J.*, **76**, 522 (2014)
74. E.N.Brodskaya, A.I.Rusanov. *Colloid J.*, **766**, 651 (2014)
75. E.N.Brodskaya, A.I.Rusanov. *Colloid J.*, **81**, 84 (2019)
76. E.N.Brodskaya, A.I.Rusanov. *Colloid J.*, **76**, 3526 (2014)
77. E.N.Brodskaya, A.I.Rusanov. *Colloid J.*, **76**, 658 (2014)
78. E.N.Brodskaya, A.I.Rusanov. *Colloid J.*, **77**, 698 (2015)
79. E.N.Brodskaya, A.I.Rusanov. *Colloid J.*, **77**, 571 (2015)
80. R.P.Jaiswal, S.P.Beaudoin. *Langmuir*, **28**, 8359 (2012)
81. L.Onsager. *Ann. N.Y. Acad. Sci.*, **51**, 627 (1949)
82. J.N.Israelachvili. *Quart. Rev. Biophys.*, **6**, 341 (1974)
83. M.J.Vold. *J. Colloid Interface Sci.*, **9**, 451 (1954)
84. A.G.de Rocco, W.Hoover. *Proc. Nat. Acad. Sci. (USA)*, **46**, 1057 (l960)
85. M.J.Sparnaay. *Rec. Trav. Chim. Pays -Bas.*, **78**, 680 (1959)
86. S.L.Brenner, D.McQuarrie. *Biophys. J.*, **13**, 301 (1973)
87. J.Drelich, J.Long, Z.Xu, J.Masliyah, C.L.White. *J. Colloid Interface Sci.*, **303**, 627 (2006)
88. J.Chen, A.Anandarajah. *J. Colloid Interface Sci.*, **180**, 519 (1996)
89. Y.G.Gu, D.Q.Li. *J. Colloid Interface Sci.*, **217**, 60 (1999)
90. J.P.Sonnenberg, E.Schmidt. *Part. Part. Syst. Charact.*, **22**, 45 (2005)
91. D.Dantchev, G.Valchev. *J. Colloid Interface Sci.*, **372**, 148 (2012)
92. E.N.Brodskaya, A.I.Rusanov. *Colloid J.*, **81**, 9 (2019)
93. J.W.Gibbs. *The Scientific Papers*. (New York: Longmans, 1906, 1928)
94. A.I.Rusanov, V.A.Prokhorov. *Interfacial Tensiometry*. (Amsterdam: Elsevier, 1996)
95. A.I.Rusanov. *Colloids Surf., A*, **156**, 315 (1999)
96. A.I.Rusanov. *J. Chem. Phys.*, **131**, 244713 (2009)
97. A.I. Rusanov. *Colloid J.*, **72**, 669 (2010)
98. A.I.Rusanov, E.N.Brodskaya. *Colloids Surf., A*, **448**, 175 (2014)
99. A.I.Rusanov. *Surf. Sci. Rep.*, **69**, 296 (2014)
100. A.I.Rusanov. *Nanoscale*, **6**, 8130 (2014)
101. A.I.Rusanov. *Colloid J.*, **88**, 36 (2019)
102. Z.-L.Li, Z.-M.Li, H.-Y.Cao, J.-H.Yang, Q.Shu, Y.-Y.Zhang, H.J.Xiang, X.G.Gong. *Nanoscale*, **6**, 4309 (2014)
103. A.S.Barnard, I.K.Snook. *J. Chem. Phys.*, **128**, 094707-1 (2008)
104. Yu.S.Barash, B.L.Ginzburg. *Usp. Fiz. Nauk*, **116**, 5 (1975)
105. I.G.Kaplan. *Theory of Molecular Interactions*. (Amsterdam: Elsevier, 1986)
106. Yu.S.Barash. *Van der Waals Forces*. (Moscow: Nauka, 1988) (in Russian)
107. I.G.Kaplan. *Intermolecular Interactions: Physical Picture, Computational Methods and Model Potentials*. (Padstow: Wiley, 2006)
108. E.I.Kats. *Physics-Uspekhi*, **58**, 892 (2015)
109. A.I.Rusanov, E.N.Brodskaya. *J. Colloid Interface Sci.*, **62**, 542 (1977)